THE EFFECTS OF HYDRATION ON LOW-ANGLE SUBDUCTION SYSTEMS

By Sarah Elizabeth Petersen

A Dissertation

Submitted in Partial Fulfillment
of the Requirements for the Degree of
Doctor of Philosophy
in Earth Sciences and Environmental Sustainability

Northern Arizona University

August 2021

Approved:

Ryan Porter, Ph.D., Chair

Thomas Hoisch, Ph.D.

Paul Umhoefer, Ph.D.

Jeffrey Kennedy, Ph.D.

ABSTRACT

THE EFFECTS OF HYDRATION ON LOW-ANGLE SUBDUCTION SYSTEMS

SARAH ELIZABETH PETERSEN

Low-angle subduction has a profound impact on subduction zone behavior. However, the mechanisms that initiate, drive, and sustain flat-slab subduction are debated. Within all subduction zone systems, metamorphic dehydration reactions within the down-going slab create conditions that allow for seismicity and melting of the asthenospheric wedge, leading to arc volcanism. In flat-slab systems, the low angle of the subducting slab cuts off corner-flow in the asthenospheric wedge, leading to a colder thermal regime inboard of the trench relative to typical subduction, and effectively shutting off arc volcanism. This allows for the stability of H_2O-bound minerals well inboard of the trench. The implications of this include increased slab buoyancy, hydration of the overriding lower continental lithosphere, and a delay in slab eclogitization processes.

This dissertation presents new modeling results that assess the role of water in flat-slab subduction. Thermal modeling of the Alaskan flat-slab subduction system and stable mineral assemblage calculations provide insight into the effects of hydration on slab density. Results show that an anhydrous slab is not sufficiently buoyant to maintain a low-angle subduction geometry, and would require dynamic forces (i.e. asthenospheric upwelling, slab suction) to explain the observed subduction angle. A moderate amount of hydration (1-1.5% chemically bound water) reduces slab density by 0.5-0.8%, and is sufficient to produce a buoyant slab that extends to 300-400 km from the trench.

By using the thermal modeling and mineral assemblage calculations in Alaska to estimate seismic velocities, a comparison can be made between our models and observational seismic data. Seismic velocities are sensitive to temperature, pressure, composition, hydration state, and the presence of absence of melt. The non-uniqueness of seismic data makes isolating any one of these factors challenging using only seismic observations. To overcome this, we constrain pressure, temperature, and composition states using our models in to better isolate the effects of hydration. Results indicate that approximately 3% chemically-bound H_2O is present within the subducting Alaskan flat-slab.

Finally, we calculate density models of the Colorado Plateau and adjacent Basin and Range Province and Great Basin Province in the Southwestern region of the United States. Flat-slab subduction associated with Laramide tectonics is thought to have hydrated the lower crust of the Colorado Plateau lowering its density. We quantify the amount of uplift that can be associated with isostatic support in this study.

A better understanding of the role that water plays during flat-slab subduction can provide more informed interpretations of geological and geophysical data associated with regions that are current or former flat-slab systems. By using forward modeling approaches along with observational data, we can better constrain and interpret geological observations. Altogether, this dissertation presents new methods and insights into the role of water in flat-slab subduction systems, with clear implications for future research, data analysis, and data interpretation of regions affected by flat-slab tectonics.

.

COPYRIGHT

Chapter 2

ACKNOWLEDGMENTS

I’ve wanted to be a scientist for as long as I can remember. I have always been interested in knowing why or how things are the way they are. Even as a teenager, I knew that I wanted to pursue a career in the geosciences. I loved learning about earthquakes, volcanoes, mountain building, floods, and other natural phenomena. This love for learning and understanding how the Earth works has fueled my passion and drive through my undergraduate degree, master’s degree, and finally through my doctoral degree. This journey of learning would have not been possible without the guidance and support of many people. This includes my own parents, Kent and Linda Robinson, who guided me when they home-schooled me through high school. My Dad’s education in astrophysics fueled my love for science, as did my Mom’s love of teaching and learning more about natural disasters. During my undergraduate and Master’s degrees, I was mentored by ASU professors Dr. Ramon Arrowsmith, Dr. Steven Semken, and Dr. Edward Garnero. Without these men I would not have continued down the path of higher education. Finally, for my Ph.D., my professors and advisors Dr. Ryan Porter, Dr. Thomas Hoisch, Dr. Paul Umhoefer, and Dr. Jeffrey Kennedy have provided continued support and guidance on my journey.

To my Ph.D. supervisor and committee members: Thank you for your support, guidance, and knowledge. To Dr. Ryan Porter, who served as my primary advisor, thank you for your unending patience with me, for your willingness to help and answer my millions of questions, and for guiding me down this path for the past several years. I do not mean it lightly when I say that I could not have done this without your support, and that I cannot imagine a better or more helpful advisor. To Dr. Thomas Hoisch, thank you for your time, work, and guidance with using *Thermod*, and for the many conversations you had with me that broadened my understanding and knowledge of thermal modeling and metamorphic processes. Thank you for being thorough when you review my work, and for pushing me to write more concisely and accurately. To Dr. Paul Umhoefer, thank you for believing in me and for always pushing me to broaden my thinking. Thank you for guiding me in the advancement of my knowledge of tectonics and subduction processes. To Dr. Jeffrey Kennedy, thank you for allowing me to ride along with you on your field work, and for your knowledge and insight into geophysical processes and data that I was less familiar with.

To the NAU geophysics group and lab, thank you all for your questions, support, and knowledge. I am very grateful for the conversations I have had with professors Dr. Donna Shillington and Dr. James Gaherty. I am also unendingly grateful for the support of the geophysics graduate students, especially to Tanya van der Vis, Andrew Platt, Allison Haddon-Moore, John Compton, John Spruell, Cyanna Hicks, Shannon Rees, and of course my now-husband Cameron Petersen. Thank you also to the support, insight, and guidance of NAU graduate students Mike Darin, Casey Tierney, Casey Jones, Stephanie Arcusa, Rachel Krueger, and Emma Lodes. To the SES administrative staff, I would especially like to thank Amy Wolkowinsky, Sarah Colby, Robert Lenegan, and Tracy Tiedemann for their constant support and help. Your hard work does not go unnoticed.

I would like to extend a special thanks to the Pacific Geoscience Centre (PGC) in British Columbia, especially to Jiangheng He and Kelin Wang for their support and guidance during my visit there to learn finite element thermal modeling, and for their insight into the thermal modeling of subduction zones. Thank you to the non-profit organization GEM Environmental for their financial support in making my visit to PGC possible. A special thanks to Eric Welsh at GEM for his involvement and support of my PhD journey.

I don’t know how I would have completed this PhD journey without the support of my close friends, including Kristen Whitney, Dr. Megan Miller, Dr. Michael Pagano, Dr. Brandon Mechtley, Amy Zink, Emma Lodes, Dr. Stephanie Arcusa, Tyler Jones, and Casey Jones. You each helped me to laugh when things got tough, to talk through things when I needed to, and supported me in diverse ways, each of which helped me in finishing this journey. I am also grateful for the support and encouragement of my father-in-law Christopher Petersen and my sister-in-law Dr. Courtney Petersen.

I am so overwhelmingly grateful to my husband Cameron Petersen, who not only has helped me broaden my scientific knowledge, but has supported me emotionally and spiritually during this time. I love you so much, and I’m so grateful that you came to NAU (thanks for accepting him, Ryan). Thank you to my family, Kent and Linda Robinson, Rachel Cromwell (and James, Isaac, and Jackson), Luke Robinson, and Anna Robinson. Your overwhelming support of me is so appreciated, and I love all of you. Finally, I would like to thank Jesus Christ, without whom I would not have had the hope, peace, and drive to finish this race.

TABLE OF CONTENTS

LIST OF TABLES

LIST OF FIGURES

CHAPTER 1: INTRODUCTION TO FLAT-SLAB SUBDUCTION SYSTEMS

1.1 AN OVERVIEW FLAT-SLAB TECTONICS

Flat-slab subduction is a phenomena that occurs at convergent margins, where the downgoing oceanic plate assumes a shallow or horizontal angle beneath the overriding plate. This occurs in ~10% of subduction zones worldwide by length (Gutscher et al., 2000). Flat-slab subduction zones are characterized by a variety of geological phenomena, including the migration of deformation inboard from the plate margin, the inboard migration or cessation of subduction-related volcanism, hydration of the overriding continental lithosphere through the dewatering of the slab, and others (e.g. Coney and Reynolds, 1977; Dickinson and Snyder, 1978; Bird, 1988; Saleeby, 2003; Ramos and Folguera, 2009). Globally, flat-slab subduction zones vary in length laterally between 250 km (Costa Rica), and 1500 km (Peru) (Huangfu et al., 2016). They are often associated with the subduction of aseismic ridges which vary in age between 8 Ma (Cascadia) and 55 Ma (Alaska) (Davis and Plafker, 1986; Gutscher et al., 2000; van Hunen et al., 2002; Huangfu et al., 2016). The cessation of flat-slab subduction may occur due to slab break-off or slab rollback, which can trigger widespread volcanism as the sinking slab is replaced by upwelling hotter material from the underlying asthenosphere (Coney and Reynolds, 1977; Coney, 1978; Clark et al., 1982; Humphreys, 1995).

In this dissertation, we focus on two geographical regions affected by flat-slab subduction. The first is the Alaskan flat-slab subduction zone in southeastern Alaska. Here the Yakutat oceanic plateau is subducting beneath the North American plate at approximately 5 cm/yr at a low subduction angle (~7°) (Argus et al., 2010; Bauer et al., 2014; Elliot et al., 2010; Plattner et al., 2007; Ward, 2015; Worthington et al., 2012). Flat-slab subduction has been ongoing in Alaska since ~20 Ma (Finzel et al., 2011). The second region of study is the Colorado Plateau and adjacent Basin and Range Province in southwestern USA. During the

Laramide orogeny (80-40 Ma), flat-slab subduction of the Farallon slab is theorized to have hydrated the lithosphere of the Colorado Plateau, which impacted its density structure (Humphreys et al., 2003; Schulze et al., 2015; Porter et al., 2017). The purpose of the evaluation of these two geographical regions is to provide insight into flat-slab subduction processes in each respective region, and flat-slab systems as a whole.

Several hypotheses have been debated as to the cause of flat-slab subduction, including fast convergence rates, fast overriding plate motion, young (warmer and more buoyant) oceanic slabs, the subduction of thicker crust (e.g. buoyant aseismic ridges), slab suction, and the incorporation of water into subducting slabs (Jischke, 1975; Stevenson and Turner, 1977; Pilger, 1981; Cross and Pilger, 1982; Gutscher, 2002; O'Driscoll et al., 2009; Ramos and Folguera, 2009; Skinner and Clayton, 2010; Manea et al., 2011; Porter et al., 2012; Gardner et al., 2013; Knezevic Antonijevic et al., 2015; Ma and Clayton, 2015; Petersen et al., 2021). However, in the Alaskan flat-slab subduction region, many of these mechanisms are absent or unlikely to be the primary control on subduction geometry. Young, hot oceanic lithosphere is not present, and both the convergence rate and the absolute (trenchward) overriding plate motion are not especially high (Cross and Pilger, 1982; van Hunen et al., 2002). Additionally, the subducting oceanic plateau in Alaska known as the Yakutat terrane is theorized to have formed around 55 Ma – disqualifying it as a young plateau (Davis and Plafker, 1986; Wells et al., 2014). Thus, a closer look at other potential flat-slab mechanisms is warranted to determine the nature of flat-slab subduction in the Alaska region. One of these potential mechanisms is the incorporation of water into flat-slab systems.

When water is incorporated into the subducting slab, it is incorporated into hydrous phases, which results in lowered rock densities (i.e. Peacock and Wang, 1999). In flat-slab systems, the cut-off of asthenospheric corner flow can result in much lower temperatures than those observed in a steep subduction system (English et al., 2003). This, in combination with a shallow subduction angle can delay dehydration reactions within the slab until long distances from the trench (English et al., 2003). Thus, the maintained stability of hydrous mineral assemblages in slabs with shallow-angle subduction increases slab buoyancy relative to those slabs in steep subduction systems.

Water is present to varying degrees in all subduction systems regardless of subduction angle (Peacock, 1990; Peacock, 1993a; Peacock, 1993b; van Keken et al., 2002; Hacker and Abers, 2003; Hacker & Abers, 2004; Rüpke et al., 2004; Bebout & Penniston-Dorland, 2016; Zheng et al., 2016; Garth & Rietbrock, 2017; Cai et al., 2018; Condit et al., 2020). The low-angle of subduction may be maintained by the delay of dehydration reactions in flat-slab systems. However, hydration may not explain the initiation of low-angle subduction unless there is reason for excess hydration in an area. It is therefore important to ascertain what is different about flat-slab systems during their initial subduction when compared with steeper subduction geometry systems.

One possibility is the difference in the nature of the subducting crust in flat-slab systems. Flat-slab subduction zones globally have a higher correlation with the subduction of aseismic ridges or oceanic plateaus (Gutscher et al., 2000), suggesting that oceanic plateaus and aseismic ridges are anomalously buoyant (van Hunen et al., 2002). This suggests a few possibilities: (1) that thicker oceanic crust is more buoyant due to a greater volume of crust, even if essentially anhydrous, (2) that aseismic ridges and oceanic plateaus are more buoyant than thinner subducting oceanic crust because more water is incorporated into the crust during formation (or something else fundamentally different occurs during aseismic ridge formation that increases crustal buoyancy), (3) that aseismic ridges and oceanic plateaus experience hydration/alteration after their formation. It is also possible that the fundamental difference between typical oceanic crust and aseismic ridges/oceanic plateaus involves hydration in the slab mantle – either during its formation or due to secondary hydration/alteration events. In order to test these possibilities, we must evaluate carefully the nature of aseismic ridges/oceanic plateaus, and the nature of hydration in flat-slab subduction systems.

1.2 WATER AND FLAT-SLAB SUBDUCTION ZONES

Although water is known to play an important role in subduction processes, the quantity and mechanisms by which water is incorporated into subducting oceanic slabs—particularly in the lower crust and upper mantle—is a matter of debate and ongoing research (e.g., Peacock & Wang, 1999; Peacock, 2001; van Keken et al., 2002; Hacker & Abers, 2004; Rüpke et al., 2004; Bebout and Penniston-Dorland, 2016; Zheng et al., 2016; Abers et al., 2017; Garth and Rietbrock, 2017; Cai et al., 2018; Park & Rye, 2019; Condit et al., 2020). Fresh oceanic basalt typically only contains 0.1-0.5 % chemically bound H_2O, but ocean-water interaction and submarine weathering can allow basalt to hold much more (up to ~6 wt% mineral-bound) (Dixon et al., 1988; Peacock, 1993a). It is theorized that water may infiltrate through the subducting slab via fractures in the outer rise produced by the bending of the slab approaching the trench (Peacock, 2001; Yanez et al., 2002; Ranero et al., 2003; Faccenda et al, 2009; Lefeldt et al., 2012; Porter et al., 2012; Naif et al., 2015; Zheng et al., 2016). Detailed seismic and heat-flow surveys of outer-rise regions indicate both pervasive hydration and active fluid circulation within subducting slabs – up to several kilometers below the crust-mantle boundary (Ranero et al., 2003; Ranero et al., 2004; Ranero et al., 2005; Grevemeyer et al., 2007; Conteras-Reyes et al., 2008; Tilmann et al., 2008). Thus, hydration in subducting slabs is likely concentrated along faults and fractures present throughout the slab, while regions away from these fracture zones are likely anhydrous or mostly anhydrous.

Attempting to assess the extent of hydration in subducting slabs, however, is difficult. While seismic imaging can provide some insight into hydration state, seismic wavespeeds are affected by other factors besides hydration – including composition, temperature, pressure, and the presence of partial melt (Gueguen and Mercier, 1973; Minster and Anderson, 1981; Karato, 1986; Karato and Jung, 1998). Isolating these variables is essential for the interpretation of seismic data and the determination of hydration state.

In many flat-slab subduction zones, the subducting crust consists of either an oceanic plateau or aseismic ridge. In our study region of Alaska, the Yakutat oceanic plateau is thought to have formed at the Yellowstone hot spot ~55 Ma (Wells et al., 2014). Recent work by Park and Rye (2019) argues that during the formation of aseismic ridges and oceanic plateaus at hot spots, cracking due to the ascent and eruption of plume lavas allows for the infiltration of seawater and metasomatic underplating. This implies that these features associated with flat-slab subduction might exhibit greater hydration throughout the crust and upper mantle compared to typical oceanic crust that is formed at mid-ocean ridges, though this is debated.

Oceanic plateaus like the Yakutat plateau in Alaska also consist of an upper layer of sediments that is many kilometers thick in some places. While sediments contain pore spaces and cracks that can hold large volumes of water, this free water is likely released at shallow depths due to compression and associated compaction (e.g. Saffer and Bekins, 1998; Moore and Saffer, 2001; Bebout and Penniston-Dorland, 2016). Additionally, much of these sediments are scraped off and subcreted/underplated during the initial stages of subduction (e.g. Mankhemthong et al., 2013). Thus, at depth, a subducting oceanic plateau or aseismic ridge is composed primarily of an upper basaltic crust that is 1-2 km thick with an underlying layer composed of gabbro (van Hunen et al., 2002). These oceanic plateaus and aseismic ridges are much thicker than typical 5-7 km thick oceanic crust - the crust of the Yakutat Plateau in Alaska is ~20 km thick, and up to 27 km thick in some places (Veenstra et al., 2006; Christeson et al., 2010; Bauer et al., 2014). As unaltered basalts and gabbros have a lower density than that of the underlying asthenosphere, it has been argued by van Hunen et al., (2002) that unaltered and overthickened oceanic plateaus resist subduction even if they are relatively anhydrous. However, a thicker oceanic crust could also mean that larger volumes of water could be distributed through the slab than in that of a thinner crust. It is therefore a primary motivation of this work to assess the density state of both a relatively anhydrous oceanic plateau and a hydrated one.

In Alaska, it is important to determine what may be different about the subducting Yakutat Plateau relative to typical subducting crust, or even other flat-slab subduction systems. Many flat-slab subduction systems have associated buoyant ridges like Alaska, but none are as old as the Yakutat Plateau, which is theorized to have formed 55 Ma at the Yellowstone Hotspot off the coast of present-day northwestern US (Wells et al., 2014). The hypothesis used to explain other flat-slab systems of young and hot/buoyant slabs is likely not applicable in the Alaska system. However, the Yakutat Plateau is not only an oceanic plateau that formed at a hot-spot, it was also formed at a mid-ocean ridge (Wells et al., 2014). This could mean a greater degree of fracturing/cracking in the crust during its formation, as well as a greater degree of hydrothermal circulation. Thus, the nature of the Yakutat Plateau's formation could not only mean higher degrees of primary hydration during its formation, but also higher volumes of faults and fractures along which secondary hydration could occur.

In our work in Alaska in chapters 2 and 3, we evaluate the thermal state of the subduction zone region, as the thermal state is important for determining whether hydrous minerals are present. It is important to note that all our models are two-dimensional. Because of this, we do not account for lateral variations in temperature which could affect the hydrous state of the minerals. For example, to the eastern edge of the flat-slab region, it has been hypothesized that there is a slab tear (Bauer et al., 2014). If this tear exists, it would mean hotter temperatures to the east compared with the interior region where many of our models are. The temperature gradient could be quite sharp approaching the tear. The western boundary of the flat-slab region gradually increases in subduction dip. This would also mean an increase in temperatures compared with the center of the flat-slab subduction region. The temperature increase would likely be more gradual than what would be observed with the presence of a slab tear. Thus, our models in chapters 2 and 3 represent the cooler interior of the flat-slab subduction region, which would result in higher stability for hydrous mineral assemblages.

1.3 SUMMARY AND MOTIVATING QUESTIONS

This dissertation takes a closer look at the role of water in flat-slab subduction systems. We attempt a multifaceted approach, using both forward modeling and the incorporation of seismic data to evaluate the effects of water in flat-slab systems. We address the following research questions: (1) does hydration make the subducting slab in Alaska sufficiently buoyant to maintain its low angle of subduction? (2) How much chemically-bound H_2O is present in the Alaskan flat-slab system? (3) Is the Colorado Plateau in isostatic equilibrium with the adjacent Basin and Range Province? In this collection of works, the hypothesis that water plays an important role in Alaskan flat-slab subduction, and in flat-slab systems worldwide is tested.

In Chapter 2, thermal modeling and stable mineral assemblage modeling of Alaska are used to determine the effect that water has on slab buoyancy. Both finite element and finite difference thermal modeling methods are incorporated in the study to evaluate the thermal state of the Alaskan flat-slab system. We use stable mineral assemblage calculations to determine density and pressure. The effects of hydration on the Alaskan flat-slab system are evaluated by comparing models of an anhydrous slab with several models of varying degrees of hydration. Results show that a moderate amount of hydration (1-1.5 wt% H_2O) in the subducting crust and upper lithospheric mantle reduces slab density by 0.5%-0.8% relative to an anhydrous slab, and is sufficient to maintain slab buoyancy to 300-400 km from the trench. These models show that water is a viable factor in influencing the subduction geometry in Alaska, and is likely important globally.

In Chapter 3, we use our modeling results from Chapter 2 to calculate seismic velocities, and compare them with published seismic velocity models. Using the Abers and Hacker (2016) toolbox, thermal modeling, and mineral phase equilibria results, we predict P and S wave velocities within the Alaskan flat-slab subduction zone. This allows us to test hydration models for southern Alaska. Results are consistent with the subducting slab containing at least 3% chemically-bound H_2O in the 20-km thick crust and upper 10 km of the subducting mantle. These results also indicate that the subducting slab in Alaska is more hydrated than our determination of what was necessary to maintain slab buoyancy in Chapter 2.

In Chapter 4, the isostatic state of the Colorado Plateau relative to the adjacent Southern Basin and Range Province and Great Basin Province is evaluated. By integrating several recent datasets, uplift mechanisms associated with isostatic support can be evaluated. We use datasets for crustal density, crustal thickness, sediment thickness, and mantle temperatures in order to create a complete isostatic model of the Colorado Plateau and adjacent Basin and Range Province. To accomplish this, we incorporate mineral phase equilibria calculations of the lower crust and upper mantle, seismic data, heat flow data, and gravity measurements to estimate densities for the crust and upper mantle and assess the role of isostasy in supporting the plateau. As the lower lithosphere of the Colorado Plateau likely remains hydrated due to Farallon slab dewatering (Humphreys et al., 2003; Schulze et al., 2015; Porter et al., 2017), we incorporated hydration into our mineral phase equilibria calculations of the lower crust of the Colorado Plateau. Results indicate that the Colorado Plateau is largely in isostatic equilibrium with the Basin and Range, however evidence exists for dynamic uplift in the Transition Zone – the region between the Colorado Plateau and Basin and Range Province. The enigmatic high topography of the Colorado Plateau is sustained by its buoyant lower crust – due in part to hydration from Farallon flat-slab subduction.

1.4 REFERENCES

Abers, G. A., & Hacker, B. R. (2016). A MATLAB toolbox and Excel workbook for calculating the densities, seismic wave speeds, and major element composition of minerals and rocks at pressure and temperature. Geochemistry, Geophysics, Geosystems, 17(2), 616-624.

Abers, G. A., van Keken, P. E., & Hacker, B. R. (2017). The cold and relatively dry nature of mantle forearcs in subduction zones. Nature Geoscience, 10, 333–337. https://doi.org/10.1038/ngeo2922

Argus, D. F., Gordon, R. G., Heflin, M. B., Ma, C., Eanes, R. J., Willis, P., et al. (2010). The angular velocities of the plates and the velocity of Earth's centre from space geodesy. Geophysical Journal International, 180(3), 913–960. https://doi.org/10.1111/j.1365-246X.2009.04463.x

Bauer, M. A., Pavlis, G. L., & Landes, M. (2014). Subduction geometry of the Yakutat terrane, southeastern Alaska. Geosphere, 10(6), 1161–1176. https://doi.org/10.1130/ges00852.1

Bebout, G. E., & Penniston-Dorland, S. C. (2016). Fluid and mass transfer at subduction interfaces-The field metamorphic record. Lithos, 240-243, 228–258. https://doi.org/10.1016/j.lithos.2015.10.007

Bird, P., (1988), Formation of the Rocky Mountains, western United States: A continuum computer model: Science, v. 239, p. 1501.

Cai, C., Wiens, D. A., Shen, W., & Eimer, M. (2018). Water input into the Mariana subduction zone estimated from ocean-bottom seismic data. Nature, 563, 389–392. https://doi.org/10.1038/s41586-018-0655-4

Christeson, G. L., Gulick, S. P. S., van Avendonk, H. J. A., Worthington, L. L., Reece, R. S., & Pavlis, T. L. (2010). The Yakutat terrane: Dramatic change in crustal thickness across the Transition fault, Alaska. Geology, 38(10), 895–898. https://doi.org/10.1130/g31170.1

Clark, F. C., Foster, C. T., and Damon, P. E., 1982, Cenozoic mineral deposits and subduction-related arcs in Mexico: Geological Society of America Bulletin, v. 93, p. 533–544.

Coney, P.J., and Reynolds, S.J., (1977), Cordilleran benioff zones: Nature, v. 270, p. 403-406.

Coney, P. J., 1978, Mesozoic-Cenozoic Cordilleran plate tectonics, in Smith, R. B., and Eaton, G. P., eds., Cenozoic tectonics and regional geophysics of the western Cordillera: Geological Society of America Memoir 152, p. 33–50.

Contreras-Reyes, E., Grevemeyer, I., Flueh, E. R., & Reichert, C. (2008). Upper lithospheric structure of the subduction zone offshore of southern Arauco peninsula, Chile, at~ 38 S. Journal of Geophysical Research: Solid Earth, 113(B7).

Davis, A. S., & Plafker, G. (1986). Eocene basalts from the Yakutat terrane: Evidence for the origin of an accreting terrane in southern Alaska. Geology, 14(11), 963–966. https://doi.org/10.1130/0091-7613(1986)14<963:ebftyt>2.0.co;2

Dickinson, W.R., and Snyder, W.S., (1978), Plate tectonics of the Laramide orogeny: Geological Society of America Memoir, v. 151, p. 355-366.

Dixon, J. E., Stolper, E., & Delaney, J. R. (1988). Infrared spectroscopic measurements of CO2 and H2O in Juan de Fuca Ridge basaltic glasses. Earth and Planetary Science Letters, 90(1), 87–104. https://doi.org/10.1016/0012-821x(88)90114-8

Elliott, J. L., Larsen, C. F., Freymueller, J. T., & Motyka, R. J. (2010). Tectonic block motion and glacial isostatic adjustment in southeast Alaska and adjacent Canada constrained by GPS measurements. Journal of Geophysical Research: Solid Earth, 115(B9). https://doi.org/10.1029/2009jb007139

English, J. M., Johnston, S. T., & Wang, K. (2003). Thermal modelling of the Laramide orogeny: testing the flat-slab subduction hypothesis. Earth and Planetary Science Letters, 214(3-4), 619–632. https://doi.org/10.1016/s0012-821x(03)00399-6

Faccenda, M., Gerya, T. V., & Burlini, L. (2009). Deep slab hydration induced by bending-related variations in tectonic pressure. Nature Geoscience, 2(11), 790-793.

Finzel, E. S., Trop, J. M., Ridgway, K. D., & Enkelmann, E. (2011). Upper plate proxies for flat-slab subduction processes in southern Alaska. Earth and Planetary Science Letters, 303(3-4), 348–360. https://doi.org/10.1016/j.epsl.2011.01.014

Gardner, T.W., Fisher, D.M., Morell, K.D., and Cupper, M.L., (2013), Upper-plate deformation in response to flat slab subduction inboard of the aseismic Cocos Ridge, Osa Peninsula, Costa Rica: Lithosphere, v. 5, no. 3, p. 247–264, doi: 10.1130/L251.1.

Garth, T., & Rietbrock, A. (2017). Constraining the hydration of the subducting Nazca plate beneath Northern Chile using subduction zone guided waves. Earth and Planetary Science Letters, 474, 237–247. https://doi.org/10.1016/j.epsl.2017.06.041

Grevemeyer, I., Ranero, C. R., Flueh, E. R., Kläschen, D., & Bialas, J. (2007). Passive and active seismological study of bending-related faulting and mantle serpentinization at the Middle America trench. Earth and Planetary Science Letters, 258(3-4), 528-542.

Gueguen, Y., & Mercier, J. M. (1973). High attenuation and the low-velocity zone. Physics of the Earth and Planetary Interiors, 7(1), 39-46.

Gutscher, M.-A.A., Maury, R., Eissen, J.P., and Bourdon, E., (2000), Can slab melting be caused by flat subduction?: Geology, v. 28, no. 6, p. 535, doi: 10.1130/0091-7613(2000)28<535:CSMBCB>2.0.CO;2.

Gutscher, M.A. (2002), Andean subduction styles and their effect on thermal structure and interplate coupling: Journal of South American Earth Sciences, v. 15, no. 1, p. 3–10, doi: 10.1016/S0895-9811(02)00002-0.

Hacker, B. R., Peacock, S. M., Abers, G. A., & Holloway, S. D. (2003). Subduction factory 2. Are intermediate-depth earthquakes in subducting slabs linked to metamorphic dehydration reactions? Journal of Geophysical Research: Solid Earth, 108(B1).

Hacker, B. R., & Abers, G. A. (2004). Subduction Factory 3: An Excel worksheet and macro for calculating the densities, seismic wave speeds, and H2O contents of minerals and rocks at pressure and temperature. Geochemistry, Geophysics, Geosystems, 5(1).

Huangfu, P., Wang, Y., Cawood, P. A., Li, Z. H., Fan, W., & Gerya, T. V. (2016). Thermo-mechanical controls of flat subduction: Insights from numerical modeling. Gondwana Research, 40, 170-183.

Humphreys, E. D. (1995). Post-Laramide removal of the Farallon slab, western United States. Geology, 23(11), 987-990.

Humphreys, E., Hessler, E., Dueker, K., Farmer, G. L., Erslev, E., & Atwater, T. (2003). How Laramide-age hydration of North American lithosphere by the Farallon slab controlled subsequent activity in the western United States. International Geology Review, 45(7), 575-595.

Jischke, M.C., (1975), On the dynamics of descending lithospheric plates and slip zones: Journal of Geophysical Research-Solid Earth and Planets, v. 80, no. 35, p. 4809–4813, doi: 10.1029/JB080i035p04809.

Karato, S. I. (1986). Does partial melting reduce the creep strength of the upper mantle?. Nature, 319(6051), 309-310.

Karato, S. I., & Jung, H. (1998). Water, partial melting and the origin of the seismic low velocity and high attenuation zone in the upper mantle. Earth and Planetary Science Letters, 157(3-4), 193-207.

Knezevic Antonijevic, S., Wagner, L.S., Kumar, A., Beck, S.L., Long, M.D., Zandt, G., Tavera, H., and Condori, C., (2015), The role of ridges in the formation and longevity of flat slabs: Nature, v. 524, no. 7564, p. 212–215, doi: 10.1038/nature14648.

Lefeldt, M., Ranero, C. R., & Grevemeyer, I. (2012). Seismic evidence of tectonic control on the depth of water influx into incoming oceanic plates at subduction trenches. Geochemistry, Geophysics, Geosystems, 13(5).

Ma, Y., and Clayton, R.W., (2015), Flat slab deformation caused by interplate suction force: Geophysical Research Letters, v. 42, p. 1–9, doi: 10.1002/(ISSN)1944-8007.

Manea, V.C., Perez-Gussinye, M., and Manea, M., (2011), Chilean flat slab subduction controlled by overriding plate thickness and trench rollback: Geology, v. 40, no. 1, p. 35–38, doi: 10.1130/G32543.1.

Mankhemthong, N., Doser, D. I., & Pavlis, T. L. (2013). Interpretation of gravity and magnetic data and development of two-dimensional cross-sectional models for the Border Ranges fault system, south-central Alaska. Geosphere, 9(2), 242–259. https://doi.org/10.1130/ges00833.1

Minster, J. B., & Anderson, D. L. (1981). A model of dislocation-controlled rheology for the mantle. Philosophical Transactions of the Royal Society of London. Series A, Mathematical and Physical Sciences, 299(1449), 319-356.

Moore, J. C., & Saffer, D. (2001). Updip limit of the seismogenic zone beneath the accretionary prism of southwest Japan: An effect of diagenetic to low-grade metamorphic processes and increasing effective stress. Geology, 29(2), 183–186. https://doi.org/10.1130/0091-7 613(2001)029<0183:ulotsz>2.0.co;2

Naif, S., Key, K., Constable, S., & Evans, R. L. (2015). Water-rich bending faults at the Middle America Trench. Geochemistry, Geophysics, Geosystems, 16(8), 2582–2597. https://doi.org/10.1002/2015gc005927

O'Driscoll, L.J., Humphreys, E.D., and Saucier, F., (2009), Subduction adjacent to deep continental roots: Enhanced negative pressure in the mantle wedge, mountain building and continental motion: Earth and Planetary Science Letters, v. 280, no. 1-4, p. 61–70, doi: 10.1016/j.epsl.2009.01.020.

Park, J., & Rye, D. M. (2019). Broader impacts of the metasomatic underplating hypothesis. Geochemistry, Geophysics, Geosystems, 20(11), 4810–4829.

Peacock, S. A. (1990). Fluid processes in subduction zones. Science, 248(4953), 329–337. https://doi.org/10.1126/science.248.4953.329

Peacock, S. M. (1993a). Large-scale hydration of the lithosphere above subducting slabs. Chemical Geology, 108(1-4), 49–59. https://doi.org/10.1016/0009-2541(93)90317-c

Peacock, S. M. (1993b). The importance of blueschist → eclogite dehydration reactions in subducting oceanic crust. Geological Society of America Bulletin, 105(5), 684–694. https://doi.org/10.1130/0016-7606(1993)105<0684:tiobed>2.3.co;2

Peacock, S. M., & Wang, K. (1999). Seismic consequences of warm versus cool subduction metamorphism: Examples from southwest and northeast Japan. Science, 286(5441), 937–939. https://doi.org/10.1126/science.286.5441.937

Peacock, S. M. (2001). Are the lower planes of double seismic zones caused by serpentine dehydration in subducting oceanic mantle? Geology, 29(4), 299–302. https://doi.org/10.1130/0091-7613(2001)029<0299:atlpod>2.0.co;2

Penniston-Dorland, S. C., Kohn, M. J., & Manning, C. E. (2015). The global range of subduction zone thermal structures from exhumed blueschists and eclogites: Rocks are hotter than models. Earth and Planetary Science Letters, 428, 243–254.

Petersen, S. E., Hoisch, T. D., & Porter, R. C. (2021). Assessing the Role of Water in Alaskan Flat-Slab Subduction. Geochemistry, Geophysics, Geosystems, 22, e2021GC009734. https://doi.org/10.1029/2021GC009734

Pilger, R. H., Jr (1981). Plate reconstructions, aseismic ridges, and low-angle subduction beneath the Andes. The Geological Society of America Bulletin, 92(7), 448. https://doi.org/10.1130/0016-7606(1981)92<448:PRARAL>2.0.CO;2.10.1130/0016-7606(1981)92<448 :praral>2.0.co;2

Plattner, C., Malservisi, R., Dixon, T. H., LaFemina, P., Sella, G. F., Fletcher, J., & Suarez-Vidal, F. (2007). New constraints on relative motion between the Pacific plate and Baja California microplate (Mexico) from GPS measurements. Geophysical Journal International, 170(3), 1373–1380. https://doi.org/10.1111/j.1365-246x.2007.03494.x

Porter, R., Gilbert, H., Zandt, G., Beck, S., Warren, L., Calkins, J., et al. (2012). Shear wave velocities in the Pampean flat-slab region from Rayleigh wave tomography: Implications for slab and upper mantle hydration. Journal of Geophysical Research, 117(B11), B11301. https://doi.org/10.1029/2012JB009350

Porter, R., Hoisch, T., & Holt, W. E. (2017). The role of lower-crustal hydration in the tectonic evolution of the Colorado Plateau. Tectonophysics, 712, 221-231.

Ramos, V. A., & Folguera, A. (2009). Andean flat-slab subduction through time. Geological Society, London, Special Publications, 327(1), 31-54.

Ranero, C. R., Morgan, J. P., McIntosh, K., & Reichert, C. (2003). Bending-related faulting and mantle serpentinization at the Middle America trench. Nature, 425(6956), 367-373.

Ranero, C. R., & Sallarès, V. (2004). Geophysical evidence for hydration of the crust and mantle of the Nazca plate during bending at the north Chile trench. Geology, 32(7), 549-552.

Ranero, C. R., Villaseñor, A., Phipps Morgan, J., & Weinrebe, W. (2005). Relationship between bend-faulting at trenches and intermediate-depth seismicity. Geochemistry, Geophysics, Geosystems, 6(12).

Rüpke, L. H., Morgan, J. P., Hort, M., & Connolly, J. A. (2004). Serpentine and the subduction zone water cycle. Earth and Planetary Science Letters, 223(1-2), 17-34.

Saffer, D. M., & Bekins, B. A. (1998). Episodic fluid flow in the Nankai accretionary complex: Timescale, geochemistry, flow rates, and fluid budget. Journal of Geophysical Research, 103(B12), 30351–30370. https://doi.org/10.1029/98jb01983

Saleeby, J., (2003), Segmentation of the Laramide slab- Evidence from the southern Sierra Nevada region: Geological Society of America Bulletin, v. 115, p. 655.

Schulze, D.J., Davis, D.W., Helmstaedt, H., Joy, B., 2015. Timing of the Cenozoic "Great Hydration" event beneath the Colorado Plateau: Th-Pb dating of monazite in Navajo volcanic field metamorphic eclogite xenoliths. Geology 43 (8), 727–730.

Skinner, S.M., and Clayton, R.W., (2010), An Evaluation of Proposed Mechanisms of Slab Flattening in Central Mexico: Pure and applied geophysics,, p. 1–14, doi: 10.1007/s00024-010-0200-3.

Stevenson, D.J., and Turner, J.S., (1977), Angle of subduction: Nature, v. 270, p. 334–336, doi: 10.1038/270334a0.

Tilmann, F. J., Grevemeyer, I., Flueh, E. R., Dahm, T., & Gossler, J. (2008). Seismicity in the outer rise offshore southern Chile: indication of fluid effects in crust and mantle. Earth and Planetary Science Letters, 269(1-2), 41-55.

van Hunen, J., van den Berg, A. P., & Vlaar, N. J. (2002). On the role of subducting oceanic plateaus in the development of shallow flat subduction. Tectonophysics, 352(3-4), 317–333. https://doi.org/10.1016/s0040-1951(02)00263-9

van Keken, P. E., Kiefer, B., & Peacock, S. M. (2002). High-resolution models of subduction zones: Implications for mineral dehydration reactions and the transport of water into the deep mantle. Geochemistry, Geophysics, Geosystems, 3(10), 20. https://doi.org/10.1029/2001GC000256

Veenstra, E., Christensen, D. H., Abers, G. A., & Ferris, A. (2006). Crustal thickness variation in south-central Alaska. Geology, 34(9), 781–784. https://doi.org/10.1130/g22615.1

Ward, K. M. (2015). Ambient noise tomography across the southern Alaskan Cordillera. Geophysical Research Letters, 42(9), 3218–3227.

Wells, R., Bukry, D., Friedman, R., Pyle, D., Duncan, R., Haeussler, P., & Wooden, J. (2014). Geologic history of Siletzia, a large igneous province in the Oregon and Washington Coast Range: Correlation to the geomagnetic polarity time scale and implications for a longlived Yellowstone hotspot. Geosphere, 10(4), 692–719. https://doi.org/10.1130/ges01018.1

Worthington, L. L., Van Avendonk, H. J., Gulick, S. P., Christeson, G. L., & Pavlis, T. L. (2012). Crustal structure of the Yakutat terrane and the evolution of subduction and collision in southern Alaska. Journal of Geophysical Research: Solid Earth, 117(B1). https://doi.org/10.1029/2011jb008493

Yanez, G., Cembrano, J., Pardo, M., Ranero, C., & Selles, D. (2002). The Challenger-Juan Fernandez-Maipo major tectonic transition of the Nazca-Andean subduction system at 33–34 S: geodynamic evidence and implications. Journal of South American Earth Sciences, 15(1), 23–38. https://doi.org/10.1016/s0895-9811(02)00004-4

Zheng, Y., Chen, R., Xu, Z., & Zhang, S. (2016). The transport of water in subduction zones. Science China Earth Sciences, 59(4), 651–682. https://doi.org/10.1007/s11430-015-5258-4

CHAPTER 2: ASSESSING THE ROLE OF WATER IN ALASKAN FLAT-SLAB SUBDUCTION

Authors: Petersen, S.E., Hoisch,T.D., and Porter, R.C.

2.1 ABSTRACT

Low-angle subduction has been shown to have a profound impact on subduction processes. However, the mechanisms that initiate, drive, and sustain flat-slab subduction are debated. Within all subduction zone systems, metamorphic dehydration reactions within the down-going slab have been hypothesized to produce seismicity, and to produce water that fluxes melting of the asthenospheric wedge leading to arc magmatism. In this work, we examine the role hydration plays in influencing slab buoyancy and the geometry of the downgoing oceanic plate. When water is introduced to the oceanic lithosphere, it is incorporated into hydrous phases, which results in lowered rock densities. The net effect of this process is an increase in the buoyancy of the downgoing oceanic lithosphere. To better understand the role of water in low-angle subduction settings, we model flat-slab subduction in Alaska, where the thickened oceanic lithosphere of the Yakutat oceanic plateau is subducting beneath the continental lithosphere.

In this work, we calculate the thermal conditions and stable mineral assemblages in the slab crust and mantle in order to assess the role that water plays in altering the density of the subducting slab. Our slab density results show that a moderate amount of hydration (1–1.5 wt% H_2O) in the subducting crust and upper lithospheric mantle reduces slab density by 0.5%–0.8% relative to an anhydrous slab, and is sufficient to maintain slab buoyancy to 300–400 km from the trench. These models show that water is a viable factor in influencing the subduction geometry in Alaska, and is likely important globally.

2.2 INTRODUCTION

Although the plate tectonics theory is well established in the geosciences, the mechanisms and details of various plate-tectonics related phenomena are debated. In ∼10% of subduction zones, subducting slabs do not sink into the mantle at a steep angle as in the classic model of subduction (Gutscher et al., 2000). Rather, subduction of downgoing oceanic plates is characterized by low-angle to horizontal geometries and is termed “flat-slab subduction.” Several mechanisms have been proposed to explain this form of subduction, including fast convergence rate or fast trenchward overriding plate motion (van Hunen et al., 2000; Vlaar, 1983), subduction of young (warmer) slabs, the subduction of thickened and mechanically strong aseismic ridges or oceanic plateaus (Gutscher et al., 2000; van Hunen et al., 2002), slab suction (Stevenson & Turner, 1977; Tovish et al., 1978), and the presence of water in subducting slabs (Antonijevic et al., 2015; English et al., 2003; Gardner et al., 2013; Gutscher, 2002; Jischke, 1975; Ma & Clayton, 2015; Manea et al., 2011; O'Driscoll et al., 2009; Pilger, 1981; Porter et al., 2012; Ramos & Folguera, 2009; Skinner & Clayton, 2010; Stevenson & Turner, 1977).

The purpose of this study is to better understand the role that hydration plays within flat-slab subduction settings, with a focus on the Alaskan flat-slab region. In this work, we test the following hypothesis: Slab hydration and subsequent dehydration influences slab buoyancy and whether flat-slab subduction will be initiated, maintained or ended. Testing this hypothesis is important not only for providing a better under- standing of the behavior of these systems, but also for understanding seismic and volcanic hazards associated with both crustal deformation and slab rollback.

In order to test this hypothesis, thermo-mechanical models of Alaskan flat-slab subduction were calculated to provide insight into current thermal conditions. The results from these models were then used to calculate stable mineral assemblages and associated densities within the crust and upper mantle of the subducting plate. Calculations of slab density were made in order to evaluate the effect of hydration on slab buoyancy and subduction geometry.

2.3 TECTONIC SETTING

The Alaskan lithosphere formed through the accretion of several terranes to the North American plate due to convergence and strike-slip motion at the plate boundary. Subduction and related terrane accretion have created a complex and diverse crustal structure and geologic history (Bauer et al., 2014; Fuis et al., 2008). Active tectonism, including seismicity and volcanism is present throughout much of southern Alaska.

Within the study area, the Pacific plate is subducting to the northwest beneath the North American plate at approximately 5 cm/yr at a low subduction angle (∼7°) (see Figure 2.1) (Argus et al., 2010; Bauer et al., 2014; Elliott et al., 2010; Plattner et al., 2007; Ward, 2015; Worthington et al., 2012). Low-angle subduction along the southeastern margin of Alaska involves subduction of a large oceanic plateau called the Yakutat block (Bauer et al., 2014; Bruns, 1983; Davis & Plafker, 1986).

The Yakutat block is a microplate wedged between the North American and Pacific plates at the southeast- ern margin of Alaska (Figure 2.1). It is hypothesized that the block formed at ∼55 Ma as an oceanic plateau at the Yellowstone hotspot (Wells et al., 2014). In this model, the Yakutat block is the conjugate to the Siletzia Province that accreted to present-day Oregon (Wells et al., 2014). At the time of Yakutat block formation, the Yellowstone hotspot was located at a latitude between present-day Washington and British Columbia off the coast of western North America (Davis & Plafker, 1986; Wells et al., 2014). Following its formation, the Yakutat block was transported northward on the Pacific Plate to its present position along the Queen Charlotte-Fairweather fault system, which forms the plate boundary between western North America and the eastern portion of the Pacific Plate (Bauer et al., 2014; Bruns, 1983).

Subduction along the southern Alaskan margin began as early as 213 Ma (Rioux et al., 2010). There is some debate as to the timing of the collision of the Yakutat Plateau with the southern margin of Alaska, which likely coincides with the initiation of flat-slab subduction. Davis and Plafker (1986) suggest flat-slab subduction initiated at ∼10 Ma, while more recent work by Finzel et al. (2011) indicates that flat-slab subduction has been ongoing since ∼23 Ma or perhaps longer. Since its arrival at the North American plate margin in south-central Alaska, the Yakutat slab has penetrated over 600 km inland of the trench, and is thought to be the primary cause of a regional 400-km wide gap in the volcanic arc known as the Denali Gap (Eber- hart-Phillips et al., 2006; Martin-Short et al., 2016; Nye, 1999; Plafker & Berg, 1994; Wang & Tape, 2014).

The crust of the Yakutat block can be separated into two distinct layers. The upper layer consists of Eocene-Miocene marine and continental sediments that are ∼15 km thick at the western edge of the block and thin to near zero at its southeastern edge. The lower layer of the Yakutat block crust has previously been interpreted as continental crust, or a combination of continental and oceanic crust (Bruns, 1983; Plafker et al., 1978). Recent seismic studies have confirmed that the basement of the Yakutat is uniform and likely of mafic composition (Christeson et al., 2010). Basalts from the Yakutat terrane are dated at 50–55 Ma (Da- vis & Plafker, 1986), and the overall thickness of the Yakutat block is consistent with an oceanic plateau structure (Bauer et al., 2014; Bruns, 1983; Christeson et al., 2010; Davis & Plafker, 1986; Wells et al., 2014; Worthington et al., 2012).

The Yakutat block crust is approximately 24–27 km thick (overlain by sediments in some parts) and the Alaskan continental crust is between 25 and 45 km thick (Bauer et al., 2014; Christeson et al., 2010; Veenstra et al., 2006). The eastern portion of the Yakutat block is accreting to the Alaskan continent, while the west- ern portion of the block is subducting along with the Pacific Plate underneath Alaska (Bauer et al., 2014). A magnetic and gravity study in the southeastern region of Alaska has shown evidence of underplated sediments near Cook Inlet in Alaska, likely subcreted by the subduction of the Yakutat oceanic plateau (Mankhemthong et al., 2013).

The thickness of the slab in this region is estimated to be approximately 80 km based on models of lithospheric age and the depth of the lithosphere-asthenosphere boundary determined in previous Sp receiver function studies in the Alaskan region (Kumar & Kawakatsu, 2011; O'Driscoll & Miller, 2015). Previous work has shown that within the steeper subduction zone region in Alaska (west of the flat-slab subduction region in this study), 10%–20% of the mantle wedge is serpentinized due to hydration of the mantle lithosphere (Hyndman & Peacock, 2003). Further inland, high mantle Vp/Vs ratios derived from receiver function calculations possibly indicate hydrated zones at depths less than 80 km (Rossi et al., 2006). How- ever, in the flat-slab region itself, there is debate as to how much hydration is present in the subducting slab and the depth to which the subducting slab is hydrated (i.e., Chuang et al., 2017; Feng & Ritzwoller, 2019; Martin-Short et al., 2018; Rossi et al., 2006; Ward & Lin, 2018). In a recent study by Chuang et al. (2017), they argue that little to no hydration is present in the Yakutat slab beyond the top few kilometers of the upper crust, and that the oceanic plateau is essentially anhydrous. However, their work is partially dependent on seismic tomography studies that predate the EarthScope seismic deployment (Alaskan Transportable Array) (i.e., Abers et al., 2006; Rondenay et al., 2010). More recent studies that incorporate data from the EarthScope deployment indicate the possibility for the presence of hydration in the subducting lithospheric mantle (Feng & Ritzwoller, 2019; Martin-Short et al., 2018; Ward & Lin, 2018).

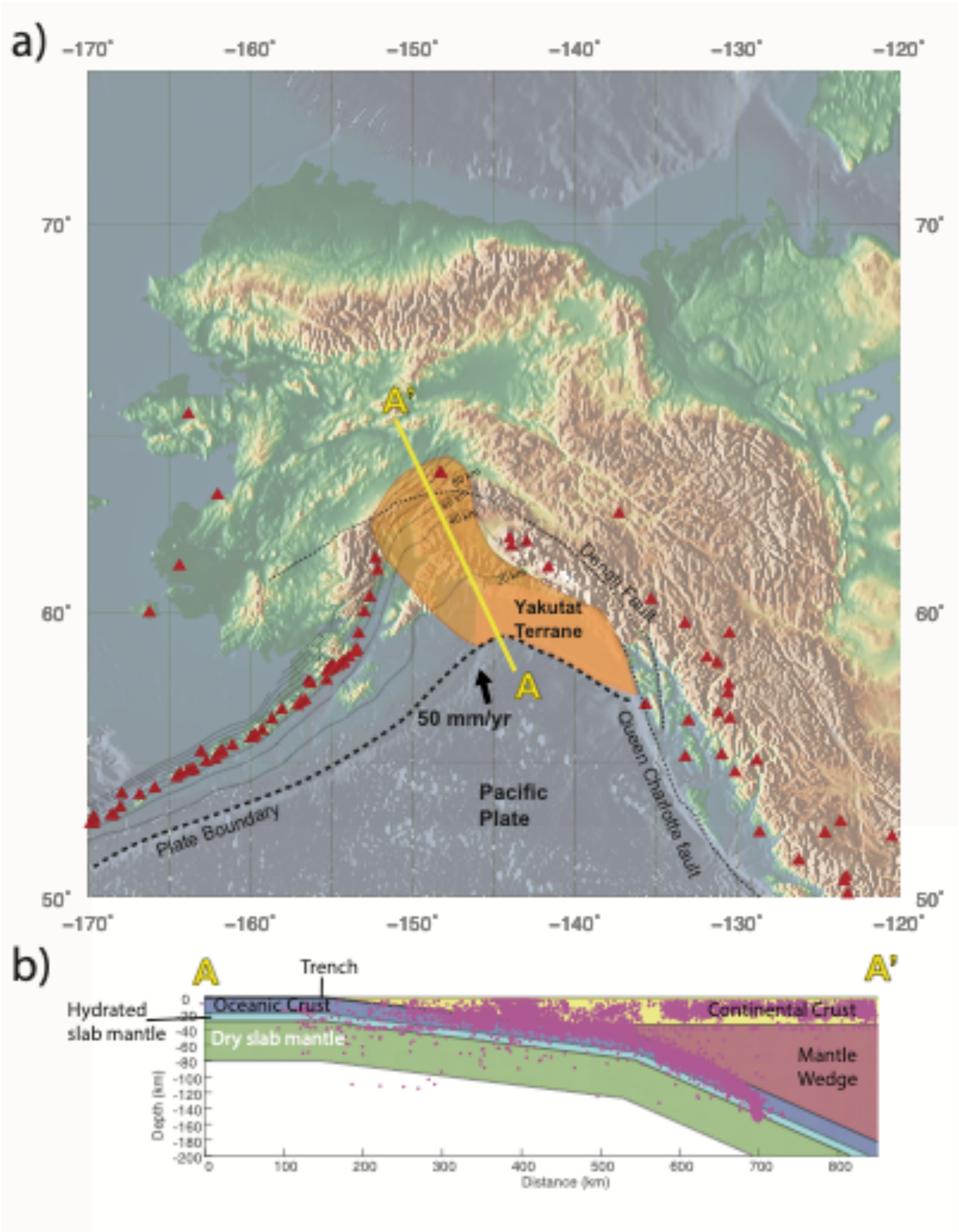

Figure 2.1. (a) Map of the study area showing the location of the 850 km transect (A–A′) used in this study in yellow. Holocene volcanoes are shown as red triangles. Flat slab subduction region and associated Yakutat terrane are highlighted in orange. The contours show slab contours with a contour interval of 20 km. Faults are shown as dotted black lines. (b) Cross section of the 850 km transect showing the geometry used for thermal modeling. Earthquakes are plotted to 150 km depth as pink dots. Earthquake data used are from the Array Network Facility (ANF), Global Centroid Moment Tensor (GCMT), National Earthquake Information Center Preliminary Determination of Epicenters (NEIC PDE), and the International Seismological Centre (ISC).

2.4 FLAT-SLAB SUBDUCTION MECHANISMS AND ALASKA

The cause of low-angle subduction in southern Alaska is enigmatic, as mechanisms commonly invoked by other low-angle subduction studies to explain flat-slab subduction (i.e., young oceanic lithosphere, fast trenchward overriding plate motion, fast subduction rate) are absent or unlikely to be the primary cause for Alaskan flat-slab subduction. Young, hot (and presumably buoyant) oceanic lithosphere is not present, and both the convergence rate and the absolute (trenchward) overriding plate motion are not especially high (Cross & Pilger, 1982; van Hunen et al., 2002). Additionally, the Yakutat terrane is considered to have been formed around 55 Ma, which does not qualify it as a young oceanic plateau. Geomechanical models of sub- ducting oceanic plateaus in van Hunen et al. (2002) found that slabs that are 44 Ma or younger were able to produce flat-slab segments due to their increased thermal buoyancy, but a 56-Ma old slab model failed to assume a horizontal geometry. Additionally, the Alaska flat-slab subduction region convergence rate is only 5 cm/yr, and the absolute (trenchward) overriding plate motion is only 2.3 cm/yr, much lower than South America's westward absolute motion of 3 cm/yr with respect to the hotspot reference frame (Olbertz et al., 1997), or the proposed westward motion of North America at 5 cm/yr during Laramide flat-slab sub- duction (Engebretson et al., 1985).

Ruling out these two mechanisms as major contributions to flat-slab subduction in Alaska, we consider other possible contributions such as the rigidity of thick oceanic crust (van Hunen et al., 2002), and the presence of hydrous mineral assemblages that increase the buoyancy of the subducting slab (Antonijevic et al., 2015; English et al., 2003; Gardner et al., 2013; Gutscher, 2002; Jischke, 1975; Ma & Clayton, 2015; Manea et al., 2011; O'Driscoll et al., 2009; Pilger, 1981; Porter et al., 2012; Ramos & Folguera, 2009; Skinner & Clayton, 2010; Stevenson & Turner, 1977). Flat-slab subduction zones globally have a high correlation with the subduction of aseismic ridges or oceanic plateaus (Gutscher et al., 2000), suggesting that oceanic plateaus, like the subducting Yakutat Plateau in Alaska, are anomalously buoyant (van Hunen et al., 2002).

Due to delays in the occurrence of metamorphic reactions that densify a slab, increased slab buoyancy can be maintained many hundreds of kilometers inboard of the trench. These reactions are delayed due to the cold thermal regime created by corner-flow cutoff and the shallow angle of subduction (Cross & Pilger, 1978; English et al., 2003; Peacock & Wang, 1999). The density of the unaltered basalts and gabbros that comprise the crust of an oceanic plateau is lower than that of the underlying asthenosphere. After sub- duction begins, eclogitization of the oceanic crust densifies the subducting slab, causing it to become more dense than the underlying mantle (Irifune & Ringwood, 1993). However, conditions of eclogite formation, which under equilibrium conditions occurs at ∼70–80 km depth (Kirby et al., 1996), will not develop in flat-slab subduction regions until many hundreds of kilometers from the trench. It was therefore suggested by van Hunen et al. (2002) that unaltered and overthickened oceanic plateaus resist subduction even if they are relatively anhydrous.

Additionally, the thickness of the subducting oceanic crust in Alaska (∼20 km) and depletion of the under- lying lithosphere could create a rather rigid plate, which would be amplified by its “old and cold” thermal state. While an older/colder subducting slab would be denser than a younger/warmer slab, it would also increase its rigidity and resistance to bending/steep subduction (van Hunen et al., 2002). In this study, we assess the contributions of thickened oceanic crust and hydration to the reduction of slab density of the downgoing slab.

2.5 WATER IN SUBDUCTION ZONES

Water is known to play an important role in subduction processes. However, the quantity and mechanisms by which water is incorporated into subducting oceanic slabs—particularly in the lower crust and upper mantle—is a matter of debate and ongoing research (e.g., Abers et al., 2017; Bebout & Penniston-Dorland, 2016; Cai et al., 2018; Condit et al., 2020; Garth & Rietbrock, 2017; Gerya, 2011; Hacker & Abers, 2004; Park & Rye, 2019; Peacock, 2001, 2009; Peacock & Wang, 1999; Rüpke et al., 2004; van Keken et al., 2002; Zheng et al., 2016). The degree of hydration likely varies greatly throughout the slab both laterally and vertically. Fresh oceanic basalt contains between 0.1 and 0.5 wt% H_2O, but ocean-floor metamorphic reactions, hydrothermal circulation, and submarine weathering can allow basalt to hold much more (up to ~6 wt% mineral-bound) (Dixon et al., 1988; Peacock, 1993a). Hydration is likely added along permeable fracture networks (Lefeldt et al., 2012; Peacock, 2001; Ranero et al., 2003).

Water is incorporated into subducting slabs through several different mechanisms. Water in oceanic sediments is held as free water within pore spaces and cracks and is also chemically bound in clastic hydrous minerals (e.g., Bebout, 2007; Stern, 2002). Much of this material is either scraped off or underplated during subduction. The free water held within pore spaces and cracks is likely released at shallow depths due to compression and associated compaction (e.g., Bebout & Penniston-Dorland, 2016; Moore & Saffer, 2001; Saffer & Bekins, 1998). Water that is chemically bound in minerals is released through metamorphic de-volatilization reactions deeper in the subduction zone (e.g., Bebout & Penniston-Dorland, 2016; van Keken et al., 2011).

The upper 1 or 2 km of subducting oceanic crust consists of basalt that has been altered chemically by ocean water, and contains free water in pore spaces and water bound in hydrous minerals (Rüpke et al., 2004; Zheng et al., 2016). The underlying crust is gabbroic and typically has some hydrothermal alteration concentrated along faults and fractures (Bebout & Penniston-Dorland, 2016; Peacock, 2001; Rüpke et al., 2004; Zheng et al., 2016). Recent work by Park and Rye (2019) argues that during the formation of aseismic ridges and oceanic plateaus at hot spots, cracking due to the ascent and eruption of plume lavas allows for the infiltration of seawater and metasomatic underplating. This would suggest that aseismic ridges and oceanic plateaus, such as the Yakutat Plateau in Alaska and other aseismic ridges associated with flat-slab subduction, might exhibit greater hydration throughout the crust and the upper mantle compared to typical oceanic crust formed at mid-ocean ridges, though this is debated. Water chemically bound in hydrous minerals in the subducting crust and mantle is estimated to contribute as much as 90% of the H_2O subducted past the accretionary prism (Ito et al., 1983; Peacock, 1990).

The lithospheric mantle has the potential to hold far more water in hydrous phases—up to nine weight percent—than oceanic crust due to the alteration of mantle peridotite to serpentine, which can be stable up to approximately 6 GPa and 700 °C (Ulmer & Trommsdorff, 1995; Wunder & Schreyer, 1997). Seismicity and arc magmatism both provide evidence of dehydration reactions occurring within the slab mantle lithosphere in subduction systems (e.g., Peacock & Wang, 1999). Ocean water may infiltrate the lithospheric mantle via fractures in the outer rise produced by the bending of the slab approaching the trench (Lefeldt et al., 2012; Naif et al., 2015; Peacock, 2001; Porter et al., 2012; Ranero et al., 2003; Yáñez et al., 2002; Zheng et al., 2016). A recent controlled-source electromagnetic study in Nicaragua found that outer-rise faulting increased total crustal H_2O stored in pore space by 60%, suggesting that significantly more pore water is infiltrating the crust via these fracture networks than previously thought (Naif et al., 2015).

The locations of aftershocks from an outer-rise earthquake in 2001 along the Juan Fernandez Ridge (an aseismic ridge contributing to flat-slab subduction in South America) suggest that the Nazca plate ruptured at least 20 km beneath the oceanic Moho, which may be indicative of faults that act as conduits for fluids, penetrating to this depth (Clouard et al., 2007; Fromm et al., 2006; Kopp et al., 2004; Porter et al., 2012). The depth to which hydration penetrates in the slab mantle due to outer rise faulting or other mechanisms is uncertain, but evidence for low P-wave in seismic wide-angle reflection and refraction studies across several subduction trenches may indicate serpentinization is occurring to depths of 25–30 km from the surface (Lefeldt et al., 2012; Seno & Gonzalez, 1987; Seno & Yamanaka, 1996).

It is likely that the Yakutat plateau experienced similar deep fracturing allowing for water to penetrate to the oceanic mantle. The distribution and amount of hydration within the oceanic upper mantle likely varies and is not precisely known; however, work by Ranero et al. (2003) suggests that outer rise faulting could produce up to 30% serpentinization in the uppermost mantle if water is always available along faults and diffuses away from the faults through a "rind" of serpentinized mantle. This study suggests that serpentinization is 3%–30% at the depth of the Moho and decreases linearly to 0% at ∼30 km past the Moho or at the thermal limit of serpentinite formation (600 °C). Another study of outer rise faulting suggests that the upper 10 km of subducting mantle contains ∼10% serpentinite or 1.2 wt% chemically bound water (Lefeldt et al., 2012).

During warm subduction, hydrous mineral phases become unstable and undergo dehydration reactions at depths less than 50 km (Hacker, 2008; Peacock, 2001; Peacock & Wang, 1999). However, typical subduction zones are colder and lose most of their water from dehydration reactions at deeper depths, coinciding with the lawsonite blueschist-eclogite transition (Abers et al., 2017; Hacker, 2008; Peacock, 1993b; van Keken et al., 2011). Slab-mantle dehydration has been tied to double zone seismicity, arc magmatism, and the transition from gabbro to eclogite in subducting slabs (Abers, 1996; Hacker, 1996; Peacock, 1993b; Rüpke et al., 2004). The stability of hydrated mineral phases is controlled by temperature and pressure conditions within the subducting slab. However, flat-slab subduction zones are colder than normal or steep subduction zones due to the combined effects of remaining at shallow depths for large distances from the trench and the lack of induced mantle corner flow (English et al., 2003). Colder conditions favor the stability of hydrous mineral phases, which are typically less dense than anhydrous mineral assemblages (i.e., Peacock & Wang, 1999). This study is focused on numerically simulating the evolving flat-slab subduction zone in southeastern Alaska in order to determine where hydrous phases may be present and how changes in mineral stability affect slab density.

Table 2.1. Physical Properties Used for Thermal Models

Material	Thermal conductivity (W/m/K)	Internal heat production (W/m^3)	Specific heat (J/(kg*K))	Thermal diffusivity (m^2/s)
Continental crust	2.2[2]	1.15x10-6[4]	800[6]	1.02x10-6
Mantle (peridotite)	2.8[3]	2x10-8[4,5]	900[6]	9.43x10-7
Oceanic crust (basalt)	1.6[1]	2x10-7[4]	800[6]	7.14x10-7

Note. Thermal diffusivity was calculated from the specific heat and thermal conductivity values shown. References: [1] Mostafa et al. (2004), [2] Hartlieb et al. (2016), [3] Keleman et al. (2004), [4] Hasterok and Webb (2017), [5] Hasterok and Chapman (2011), and [6] Waples and Waples (2004).

Table 2.2. Major Element Compositions and Solution Models Used for This Study

Major oxide	Yakutat basalt	MORB basalt	Gabbro	Peridotite DMM	cont crust	solution models for basalts	solution models for gabbro	solution models for peridotite	solution models for continental crust
Na_2O	4.21	2.79	3.65	0.13	3.40	Bio(HP)[1]	Ep(HP)[1]	Ep(HP)[1]	Bio(HP)[1]
MgO	7.75	7.58	8.02	38.74	3.60	Chl(HP)[2]	Chl(HP)[2]	Chl(W)[14]	Mica(CHA1)[3,4]
Al_2O_3	15.77	14.70	16.78	3.98	15.02	Cpx(HP)[5]	Cpx(HP)[5]	Cpx(HP)[5]	Pl(h)[6]
SiO_2	49.52	50.47	52.52	44.72	63.60	Gt(WPH)[7]	Gt(WPH)[7]	Gt(WPH)[7]	San[8]
CaO	8.32	11.39	11.45	3.18	5.26	Mica (CHA1)[3,4]	Mica (CHA1)[3,4]	Atg(PN)[13]	Cpx(HP)[5]
TiO_2	1.57	1.68	0.59	0.13	0.69	O(HP)[9]	O(HP)[9]	O(HP)[9]	GlTrTsPg[10,11]
MnO	0.19	0.18	0.11	0.13	0.10	GlTrTsPg[10,11]	GlTrTsPg[10,11]	GlTrTsPg[10,11]	Gt(HP)[9]
FeO	6.72	8.76	4.74	8.02	6.03	Pl(I1,HP)[12]	Pl(I1,HP)[12]	Pl(I1,HP)[12]	
Fe_2O_3	5.06	1.86	1.00	0.18	-	Opx(HP)[5]	Opx(HP)[5]	Opx(HP)[5]	
K_2O	0.624	0.16	0.10[a]	-	2.30	San[8]		Sp(HP)[1]	
						Ep(HP)[1]			

Note. Bulk compositions used in *Perple_X* simulations of basalts (upper crust), gabbro (lower crust), peridotite (slab mantle), and continental crust. Solution models used within *Perple_X* for each composition are also given. References: [1] Powell and Holland (1999), [2] Holland and Powell (1998b), [3] Auzanneau et al. (2010), [4] Coggon and Holland (2002), [5] Holland and Powell (1996), [6] Newton et al. (1980), [7] White et al. (2000), [8] Waldbaum and Thompson (1968), [9] Holland and Powell (1998a), [10] Wei and Powell (2003), [11] White et al. (2003), [12] Holland and Powell (2003), [13] Padron-Navarta et al. (2013), and [14] White et al. (2014). Abbreviation: MORB, mid-ocean ridge basalt.
[a] Note that K_2O is excluded from the system in our simulations of gabbro due to the small amount of potassium present in the bulk composition. For this reason, we do not use San or Bio(HP) solution models in the simulations of gabbro.

2.6 METHODS

2.6.1 Numerical Thermal Modeling

For this study we utilized two different programs to model thermal conditions in 2D within the modern southeastern Alaska subduction system. We used version 3.4 of the finite difference code *Thermodsubduct* (an updated version of *Thermod7*) (Hoisch, 2005) to simulate time-dependent evolution, and a finite element code, *PGCTherm2D*, written and developed by Jiangheng He at the Pacific Geoscience Centre in British Columbia, to simulate steady state conditions. It is important to note that *PGCTherm2D* can only produce steady state models, whereas *Thermodsubduct* iterates and evolves through time and can produce outputs at any requested time interval. Models run in both programs used the same inputs and conditions to the extent possible: the same subduction geometry, physical properties, fault velocity, frictional coefficient, and mantle convection (corner flow) geometry. Due to the relatively young age of the southeastern Alaska subduction system, we used the results calculated by *Thermodsubduct* in our calculation of slab dehydration, and the steady state models calculated by *PGCTherm2D* for comparison and benchmarking to the extent possible, recognizing that differences in boundary conditions and steady-state versus non-steady state result in predictable differences. The models were constructed to simulate an 850-km transect across the southeastern Alaska subduction zone (A–A′ in Figure 2.1a). The subduction fault geometry was set to match the Wadati-Benioff seismicity zone (see Figure 2.1b). For all models, the fault velocity was assumed to be 5 cm/yr based on geodetic studies of Alaska (Christeson et al., 2010; Fletcher & Freymueller, 1999; Veenstra et al., 2006).

Past studies have indicated the dip of the flat-slab region to be between 6° and 11° (Bauer et al., 2014; Worthington et al., 2012). For the numerical simulations, a 7° dip was assumed for the portion of the system that extends from the trench, which is located 150 km from the left boundary of the models, to about 50 km depth (550 km from the left boundary), where the dip steepens to 24°.

For both thermal modeling approaches, we assume an 80 km thick slab (Kumar & Kawakatsu, 2011; O'Driscoll & Miller, 2015) where the top 20 km is oceanic crust and the underlying oceanic lithosphere is peridotite. The Alaskan continental crust is assumed to be 35 km thick with an underlying rigid mantle lithosphere of peridotite composition to 50 km depth. Peridotite is also assumed in the convection region (below the rigid lithosphere) at depths greater than 50 km on the right side of the models. All thermodynamic properties used are listed in Table 2.1.

It is important to note that our thermal model assumes a constant continental crustal thickness of 35 km across the Alaskan continent. However, there is variability in crustal and lithospheric thickness throughout the continent. Near Denali the crust is likely thicker than 35 km (Veenstra et al., 2006). Receiver function studies have suggested that in the central Alaska Range region the crustal thickness ranges between 35 and 45 km, and that just north of the range the thickness is around 26 km, although this is towards the end of our 850 km transect (Veenstra et al., 2006). Towards the southern end of our transect, Moho depths are closer to 30 km (O'Driscoll & Miller, 2015). This variation in crustal thickness should not significantly affect the conditions predicted for the subduction channel and oceanic lithosphere in our numerical simulations of the thermal evolution.

2.6.2 Finite Difference Thermal Modeling

The *Thermodsubduct* code utilizes finite difference methods to solve 2D forward models of changing temperature conditions subject to specified initial conditions, boundary conditions, and fault geometry. Frictional heating along the fault and induced mantle convection (truncated corner flow) were also incorporated into the models (see Figures A1b and A2 for model setup). *Thermodsubduct* uses a regular staggered Eulerian grid for the simulation of advection in incompressible flow, following Leveque (1996). A flux limiter (Roe, 1985) is utilized within the advection code to limit the amount of undershoot and overshoot that may be calculated at each point, resulting in the preservation of sharp boundaries in physical arrays such as occur along faults, and suppressing the tendency for spurious oscillations to develop, which are common with less sophisticated methods.

Models were run in *Thermodsubduct* on a regular grid consisting of 101 rows and 541 columns with a spacing of 2 km, thus simulating a system with cross-sectional dimensions of 200 km by 1,080 km. Higher resolution models were run on a regular grid consisting of 201 rows and 1,086 columns with a spacing of 1 km, thus simulating cross sectional dimensions of 200 and 1,085 km. Models run in *Thermodsubduct* required a longer horizontal dimension than comparable models run in *PGCTherm2D*, which were 850 km in length, in order to simulate the same depth while also placing the mantle corner flow inflow-outflow transition at the lower left corner of the system (explained further below). The higher resolution models were run to evaluate the degree of improvement in simulating mantle corner flow, which can be challenging (e.g., van Keken et al., 2008; Wada et al., 2008; see supporting information).

Thermodsubduct simulations included induced convection (corner flow) in the asthenospheric wedge. The corner of the mantle convection domain is located at the change in subduction dip from 7° to 24°, ~550 km from the left boundary at 50 km depth. Mantle convection was calculated assuming isoviscous flow and using the stream function of Batchelor (1967). The tip of the corner was truncated vertically 608 km from the left boundary (458 km from the trench; see Figure A1b) (e.g., Currie et al., 2004). Coupling between the asthenospheric mantle wedge and the subducting slab begins at the corner truncation. It should be noted that full coupling along the subduction fault may not be entirely realistic as this portion of the fault is well defined by the seismically active zone, suggesting brittle faulting is occurring. Along the subduction fault, frictional heating was calculated assuming a frictional coefficient of 0.03 for temperatures <300 °C, de- creasing exponentially at temperatures above 300 °C (e.g., Kohn et al., 2018; see supporting information for further details). The width of the frictional heating domain was assumed to be the same as the grid spacing, as this is the minimum width that can be resolved on the grid. Benchmarking tests of *Thermodsubduct* are provided in the supporting information.

2.6.3 Finite Element Thermal Modeling

PGCTherm2D performs simulations of steady-state temperatures within 2D representations of subduction zones using the finite element method (e.g., Currie et al., 2004; Gutscher & Peacock, 2003; Gutscher et al., 2016; Wada & Wang, 2009). Models calculated using *PGCTherm2D* have been tested versus other finite element models in a community benchmarking exercise (van Keken et al., 2008). Within *PGCtherm2D*, a constant temperature boundary condition is applied to the top and left boundaries (Figure A1a). A constant temperature condition is assumed for the right-side boundary from the surface downward through the portion of the mantle convection domain where material is moving toward the trench (Figure A1a). Below this, where material is moving away from the trench, a zero heat-flux boundary is assumed (Figure A1a). Note that models run in Thermodsubduct handle the change in boundary condition at this point by extending the model further to the right so that this transition occurs at the lower right corner of the 2D array, rather than along the right-side boundary.

In models run by *PGCTherm2D*, the bottom boundary of the model domain occurs at 80 km depth within the oceanic lithosphere and maintains a constant temperature of 1,450 °C, following Stein and Stein (1992) (Figure A1a). The models incorporate the effects of shear heating along the subduction interface for a frictional coefficient of 0.03 (e.g., Kohn et al., 2018; Wada & Wang, 2009; Wada et al., 2008). The models also include induced convection (corner flow) in the asthenospheric wedge defined identically as in the *Thermodsubduct* models. The fault geometry of models run in *PGCTherm2D* is also identical to models run in Thermodsubduct. The width assumed for the frictional heating domain was assumed to be 2 km, to match the width specified in the Thermodsubduct models with 2 km grid spacing.

2.6.4 Boundary Values, Initial Conditions, and Simulated Time

For models run in *PGCTherm2D* the initial left (oceanic side) boundary is a stable geotherm from 0 to 80 km depth that was calculated numerically using the physical properties from Table 2.1, layer thicknesses in Figure 2.3, and boundary constraints from Stein and Stein (1992) for the oceanic lithosphere: constant temperatures of 0 °C and 1,450 °C at depths of 0 and 80 km, respectively. The left boundary for the Thermodsubduct models uses these same values for 0–80 km, then continues to greater depth assuming an adiabatic gradient of 0.3 °C/km (Turcotte & Schubert, 1982), as done in Stein and Stein (1992). On the continental side, the initial right-side boundary is a stable geotherm between 0 and 150 km calculated numerically using physical properties from Table 2.1, layers thickness shown in Figure 2.3, and assuming a constant temperature boundary at the surface of 0 °C and a constant heat flux boundary at 150 km depth of 4.0 × 10−7 cal/cm2s. Depths >150 km assume an increase in temperature of 0.3 °C/km, as described above.

Within the 2D model domain, the initial temperatures for the *PGCTherm2D* models are set to 0 °C through- out. Non-zero steady-state temperatures develop within the system (except at the top boundary, which is fixed to a constant temperature of 0 °C) during the run, which was set to simulate 10^{20} years of elapsed time to assure thermal equilibration.

The initial temperature array for the *Thermodsubduct* models consists of two domains spatially separated by the fault trace. The initial temperatures for the oceanic side comprise the same geotherm as used for the left- side boundary, and the initial temperatures for the continental side comprise the same geotherm as used for the right-side boundary. Models were run with a time-step of 25,000 years out to 20 m.y. (800 iterations), which allowed the leading edge of the oceanic slab to migrate all the way through the system past the lower boundary at 200 km depth.

2.6.5 Modeling of Stable Mineral Assemblages and Slab Density Using *Perple_X*

Perple_X (Connolly, 2005) version 6.7.9 was utilized to calculate stable mineral assemblages in the oceanic crust and hydrated upper mantle for Alaska's flat-slab subduction system based on thermal modeling outputs. Calculations used pressure-temperature conditions obtained from the 20 m.y. output of the *Thermodsubduct* model with 2 km spacing. *Perple_X* calculates stable mineral assemblages given a user-specified bulk composition and specified pressure-temperature ranges, solution models, and thermodynamic data set. In order to model stable mineral assemblages within the subducting slab, we chose several bulk compositions for our models that represent the upper oceanic crust, a gabbroic composition for the middle and lower crust, a depleted MOR (mid-ocean ridge) mantle peridotite composition, and a continental crust composition (which we used only for calculating 2D pressure and density grids).

To represent the upper 5 km of oceanic crust, we ran calculations using two different basalt compositions. The first is the composition of the Yakutat basalt in Alaska, based on the average of chemical analyses of 19 ocean drill samples reported in Davis and Plafker (1986). The chemical analyses included determinations of both Fe2+ and Fe3+ oxides. The second basalt composition is based on data taken from a global catalog of 771 ocean ridge segments (excluding back-arc basin samples), and represents average depleted mid-ocean ridge basalt (MORB) (Gale et al., 2013). Fe oxide wt % values for these analyses are reported as FeO_{TOTAL}, which we adjusted to Fe_2O_3 and FeO using the $Fe^{3+}/\sum Fe$ ratio for MORB melt from Cottrell and Kelley (2011).

For the lower 15 km of subducting oceanic crust, we assumed a gabbroic composition determined by averaging the compositions of 176 oceanic gabbro samples from Niu et al.

(2002). We adjusted their reported weight % values of FeO_{TOTAL} to Fe_2O_3 and FeO again using the $Fe^{3+}/\sum Fe$ ratio from Cottrell and Kelley (2011).

We use the depleted MOR mantle (DMM) peridotite composition from Workman and Hart (2005) for the simulation of mineral stabilities below the slab Moho (20 km depth). This study reported modal abundances of spinel, orthopyroxene, clinopyroxene, and olivine and all Fe as FeO_{TOTAL}. We used the reported $Fe^{3+}/\sum Fe$ ratios and modes for spinel, clinopyroxene, and orthopyroxene in peridotites reported in Wood- land et al. (2006) to convert the weight % values of FeO_{TOTAL} in the Workman and Hart (2005) peridotite DMM composition to Fe_2O_3 and FeO. Finally, we used bulk composition data from Rudnick and Gao (2003) for the continental crust.

Bulk compositions and mineral solution (a-X) models used in the calculation of isochemical plots by *Perple_X* are given in Table 2.2. The goal in choosing mineral solution models was to incorporate Fe^{3+} and Mn in minerals while also avoiding models that create excessive burdens on the computation. The chlorite solution model Chl(W) is used in the simulation of peridotite, whereas Chl(HP) is used in the simulation of basalts and gabbro. Chl(W) incorporates Fe^{3+} but is computationally taxing, whereas Chl(HP) does not incorporate Fe^{3+} and is less computationally taxing. The basalt and gabbro simulations involve a larger number of solid solution phases than the peridotite simulations and therefore also involve a larger number of a-X models. Incorporation of the Chl(W) model in the simulations of basalts and gabbro proved too computationally taxing, so we used the simpler Chl(HP) solution model. We do not think this significantly affected our results as the amount of Fe^{3+} that is incorporated into chlorite is very small.

All calculations were done using the *Perple_X* data set HP11ver (Holland & Powell, 2011). The chemical system assumed for the simulation of basalt compositions was K_2O-Na_2O-MgO-Al_2O_3-SiO_2-CaO-TiO_2- MnO-FeO-Fe_2O_3 ± H_2O. For gabbro and peridotite it was Na_2O-MgO-Al_2O_3-SiO_2-CaO-TiO_2-MnO-FeO- Fe_2O_3 ± H_2O, and for the continental crust it was Na_2O-MgO-Al_2O_3-SiO_2-CaO-TiO_2-MnO-FeO ± H_2O. H_2O was added for runs in which water-saturated conditions were simulated.

The selected a-X models include Mn-bearing components for chlorite, biotite, garnet, and olivine, but not for other solid solution phases in which it would be expected to occur in small but detectable amounts (muscovite, orthopyroxene, clinopyroxene, and amphibole). The inability of the simulations to distribute Mn throughout all of these phases could lead to over-stabilization of phases containing Mn-bearing components. However, our *Perple_X* simulations predict low values for the spessartine component of garnet ($X_{spss}^{Grt}<0.04$) for the majority of garnet produced. A small amount of low-temperature garnet (<2 vol. %) is produced with $X_{spss}^{Grt}>0.04$ that may not be realistic. However, this does not significantly affect our slab density calculations.

The continental crust calculation is only used to calculate complete 2D pressure and density grids, and its use is limited to the upper right 35 km of our cross section (see Figures 2.1 and 2.3). We therefore did not adjust for Fe^{3+} in its major element composition as any slight variations in continental crust composition do not affect calculations of slab density. Values of weight % K_2O were negligible in our gabbroic and peridotite compositions and were therefore excluded from our phase equilibria calculations.

We simulated mineral stabilities for both basalt compositions, the gabbro, and the peridotite for both water-saturated and completely anhydrous conditions within each layer of the oceanic slab from 350 to 850 km along transect A–A' (Figure 2.1). The pressure and temperature conditions used for these calculations correspond to depths within the oceanic lithosphere of 5 km for basalt, 15 km for gabbro, and 25 km for peridotite. Temperature conditions were extracted from model runs of *Thermodsubduct* for 20 m.y. of elapsed simulated time, and from *PGCTherm2D* models (steady state) (Figure 2.2). Density was calculated using P-T conditions from our modeling results. To calculate density, at each grid point, we input temperatures from our thermal models and calculated pressures into our models of stable mineral assemblage. In our pressure calculations, we started by estimating densities at the surface and then progressed downward using the calculated densities of the overlying layers. This was done so that pressure estimates incorporated the density calculations for stable mineral assemblages generated by *Perple_X*. The code used to calculate pressure and slab density is available in Data Set S1 (https://doi.org/10.5281/zenodo.4670347). By 20 m.y. of simulated time, the *Thermodsubduct* solution had not attained a steady state but is similar to *PGCTherm2D*'s steady-state solution. This is discussed in greater detail in the supporting information. The results of the water-saturated simulations are shown in Figure 2.4 (Yakutat basalt), Figure 2.5 (depleted MORB), Figure 2.6 (gabbro), and Figure 2.7 (peridotite).

Slab density was calculated along the transect using the 2D density grids built using *Perple_X* outputs. Our slab density calculations (Figure 2.8) were run for the two thermal models, and using the predicted densities for each basalt composition, gabbro, and DMM peridotite. Figure 2.8 shows a comparison of predicted slab densities for a completely anhydrous slab, completely saturated slab (with saturation occurring completely in the 20 km of oceanic crust and the upper 10 km of the subducting mantle), and a hybrid model (using a weighted average of the saturated and anhydrous results). For the hybrid model, we calculated density by using a weighted average of saturated and anhydrous densities. This weighting is designed to predict densities assuming that hydration was introduced along fracture networks (i.e., Prigent et al., 2020; Ranero et al., 2003) while unfractured areas remained anhydrous.

Within the upper 5 km of the subducting crust, we assume 25% is saturated, which equates to ~1.5 wt% H_2O (less than the 3 wt% H_2O recommendations for the oceanic crust in

Hacker et al. [2003] and Rüpke et al. [2004]). We assume the lower gabbroic crust (from 5 to 20 km depth) is somewhat less hydrated, and weighted 20% to the saturated gabbro model, which equates to ~1 wt% H_2O. Within the upper 10 km sub- ducting slab mantle, we weighted 15% to the saturated peridotite model, resulting in ~1 wt % H_2O. Each point plotted in Figure 2.8 was calculated by averaging the density of the slab at each kilometer along the transect, and displays results for each of the two thermal models and each of the two basalt compositions for our anhydrous, hybrid, and saturated slabs. Our *Perple_X* simulations of mineral assemblages (Figures 2.4–2.7) predict that densification due to metamorphic dehydration reactions begins hundreds of kilometers past the trench. For this reason, we assumed an unaltered crust in all of our modeled calculations before the trench, and until temperatures are greater than 250 °C and 0.5 GPa. These conditions occur at the top of the crust before 350 km across our A–A′ transect (Figure 2.1), and our results are therefore presented after 350 km in Figures 2.4–2.9. All calculated anhydrous assemblages are included in the Data Set S1 (https://doi.org/10.5281/ zenodo.4670347).

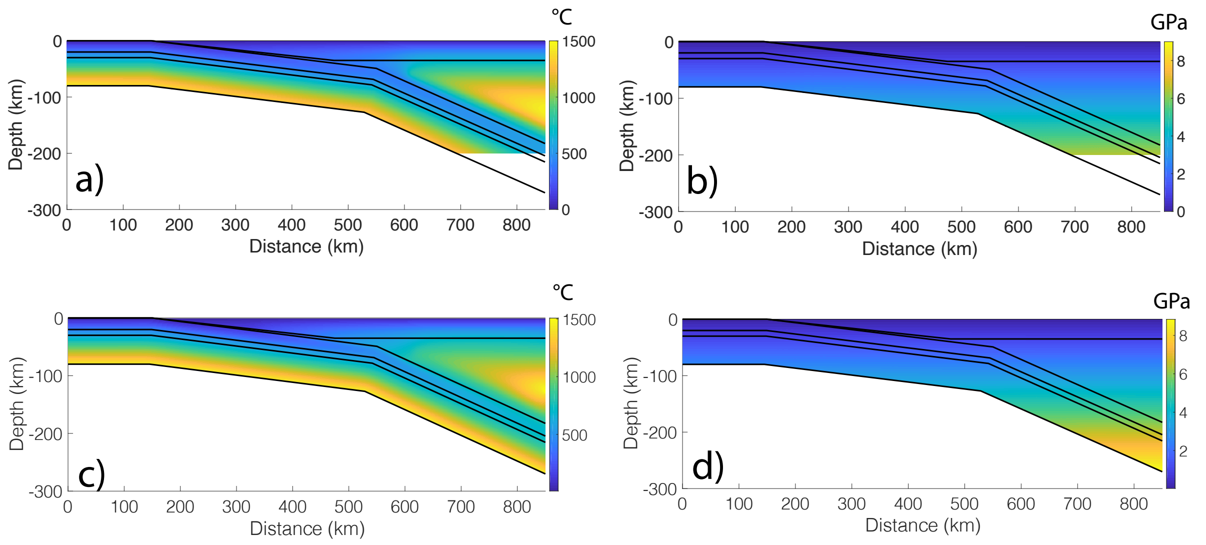

Figure 2.2. Temperature and pressures calculated for the southern Alaska subduction system from numerical simulations. (a and b) Conditions were determined from the Thermodsubduct

model calculated for 20 m.y. (c and d) Conditions were calculated from the *PGCTherm2D* steady state model. All panels plot results along the A–A′ transect (Figure 2.1).

2.7 RESULTS

Numerical simulations produced by *Thermodsubduct* (for 20 m.y.) and *PGCTherm2D* (steady state) for the southern Alaska subduction system are shown in Figure 2.2. A more detailed comparison between the finite difference (*Thermodsubduct*) and finite element (*PGCTherm2D*) thermal modeling codes, as well as a presentation of results with and without shear heating incorporated for each model is presented in the supporting information (Figure A6). The two thermal modeling programs generally agree with each other, with differences attributable to steady-state versus non-steady state, slight differences in boundary conditions, and different resolutions. Differences between the models generated by the two methods (explained in more detail in the supporting information) are subtle and do not alter the conclusions of this study.

The Yakutat subduction system lacks exposures of exhumed metamorphic rocks from the subduction zone, thus requiring conditions within the subduction zone to be inferred by means other than petrologic analysis. Our numerical simulations predict conditions within the Yakutat subduction zone that are colder than those found in average subduction zones, as judged from the rock record (e.g., Penniston-Dorland et al., 2015). The relatively cold conditions stabilize glaucophane and lawsonite assemblages, as opposed to lawsonite-absent assemblages containing sodic-calcic amphibole or calcic amphibole that are characteristic of average or warm subduction zones (Hernández-Uribe & Palin, 2019a). Our models predict assemblages in agreement with petrologic models that predict talc and lawsonite assemblages along cold subduction geotherms (Hernández-Uribe & Palin, 2019b). The Yakutat system may be similar to the Laramide flat-slab system, for which cold slab-top conditions are indicated by lawsonite eclogite xenoliths collected from diatremes in the Colorado Plateau (Hernández-

Uribe & Palin, 2019b; Usui et al., 2003). Lawsonite eclogites are also predicted in our simulations of basalt and gabbro in the Yakutat subduction system (Figures 2.4–2.6).

However, there are also examples of flat-slab or shallow angle subduction systems predicted to be consistent with average or warm conditions (e.g., Cascadia and Guerrero systems; Condit et al., 2020). While there are many factors that influence temperatures within subduction zones (e.g., van Keken et al., 2018), the principal reason the Yakutat system is cold is likely due to its shallow dip (7°) extending a long distance (400 km) from the trench before steepening to a still shallow angle of 24° (Figure 2.1). Hotter conditions are predicted for the Cascadia and Guerrero systems due to steeper subduction angles in these regions, which results in warmer conditions closer to the trench.

Our water-saturated simulations of mineral stability (Figures 2.4–2.7) were calculated along the A–A′ transect (Figure 2.1) from 350 to 850 km using the Thermodsubduct 20 m.y. results. From 0 to 350 km, due to sub-greenschist facies conditions in the oceanic lithosphere and kinetic impediments to low-temperature hydration reactions, free water held in pores and cracks may remain largely unreacted in the rocks. Much of this water is considered to be released at the trench through compaction in the earliest stages of subduction, following updip migration along the subduction channel (e.g., Bebout & Penniston-Dorland, 2016; Moore & Saffer, 2001; Peacock, 1990; Saffer & Bekins, 1998; Saffer & Tobin, 2011). As the oceanic crust is subducted and temperatures rise, we expect that kinetic impediments to hydration are increasingly overcome, and as a result, hydration reactions should progress to a greater degree assuming free water continues to be available for reaction. We consider that by 350 km along the transect, rocks have attained temperatures sufficient to overcome kinetic impediments. Hydration may occur either by reaction of free water that persists within pores and cracks following compaction, or by water migrating updip within the subduction channel released by metamorphic dehydration reactions at greater depth (Bebout, 1991; Bebout & Penniston-Dorland, 2016; Jaeckel et al., 2018).

Perple_X simulations of both basalt compositions (Figures 2.4 and 2.5) yield stability fields for assemblages involving the hydrous mineral phases lawsonite, mica (strongly phengitic muscovite), chlorite, talc, and amphibole (glaucophane). In addition, a small stability field for biotite (phlogopite) is present in the simulation of the Yakutat basalt but not MORB basalt. The Yakutat basalt (Figure 2.4) has relatively higher amounts of mica (phengitic muscovite) and clinopyroxene (aegirine-augite in the Yakutat basalt, augite in the MORB) compared with the MORB (Figure 2.5). These differences can be attributed mainly to sea-floor alteration of the Yakutat basalt, which resulted in higher weight percentages of K_2O and Fe_2O_3 compared to depleted MORB (see Table 2.2). For both basalt compositions, the same major dehydration reaction is observed be- tween 650 and 700 km across the transect (~450 °C, 3.0 GPa), where chlorite and amphibole react to form garnet (dominantly almandine), clinopyroxene and talc to produce a talc lawsonite eclogite. Free water is released in this reaction, but some water is still held in lawsonite, muscovite, and newly formed talc. This same dehydration reaction occurs at 680 km across the transect (~480 °C, 3.8 GPa) for gabbro (Figure 2.6).

In the MORB, clinopyroxene becomes more enriched in Na and Al as temperature and pressure increase along the transect, resulting in a transition from augite to omphacite. In the Yakutat basalt, the clinopyroxene remains aegirine-augite throughout the entire range of PT conditions in our transect. Aegirine-augite is stabilized in the Yakutat basalt by the higher Fe^{3+}/Fe^{2+} ratio in the bulk composition as clinopyroxene is the primary host for Fe^{3+} in these rocks. We note that in the MORB (Figure 2.5), a small stability field for orthopyroxene (ferrosilite) is present at 650–700 km (~450 °C, 3.0 GPa).

Assemblages simulated for water-saturated gabbro (Figure 2.6) are similar to those predicted for the MORB (Figure 2.5). Water is held in amphibole (glaucophane), chlorite, and lawsonite until ~680 km across the transect (~480 °C, 3.8 GPa). Dehydration of the lower crust results in garnet (dominantly almandine) and clinopyroxene. Similar to the MORB, clinopyroxene becomes increasingly more Na- and Al-rich along transect, transitioning from augite to omphacite. At 680–850 km along the transect (~480–550 °C, 3.8–6.3 GPa), hydration is held in lawsonite and talc.

The simulation of water-saturated peridotite (Figure 2.7) predicts hydration by reactions that stabilize antigorite and chlorite, yielding a serpentinite. These minerals are in high abundance and have a strong effect in lowering the density of the rock. Hydrous mineral assemblages in the upper mantle can hold up to 8 wt% H_2O, which is significantly higher than our estimates for the upper crustal basalt (up to 5.5 wt%) and lower crustal gabbro (up to 5 wt%). Dehydration of the mantle lithosphere occurs at 700–750 km across the transect (~600 °C, 4.5 GPa), yielding an entirely anhydrous assemblage of olivine, garnet (pyrope), clinopyroxene (diopside), and orthopyroxene (enstatite), consistent with a garnet lherzolite.

The results of our slab density calculation are shown in Figure 2.8 for an anhydrous slab (shown in mauve), a saturated slab (shown in blue, and only saturating the crust and upper 10 km of lithospheric mantle), and our hybrid slab (shown in green) that represents a mix of saturated and anhydrous components yielding a bulk hydration of 1–1.5 wt% H_2O for the crust and upper 10 km of the mantle. A plausible range for upper mantle densities is shaded in red for reference (Figure 2.8). Calculated densities using both basalt compositions are very similar. Calculations using the Yakutat basalt produces slightly lower densities than the MORB. Both thermal models produced similar results (Figures 2.2, A6, and A8), although the calculated slab densities for the water-saturated case noticeably diverge between 550 and 700 km along transect, where dehydration reactions cause densification of the crust. The divergence is due to lower temperatures produced within the subduction channel in the *Thermodsubduct* model. This results in dehydration reactions (and densification) occurring higher in the subduction channel in the *PGCtherm2D* model.

Comparing each set of results in Figure 2.8, we note that the calculated slab density for the anhydrous case (red) is denser than the mantle starting at ~350 km across the transect (200 km from the trench). We note that the angle of subduction steepens at 550 km across the transect, which coincides with the approximate point where the slab density in our hybrid model (~1–1.5 wt % H_2O) exceeds that of the underlying asthenosphere. The water-saturated case (blue) produced the lowest density slab. We present this in Figure 2.8 to show the upper bound for the effect of hydration on slab density, and do not consider the fully saturated case to be plausible in nature.

In Figure 2.9, we show the density (9a) and wt% H_2O (9b) in cross section along A–A' (Figure 2.1) for our hybrid (1–1.5 wt% H_2O) model (synonymous with the green lines plotted in Figure 2.8). The density of the crust increases with subduction due to increasing pressures and temperatures, and greatly increases after full eclogitization (~650 km across transect), coinciding with the crustal dehydration observed in Figure 2.9b. The slab mantle maintains a high degree of hydration to greater depth. Dehydration is predicted to occur in this layer between 600 and 800 km in Figure 2.9b, which greatly reduces the density of the upper slab mantle (observed in Figure 2.9a). The slab mantle completely dehydrates by 800 km along transect, while lower temperatures in the crust allow for some hydrous assemblages to remain stable past 850 km along transect. Eclogitization of the crust, however, increases its density to over 3,500 kg/m^3 (see Figure 2.9a).

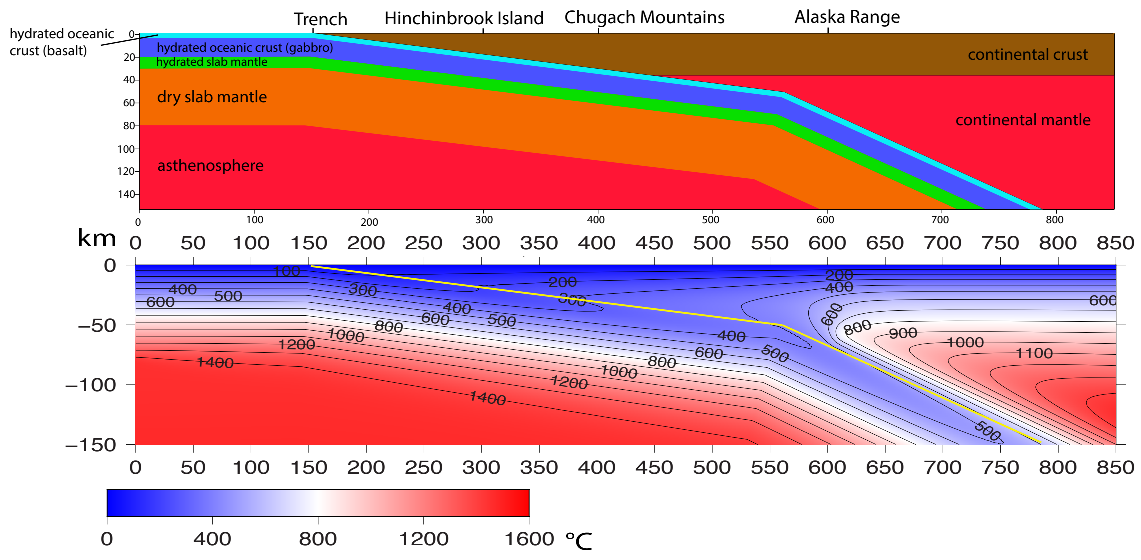

Figure 2.3. Model geometry showing layer thicknesses used in the model setup (top), and thermal profile after 20 m.y. of subduction (bottom) calculated using *Thermodsubduct* with 2 km resolution. Layer thicknesses are consistent with those used in slab density calculations (Figure 2.1). Upper basaltic crust layer is 5 km thick (cyan), and is underlain by 15 km of gabbroic lower crust (dark blue). Top 10-km of oceanic mantle is considered to be partially hydrated (green) and is underlain by anhydrous mantle (orange). Total slab thickness is 80 km. Model incorporates shear heating (effective frictional coefficient of 0.03) and isoviscous mantle cornerflow with vertical truncation of the corner flow domain at 608 km (Figure A1b). Yellow line shows the position of the fault.

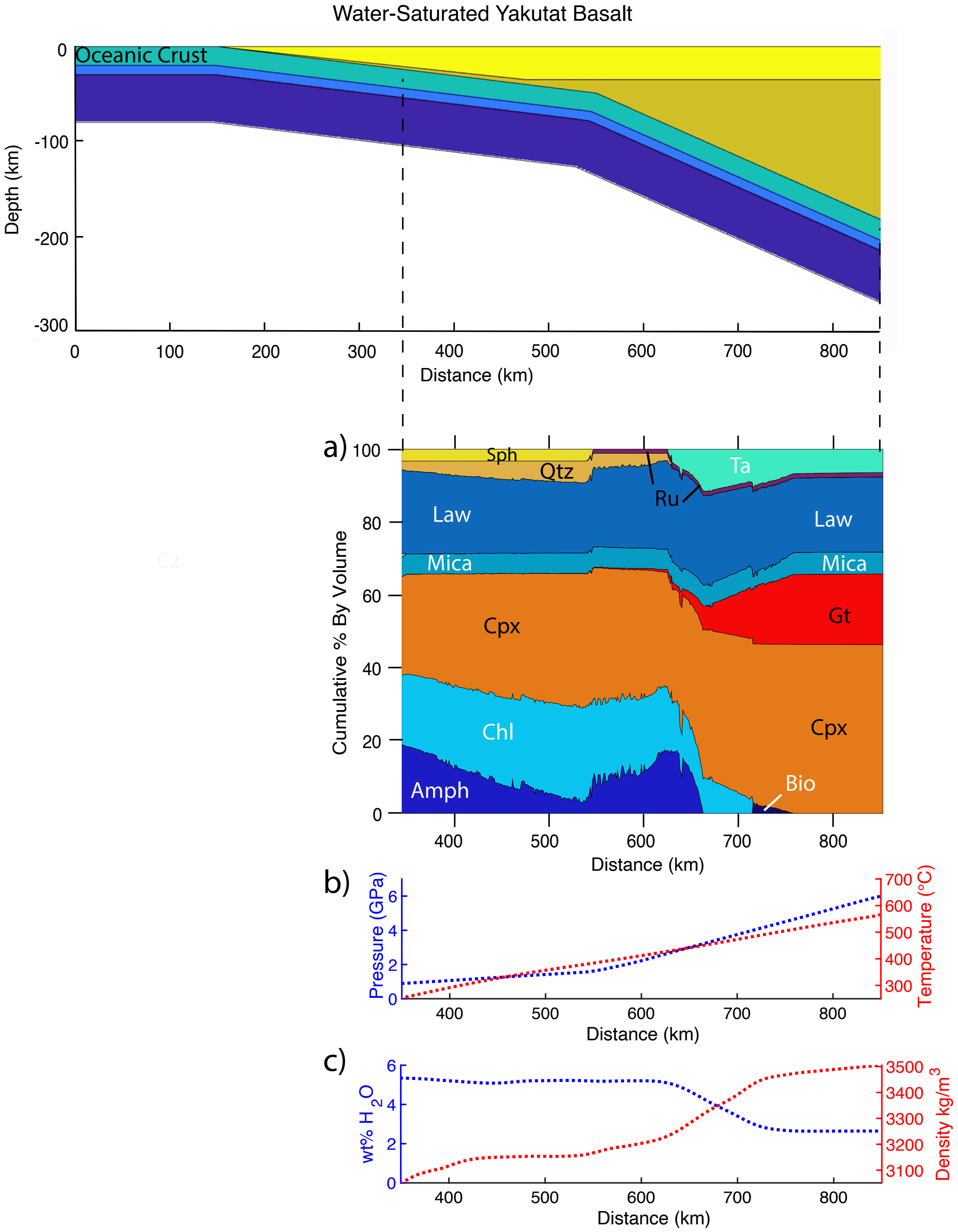

Figure 2.4. Stable mineral assemblages calculated using *Perple_X* for the Yakutat basalt composition assuming water saturation. The top diagram is shown for spatial reference. (a) Predicted minerals plotted as cumulative % by volume versus distance along transect. Hydrous mineral phases are designated by cool colors and white labels, and anhydrous mineral phases are designated by warm colors and black labels. Qtz = quartz, Ru = rutile, Gt = garnet (almandine), Cpx = clinopyroxene (aegirine-augite), Sph = sphene, Amph = amphibole (glaucophane), Chl = chlorite, Law = lawsonite, Ta = talc, Mica = phengitic muscovite, Bio = biotite (phlogopite). (b) Pressure (blue line) and temperature (red line) conditions used to

generate the results in (a). Conditions represent 5 km below the subduction interface and were determined using the 20 m.y. *Thermodsubduct* model results. (c) Weight % chemically bound H_2O (blue line) and the density calculated for Yakutat basalt (red line) for conditions shown in (b).

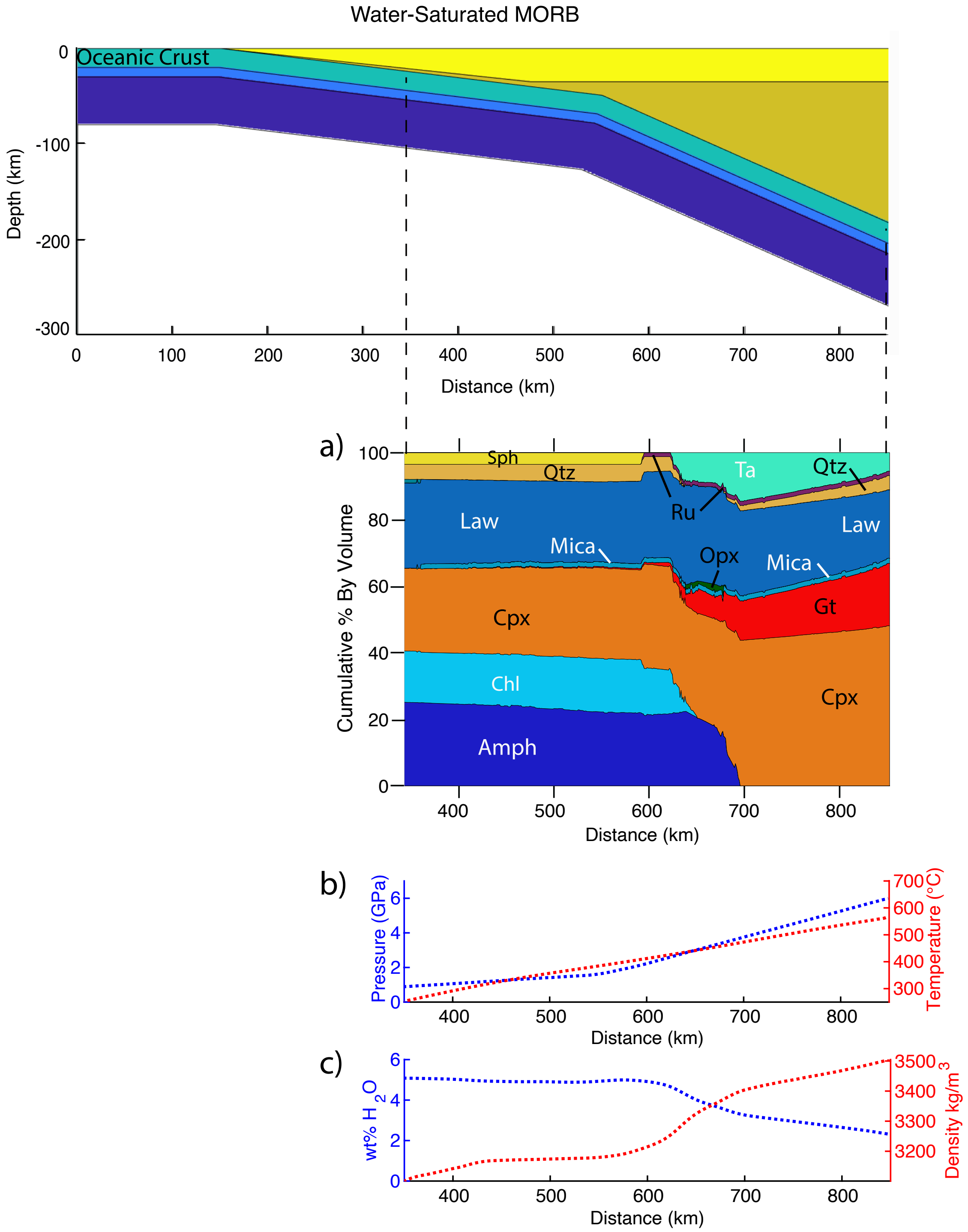

Figure 2.5. Stable mineral assemblages calculated using Perple_X for the mid-ocean ridge basalt (MORB) composition assuming water saturation. The top diagram is shown for spatial reference. (a) Predicted minerals plotted as cumulative % by volume versus distance along transect. Hydrous mineral phases are designated by cool colors and white labels, and anhydrous

mineral phases are designated by warm colors and black labels. Qtz = quartz, Ru = rutile, Gt = garnet (almandine), Cpx = clinopyroxene (augite transitioning to omphacite along transect), Opx = orthopyroxene (ferrosilite), Sph = sphene, Amph = amphibole (glaucophane), Chl = chlorite, Law = lawsonite, Ta = talc, Mica = muscovite. (b) Pressure (blue line) and temperature (red line) conditions used to generate the results in (a). Conditions represent 5 km below the subduction interface and were determined using the 20 m.y. *Thermodsubduct* model results. (c) Weight % chemically bound H_2O (blue line) and the density calculated for the MORB (red line) for conditions shown in (b).

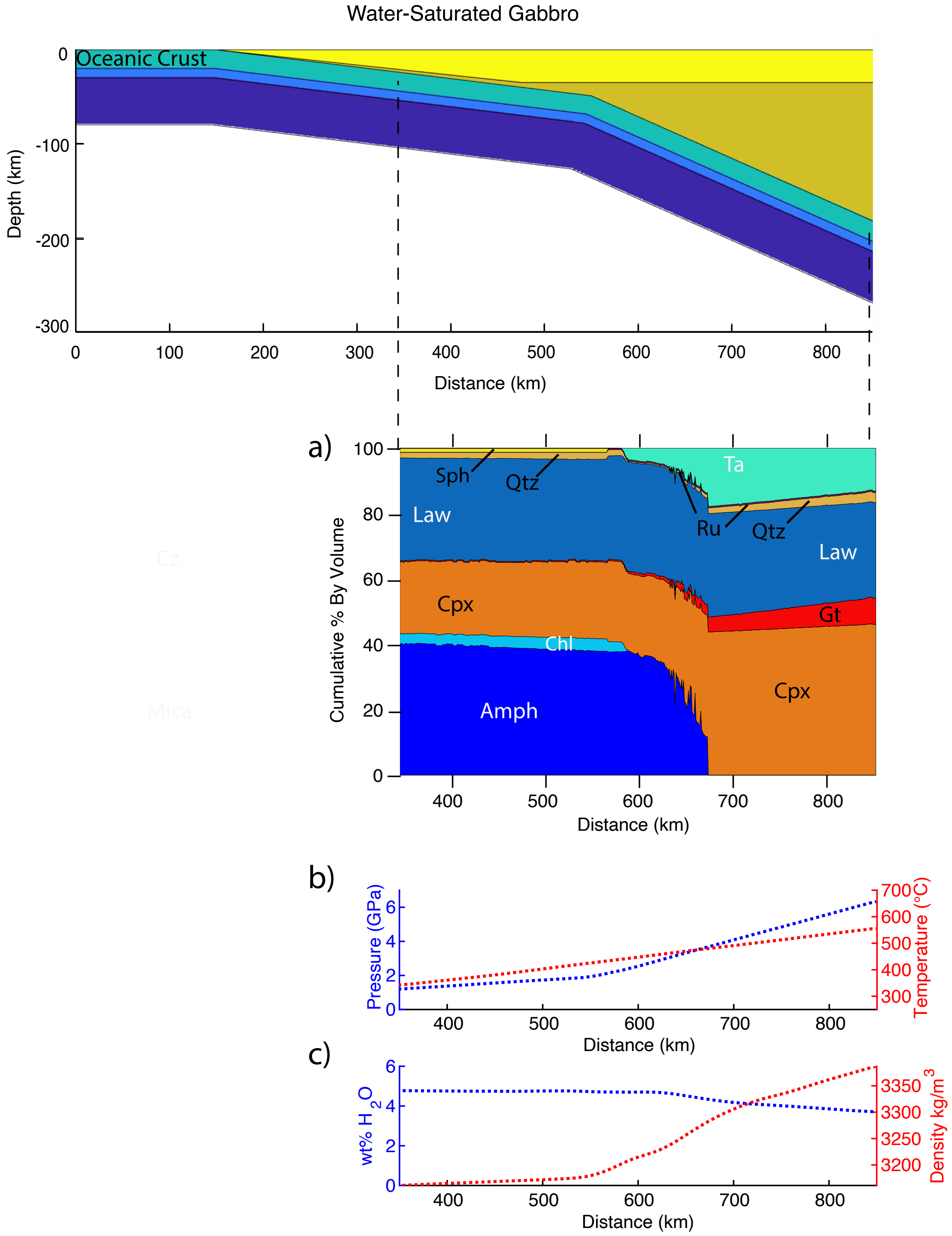

Figure 2.6. Stable mineral assemblages calculated using *Perple_X* for the gabbroic composition assuming water saturation. The top diagram is shown for spatial reference. (a) Predicted minerals plotted as cumulative % by volume versus distance along transect. Hydrous mineral phases are designated by cool colors and white labels, and anhydrous mineral phases are designated by warm colors and black labels. Qtz = quartz, Gt = garnet (almandine), Cpx = clinopyroxene (augite transitioning to omphacite along transect), Sph = sphene, Amph = amphibole (glaucophane), Chl = chlorite, Law = lawsonite, Ta = talc. (b) Pressure (blue line) and temperature (red line) conditions used to generate the results in (a). Conditions represent 15 km below the subduction interface and were determined using the 20 m.y. *Thermodsubduct* model results. (c) Weight % chemically bound H_2O (blue line) and the density calculated for the gabbro (red line) for conditions shown in (b).

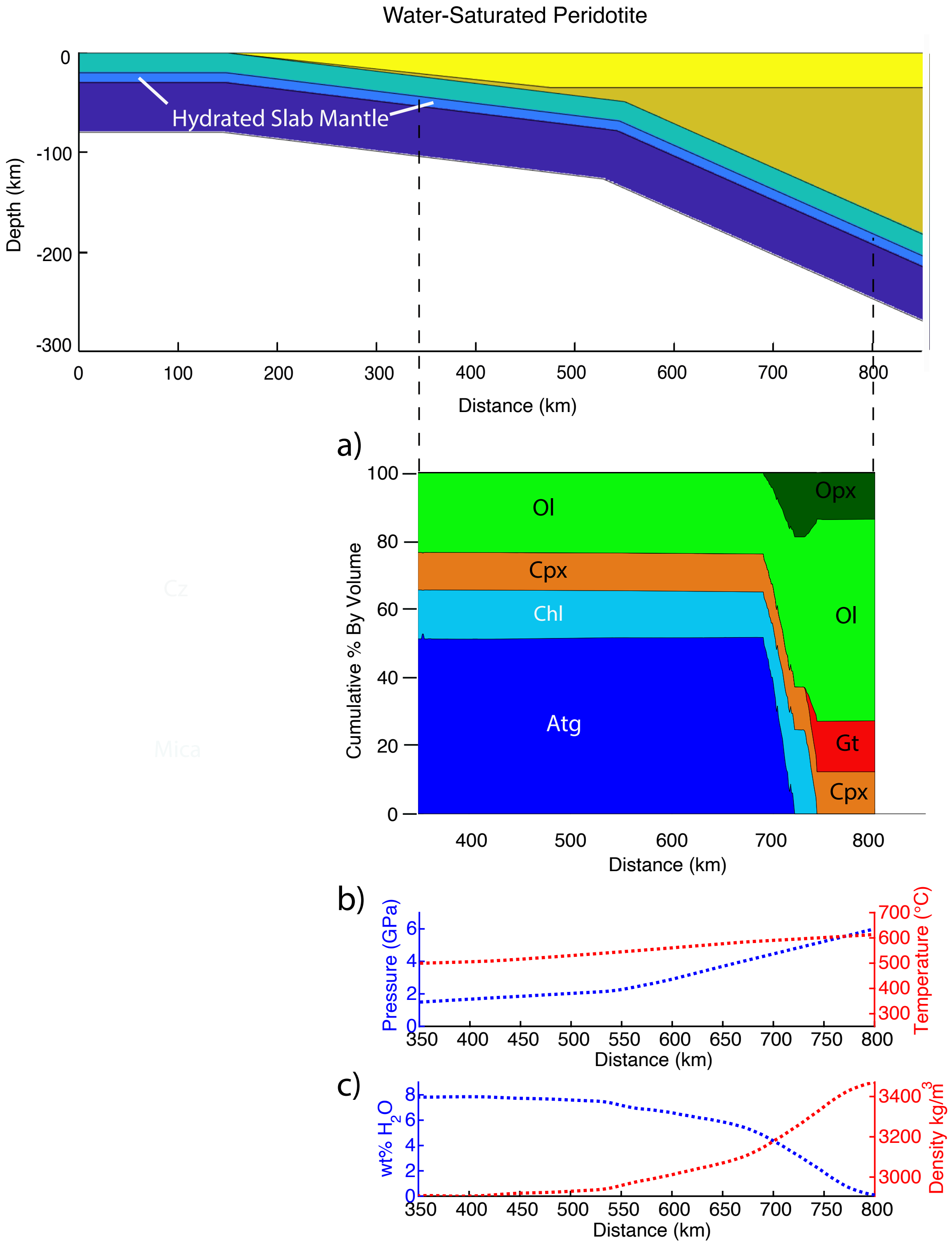

Figure 2.7. Stable mineral assemblages calculated using *Perple_X* for upper mantle depleted MOR peridotite composition assuming water saturation. The top diagram is shown for spatial reference. (a) Predicted minerals plotted as cumulative % by volume versus distance along transect. Hydrous mineral phases are designated by cool colors and white labels, and anhydrous mineral phases are designated by warm colors and black labels. Ilmenite <0.2 vol. % (not shown) is also present. Opx = orthopyroxene (enstatite), Ol = olivine, Gt = garnet (pyrope), Cpx = clinopyroxene (diopside), Chl = chlorite, Atg = antigorite (serpentinite). (b) Pressure (blue line) and temperature (red line) conditions used to generate the results in (a).

Conditions represent 5 km below the crust-mantle boundary (25 km below the subduction interface) and were determined using the 20 m.y. *Thermodsubduct* model results. (c) Weight % chemically bound H_2O (blue line) and the density calculated for the peridotite (red line) for conditions shown in (b).

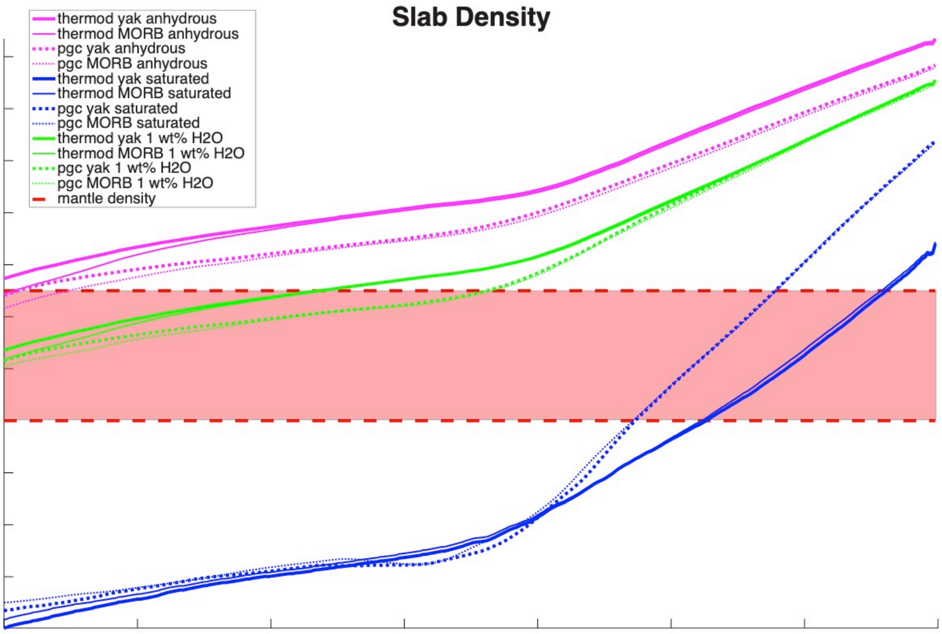
Slab Density

Figure 2.8. Slab densities versus distance along A–A' (Figure 2.1) calculated using both finite difference (*Thermodsubduct*) and finite element (*PGCTherm2D*) thermal models, and using both Yakutat basalt and MORB compositions for the upper crust. Anhydrous models are plotted in mauve, water-saturated models are plotted in blue, and hybrid models using 1–1.5 wt% H_2O in the crust and upper mantle are shown in green (see text for more details). Upper asthenospheric density is shaded in red. MORB, mid-ocean ridge basalt.

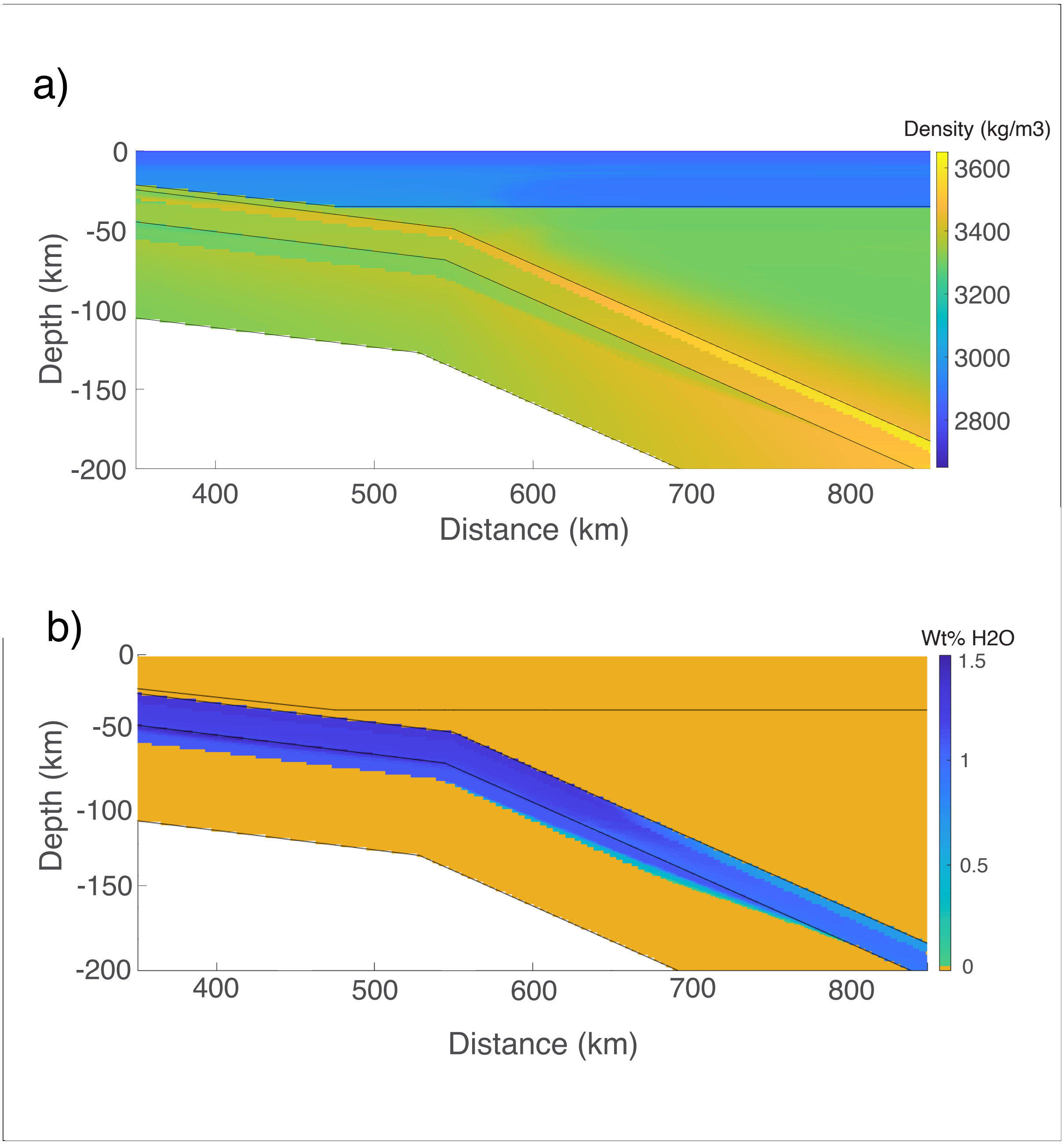

Figure 2.9. Densities (a) and wt% H_2O (b) for our hybrid model (thick solid green line in Figure 2.8) using the Yakutat basalt composition for the upper crust. Calculations used *Thermodsubduct* results.

2.8 DISCUSSION

Although the amount of water that is incorporated into the 20-km thick Yakutat crust cannot be uniquely determined, it may contain a greater degree of hydration than typical 5–15 km thick subducting oceanic crust. Because the Yakutat block is thought to have formed at the Yellowstone hotspot (Wells et al., 2014), there may have been a higher degree of thermally driven hydrothermal circulation following its formation compared to crust that forms at a typical oceanic spreading center. Also, fracturing associated with hot-spot volcanism could have contributed to an increased amount of hydrothermal circulation.

Oceanic basalt typically preserves its primary igneous chemistry with variable but generally minor alteration due to interaction with ocean water. The analyzed Yakutat basalt samples from which we derived our bulk composition were obtained from drill cores, and contain plagioclase as the dominant phenocryst phase, accompanied by minor pyroxene and in some samples olivine (Davis & Plafker, 1986). Zones of alteration in these samples contained zeolites, chlorite, K-Feldspar, albite, and epidote among others, but there is little difference in overall chemistry from a typical MORB composition (Davis & Plafker, 1986). Our calculations of slab density using *Perple_X* predict only slight differences arising from differences in the bulk chemistry of the Yakutat basalt and the MORB (see Figure 2.8).

As subduction progresses, for both basalt compositions, our models predict that metamorphism yields a glaucophane schist containing lawsonite, chlorite, phengitic muscovite, and augite (specifically aegirine-augite in the Yakutat basalt) between 350 and 650 km along transect (Figures 2.4 and 2.5). At 650–700 km across the transect, chlorite and amphibole are predicted to break down yielding a lawsonite and talc-bearing garnet eclogite. Due to the cold thermal regime typical of flat-slab subduction systems, the transition from blueschist to eclogite facies in the basaltic upper crust is predicted to occur almost 500 km from the trench. This delay in eclogitization is a large contributor to slab buoyancy in our models. We observe a similar delay in eclogitization in the lower gabbroic crust (Figure 2.6). The gabbro is predicted to be a lawsonite-bearing glaucophane schist 350–680 km along transect. A dehydration reaction at 680 km across the transect yields a lawsonite and talc-bearing garnet eclogite. These predicted assemblages reflect water-saturated conditions, which we consider are limited to zones where rocks had previously undergone hydration reactions due to interaction with free water or water derived from greater depths due to expulsion by metamorphic reactions.

Within the hydrated portion of the subducting lithospheric mantle, water is held within chlorite and antigorite (Figure 2.7). The hydrous phases remain stable until approximately 720 km across the transect, where both are predicted to break down in a major dehydration reaction. From 350 to 720 km across the transect the rock is predicted to be an olivine diopside chlorite serpentinite. The dehydration reaction at ~720 km produces a garnet lherzolite (Figure 2.7).

We note that while this work is dependent on metamorphic equilibrium, there is recent evidence for reaction overstepping (i.e., Castro & Spear, 2017). It is possible that in subduction zones, considerably higher temperatures and pressures must be reached than are predicted in equilibrium for a metamorphic reaction to occur. While we currently cannot model disequilibrium processes, we acknowledge that any occurrence of disequilibrium could produce a delay in the reactions we have predicted in our calculations.

Hydration has a large effect on slab density. This is shown in Figure 2.8, which displays a comparison of predicted densities of an anhydrous subducting slab (magenta) with a moderately hydrated (green) or completely hydrated (in the crust and upper mantle only) slab (blue), and demonstrates the large effect that hydration has on slab density. The slab density calculations all include an anhydrous lower lithosphere 50 km thick (see "dry slab mantle" layer in Figure 2.3). The results displayed in green (Figure 2.8) reflect our hybrid model, with 1.5 wt% H_2O in the upper crust and 1 wt% H_2O in the lower crust and upper 10 km of the subducting mantle. Recall that our hybrid model reflects a simple mixture in specific proportions of the water-saturated and anhydrous models. The hybrid models produce a slab density reduction of 0.5%–0.8% compared with the anhydrous models. Note that full saturation (in blue) would produce a 2.3%–4.0% reduction in slab density; however, as we previously mentioned, we do not consider this to be realistic.

Our hybrid slab density calculations (green lines in Figure 2.8) yielded similar results to other scenarios we tested involving varying amounts of hydration in the crust and upper mantle (Figure A10). We tested a mod- el consisting of 3 wt% H_2O in the 20 km thick crust combined with a completely anhydrous mantle (Model 1 in Figure A10), as well as a model with 3 wt% H_2O in the upper 5 km of the crust and upper 5 km of the mantle (Model 3 in Figure A10). Both produced similar slab density results to our hybrid model (green lines in Figure 2.8 and Model 2 in Figure A10). Models using greater than 3 wt% H_2O reduce densities beyond those of our hybrid models, but this degree of hydration is unnecessary to sustain slab buoyancy. Additionally, we tested a model with hydration only in the upper 5 km of the crust (3 wt% H_2O), and no hydration in the lower crust or upper mantle (Model 4 in Figure A10). Results were similar to a completely anhydrous slab, as there was no significant decrease in slab density. We prefer our hybrid model (green lines in Figure 2.8) to our other tested models, as we believe there is sufficient evidence for upper mantle hydration in the Alaskan subducting slab (i.e., Feng & Ritzwoller, 2019; Martin-Short et al., 2018; Ward & Lin, 2018). Higher degrees of hydration are possible than were assumed in our hybrid model, and would result in greater slab buoyancy. The degree of hydration assumed for our hybrid model represents the approximate minimum needed to confidently produce buoyancy in the subducting slab.

Although slab rigidity could potentially prevent an anhydrous slab from assuming a steep angle of subduction close to the trench (per van Hunen et al., 2002), we find that hydration can reduce slab density sufficient to prevent the slab from sinking at a steep angle. We do not observe the subduction angle of the slab increasing until 400 km from the trench (550 km across transect). While other factors such as oceanic plateau rigidity (i.e., van Hunen et al., 2002) or slab suction (i.e., Stevenson & Turner, 1977; Tovish et al., 1978) could contribute to some delay in subduction angle steepening, hydration seems a sufficient mechanism for increasing slab buoyancy and maintaining low-angle subduction to 400 km from the subduction trench. We therefore prefer a partially hydrated slab over an anhydrous slab.

We note that we do not include a sediment layer in our slab density calculations or *Perple_X* modeling. We do not include it as it is theorized that much of the Yakutat sediments associated with the subducting oceanic plateau are either accreted (von Huene et al., 2012) or subcreted/underplated (i.e., Mankhemthong et al., 2013). Any metasedimentary layer remaining after the first 5 km of subduction would constitute a disproportionately small fraction of the total 20-km thick crust (Chuang et al., 2017), and an even smaller fraction of the entire 80-km thick slab. Thus, it is unlikely this would have a significant impact on our slab density calculations.

One implication of this work is that metamorphic dehydration reactions can provide a mechanism for the cessation of flat-slab subduction. If the angle of the subducting slab were to steepen due to metamorphic dehydration reactions causing densification, it could lead to a positive feedback cycle which would result in slab rollback. During rollback, hot asthenospheric mantle would well up in place of the subducting slab and interact with continental lithosphere that had become hydrated from rising fluids expelled from the subduction channel. This process would heat the overriding lithosphere, possibly leading to melting/volcanism, similar to Farallon slab rollback during the Laramide in western North America (Humphreys, 1995). Hydration of the overriding plate could also lower the viscosity of the continental mantle lithosphere and reduce the effects of slab-suction, which may further enable slab rollback (Kusky et al., 2014; Windley et al., 2010). The rate and geometry of slab rollback would control temperature conditions beneath the continental crust. This provides a potential mechanism for the cessation of low-angle subduction.

Our results have important implications for assessing slab buoyancy in other flat-slab subduction regions. Thermodynamic predictions of mineral stability provide the basis for determining the density of a subducting slab and the effect of hydration on density. Because metamorphic reactions are highly dependent on temperature, the numerical simulations of the thermal evolution are vital to understanding where they take place. It is also important to find ways of better constraining the water budget in subduction zones, as this has broad implications for slab buoyancy, arc volcanism, and volcanism during slab rollback.

2.9 CONCLUSION

The results of this study show that hydration of the oceanic lithosphere can play an important role in creating the conditions necessary for flat-slab subduction. Hydration decreases the density of a subducting slab, and increases its buoyancy relative to the underlying asthenosphere. Without hydration, the oceanic lithosphere in southern Alaska is predicted to become significantly more dense than the underlying asthenosphere at a distance of ~200 km from the trench, implying that steep subduction would be favored starting at this point if the oceanic lithosphere was completely anhydrous. However, we calculated that 1–1.5 wt% H_2O in the subducting crust and upper 10 km of the subducting mantle reduces slab density by 0.5%–0.8% and is sufficient to produce a buoyant slab that extends 300–400 km from the trench. The anomalously old (55 Ma) age of the Yakutat oceanic plateau makes for a cold slab entering the subduction system, and the crustal thickness (20 km) makes for a thick eclogite, thus creating a very dense slab after eclogitization conditions are reached.

Many of the current hypotheses for drivers of flat-slab subduction can be ruled out in the Alaskan flat-slab system. The slow absolute overriding plate motion in Alaska and age of the Yakutat oceanic plateau allow us to rule out the flat-slab subduction hypotheses that high overriding plate motion or young slab age influence low-angle subduction in Alaska. However, slab rigidity may be contributing to the resistance of the Yakutat oceanic plateau to assume a steep angle of subduction.

These models suggest that hydration is an important driver in initiating, sustaining, and ending flat-slab subduction in the southern Alaska system and globally. Predicting seismic velocities from our models in order to compare them with new seismic tomography studies could provide some insight into the degree and location of hydration in the Alaskan flat-slab system, as improved seismic imaging allows for some interpretation of composition. These future studies will also provide insight into locating where water is stored after the subducting crust and slab mantle dehydrates.

2.10 DATA AVAILABILITY STATEMENT

A data repository containing the data used in this study is available at https://zenodo.org/record/4670347#. YG3UmxNKgQ8 (https://doi.org/10.5281/zenodo.4670347).

2.11 ACKNOWLEDGMENTS

We are grateful for the insight and help from Jiangheng He and Kelin Wang at the Pacific Geoscience Centre in British Columbia in the use of *PGCTherm2D*. We are especially grateful for the comments from our reviewers Cailey Condit and David Hernandez-Uribe, whose suggestions and insights have greatly improved this manuscript. We also would like to thank three anonymous reviewers. This manuscript also benefited through conversations and comments from Paul Umhoefer and Cameron Petersen at Northern Arizona University. Additional thanks to Claire Currie at the University of Alberta for her help and insight. This work was funded by NSF Awards EAR-1645227 and EAR-1829520. The IRIS Data Management Center (https://ds.iris. edu/ds/nodes/dmc/) provided access to the seismic data used in this study. IRIS Data Services are funded through NSF Cooperative Agreement EAR-1261681 titled Seismological Facilities for the Advancement of Geoscience and EarthScope (SAGE).

2.12 REFERENCES

Abers, G. A. (1996). Plate structure and the origin of double seismic zones. Geophysical Monographs, 96, 223–228. https://doi.org/10.1029/ GM096p0223

Abers, G. A., van Keken, P. E., & Hacker, B. R. (2017). The cold and relatively dry nature of mantle forearcs in subduction zones. Nature Geoscience, 10, 333–337. https://doi.org/10.1038/ngeo2922

Abers, G. A., van Keken, P. E., Kneller, E. A., Ferris, A., & Stachnik, J. C. (2006). The thermal structure of subduction zones constrained by seismic imaging: Implications for slab dehydration and wedge flow. Earth and Planetary Science Letters, 241(3-4), 387–397. https:// doi.org/10.1016/j.epsl.2005.11.055

Antonijevic, S. K., Wagner, L. S., Kumar, A., Beck, S. L., Long, M. D., Zandt, G., et al. (2015). The role of ridges in the formation and longevity of flat slabs. Nature, 524(7564), 212–215. https://doi.org/10.1038/nature14648

Argus, D. F., Gordon, R. G., Heflin, M. B., Ma, C., Eanes, R. J., Willis, P., et al. (2010). The angular velocities of the plates and the velocity of Earth's centre from space geodesy. Geophysical Journal International, 180(3), 913–960. https://doi.org/10.1111/j.1365-246X.2009.04463.x

Auzanneau, E., Schmidt, M. W., Vielzeuf, D., & D Connolly, J. A. (2010). Titanium in phengite: a geobarometer for high temperature eclogites. Contributions to Mineralogy and Petrology, 159(1), 1–24. https://doi.org/10.1007/s00410-009-0412-7 Batchelor, G. K. (1967). An introduction to fluid dynamics. Cambridge University Press. p. 615. xviii.

Bauer, M. A., Pavlis, G. L., & Landes, M. (2014). Subduction geometry of the Yakutat terrane, southeastern Alaska. Geosphere, 10(6), 1161–1176. https://doi.org/10.1130/ges00852.1

Bebout, G. E. (1991). Field-based evidence for devolatilization in subduction zones: implications for arc magmatism. Science, 251(4992), 413–416. https://doi.org/10.1126/science.251.4992.413

Bebout, G. E. (2007). Metamorphic chemical geodynamics of subduction zones. Earth and Planetary Science Letters, 260(3-4), 373–393. Bebout, G. E., & Penniston-Dorland, S. C. (2016). Fluid and mass transfer at subduction interfaces-The field metamorphic record. Lithos, 240-243, 228–258. https://doi.org/10.1016/j.lithos.2015.10.007

Bruns, T. R. (1983). Model for the origin of the Yakutat block, an accreting terrane in the northern Gulf of Alaska. Geology, 11(12), 718–721. https://doi.org/10.1130/0091-7613(1983)11<718:mftoot>2.0.co;2

Cai, C., Wiens, D. A., Shen, W., & Eimer, M. (2018). Water input into the Mariana subduction zone estimated from ocean-bottom seismic data. Nature, 563, 389–392. https://doi.org/10.1038/s41586-018-0655-4

Castro, A. E., & Spear, F. S. (2017). Reaction overstepping and re-evaluation of peak P–T conditions of the blueschist unit Sifnos, Greece: implications for the Cyclades subduction zone. International Geology Review, 59(5-6), 548–562. https://doi.org/10.1080/00206814.201 6.1200499

Christeson, G. L., Gulick, S. P. S., van Avendonk, H. J. A., Worthington, L. L., Reece, R. S., & Pavlis, T. L. (2010). The Yakutat terrane: Dramatic change in crustal thickness across the Transition fault, Alaska. Geology, 38(10), 895–898. https://doi.org/10.1130/g31170.1

Chuang, L., Bostock, M., Wech, A., & Plourde, A. (2017). Plateau subduction, intraslab seismicity, and the Denali (Alaska) volcanic gap. Geology, 45(7), 647–650. https://doi.org/10.1130/g38867.1

Clouard, V., Campos, J., Lemoine, A., Perez, A., & Kausel, E. (2007). Outer rise stress changes related to the subduction of the Juan Fernandez Ridge, central Chile. Journal of Geophysical Research: Solid Earth, 112(B5). https://doi.org/10.1029/2005jb003999

Coggon, R., & Holland, T. J. B. (2002). Mixing properties of phengitic micas and revised garnet-phengite thermobarometers. Journal of Metamorphic Geology, 20(7), 683–696. https://doi.org/10.1046/j.1525-1314.2002.00395.x

Condit, C. B., Guevara, V. E., Delph, J. R., & French, M. E. (2020). Slab dehydration in warm subduction zones at depths of episodic slip and tremor. Earth and Planetary Science Letters, 552, 116601. https://doi.org/10.1016/j.epsl.2020.116601

Connolly, J. A. (2005). Computation of phase equilibria by linear programming: a tool for geodynamic modeling and its application to subduction zone decarbonation. Earth and Planetary Science Letters, 236(1-2), 524–541. https://doi.org/10.1016/j.epsl.2005.04.033

Cottrell, E., & Kelley, K. A. (2011). The oxidation state of Fe in MORB glasses and the oxygen fugacity of the upper mantle. Earth and Planetary Science Letters, 305(3-4), 270–282. https://doi.org/10.1016/j.epsl.2011.03.014

Cross, T. A., & Pilger, R. H. (1978). Constraints on absolute motion and plate interaction inferred from Cenozoic igneous activity in the western United States. American Journal of Science, 278(7), 865–902. https://doi.org/10.2475/ajs.278.7.865

Cross, T. A., & Pilger, Jr, R. H. (1982). Controls of subduction geometry, location of magmatic arcs, and tectonics of arc and back-arc regions. Geological Society of America Bulletin, 93(6), 545–562.

Currie, C. A., Wang, K., Hyndman, R. D., & He, J. (2004). The thermal effects of steady-state slab-driven mantle flow above a subducting plate: the Cascadia subduction zone and backarc. Earth and Planetary Science Letters, 223(1-2), 35–48. https://doi.org/10.1016/j.epsl.2004.04.020

Davis, A. S., & Plafker, G. (1986). Eocene basalts from the Yakutat terrane: Evidence for the origin of an accreting terrane in southern Alaska. Geology, 14(11), 963–966. https://doi.org/10.1130/0091-7613(1986)14<963:ebftyt>2.0.co;2

Dixon, J. E., Stolper, E., & Delaney, J. R. (1988). Infrared spectroscopic measurements of CO2 and H2O in Juan de Fuca Ridge basaltic glasses. Earth and Planetary Science Letters, 90(1), 87–104. https://doi.org/10.1016/0012-821x(88)90114-8

Eberhart-Phillips, D., Christensen, D. H., Brocher, T. M., Hansen, R., Ruppert, N. A., Haeussler, P. J., & Abers, G. A. (2006). Imaging the transition from Aleutian subduction to Yakutat collision in central Alaska, with local earthquakes and active source data. Journal of Geophysical Research: Solid Earth, 111(B11). https://doi.org/10.1029/2005JB004240

Elliott, J. L., Larsen, C. F., Freymueller, J. T., & Motyka, R. J. (2010). Tectonic block motion and glacial isostatic adjustment in southeast Alaska and adjacent Canada constrained by GPS measurements. Journal of Geophysical Research: Solid Earth, 115(B9). https://doi. org/10.1029/2009jb007139

Engebretson, D. C. (1985). Relative motions between oceanic and continental plates in the Pacific basin (Vol. 206). Geological Society of America.

English, J. M., Johnston, S. T., & Wang, K. (2003). Thermal modelling of the Laramide orogeny: testing the flat-slab subduction hypothesis.

Earth and Planetary Science Letters, 214(3-4), 619–632. https://doi.org/10.1016/s0012-821x(03)00399-6

Feng, L., & Ritzwoller, M. H. (2019). A 3-D shear velocity model of the crust and uppermost mantle beneath Alaska including apparent radial anisotropy. Journal of Geophysical Research: Solid Earth, 124(10), 10468–10497. https://doi.org/10.1029/2019jb018122

Finzel, E. S., Trop, J. M., Ridgway, K. D., & Enkelmann, E. (2011). Upper plate proxies for flat-slab subduction processes in southern Alaska.

Earth and Planetary Science Letters, 303(3-4), 348–360. https://doi.org/10.1016/j.epsl.2011.01.014

Fletcher, H. J., & Freymueller, J. T. (1999). New GPS constraints on the motion of the Yakutat block. Geophysical Research Letters, 26(19), 3029–3032. https://doi.org/10.1029/1999gl005346

Fromm, R., Alvarado, P., Beck, S. L., & Zandt, G. (2006). The April 9, 2001 Juan Fernández Ridge (M w 6.7) Tensional Outer-Rise Earth- quake and its Aftershock Sequence. Journal of Seismology, 10(2), 163–170. https://doi.org/10.1007/s10950-006-9013-3

Fuis, G. S., Moore, T. E., Plafker, G., Brocher, T. M., Fisher, M. A., Mooney, W. D., et al. (2008). Trans-Alaska Crustal Transect and continental evolution involving subduction underplating and synchronous foreland thrusting. Geology, 36(3), 267–270. https://doi.org/10.1130/ g24257a.1

Gale, A., Dalton, C. A., Langmuir, C. H., Su, Y., & Schilling, J.-G. (2013). The mean composition of ocean ridge basalts. Geochemistry, Geophysics, Geosystems, 14(3), 489–518. https://doi.org/10.1029/2012gc004334

Gardner, T. W., Fisher, D. M., Morell, K. D., & Cupper, M. L. (2013). Upper-plate deformation in response to flat slab subduction inboard of the aseismic Cocos Ridge, Osa Peninsula, Costa Rica. Lithosphere, 5(3), 247–264. https://doi.org/10.1130/L251.1

Garth, T., & Rietbrock, A. (2017). Constraining the hydration of the subducting Nazca plate beneath Northern Chile using subduction zone guided waves. Earth and Planetary Science Letters, 474, 237–247. https://doi.org/10.1016/j.epsl.2017.06.041

Gerya, T. (2011). Future directions in subduction modeling. Journal of Geodynamics, 52(5), 344–378. https://doi.org/10.1016/j. jog.2011.06.005

Gutscher, M.-A. (2002). Andean subduction styles and their effect on thermal structure and interplate coupling. Journal of South American Earth Sciences, 15(1), 3–10. https://doi.org/10.1016/S0895-9811(02)00002-0

Gutscher, M.-A., Klingelhoefer, F., Theunissen, T., Spakman, W., Berthet, T., Wang, T. K., & Lee, C.-S. (2016). Thermal modeling of the SW Ryukyu forearc (Taiwan): Implications for the seismogenic zone and the age of the subducting Philippine Sea Plate (Huatung Basin). Tectonophysics, 692, 131–142. https://doi.org/10.1016/j.tecto.2016.03.029

Gutscher, M.-A., Maury, R., Eissen, J.-P., & Bourdon, E. (2000). Can slab melting be caused by flat subduction? Geology, 28(6), 535. https:// doi.org/10.1130/0091-7613(2000)28<53510.1130/0091-7613(2000)28<535:csmbcb>2.0.co;2

Gutscher, M. A., & Peacock, S. M. (2003). Thermal models of flat subduction and the rupture zone of great subduction earthquakes. Jour- nal of Geophysical Research: Solid Earth, 108(B1). ESE-2. https://doi.org/10.1029/2001jb000787

Hacker, B. R. (1996). Eclogite formation and the rheology, buoyancy, seismicity, and H2O content of oceanic crust. Geophysical Mono- graph-American Geophysical Union, 96, 337–346.

Hacker, B. R. (2008). H2O subduction beyond arcs. Geochemistry, Geophysics, Geosystems, 9(3). https://doi.org/10.1029/2007gc001707

Hacker, B. R., & Abers, G. A. (2004). Subduction Factory 3: An Excel worksheet and macro for calculating the densities, seismic wave speeds, and H2O contents of minerals and rocks at pressure and temperature. Geochemistry, Geophysics, Geosystems, 5(1).

Hacker, B. R., Peacock, S. M., Abers, G. A., & Holloway, S. D. (2003). Subduction factory 2. Are intermediate-depth earthquakes in subducting slabs linked to metamorphic dehydration reactions? Journal of Geophysical Research: Solid Earth, 108(B1).

Hartlieb, P., Toifl, M., Kuchar, F., Meisels, R., & Antretter, T. (2016). Thermo-physical properties of selected hard rocks and their relation to microwave-assisted comminution. Minerals Engineering, 91, 34–41.

Hasterok, D., & Chapman, D. S. (2011). Heat production and geotherms for the continental lithosphere. Earth and Planetary Science Letters, 307(1-2), 59–70. https://doi.org/10.1016/j.epsl.2011.04.034

Hasterok, D., & Webb, J. (2017). On the radiogenic heat production of igneous rocks. Geoscience Frontiers, 8(5), 919–940. https://doi. org/10.1016/j.gsf.2017.03.006

Hernández-Uribe, D., & Palin, R. M. (2019a). Catastrophic shear-removal of subcontinental lithospheric mantle beneath the Colorado Plateau by the subducted Farallon slab. Scientific Reports, 9(1), 1–10. https://doi.org/10.1038/s41598-019-44628-y

Hernández-Uribe, D., & Palin, R. M. (2019b). A revised petrological model for subducted oceanic crust: Insights from phase equilibrium modelling. Journal of Metamorphic Geology, 37(6), 745–768.

Hoisch, T. D. (2005). Thermod7: A general two-dimensional numerical modeling program for heat conduction and advection, with special application to faults. Computers & Geosciences, 31(6), 698–703. https://doi.org/10.1016/j.cageo.2005.01.005

Holland, T., Baker, J., & Powell, R. (1998b). Mixing properties and activity-composition relationships of chlorites in the system MgO-FeO-Al2O3-SiO2-H2O. European Journal of Mineralogy, 10, 395–406. https://doi.org/10.1127/ejm/10/3/0395

Holland, T. J. B., & Powell, R. (1998a). An internally consistent thermodynamic data set for phases of petrological interest. Journal of Metamorphic Geology, 16(3), 309–343.

Holland, T. J. B., & Powell, R. (2011). An improved and extended internally consistent thermodynamic dataset for phases of petrological interest, involving a new equation of state for solids. Journal of Metamorphic Geology, 29(3), 333–383. https://doi. org/10.1111/j.1525-1314.2010.00923.x

Holland, T., & Powell, R. (1996). Thermodynamics of order-disorder in minerals; II, Symmetric formalism applied to solid solutions. American Mineralogist, 81(11-12), 1425–1437. https://doi.org/10.2138/am-1996-11-1215

Holland, T., & Powell, R. (2003). Activity-composition relations for phases in petrological calculations: an asymmetric multicomponent formulation. Contributions to Mineralogy and Petrology, 145(4), 492–501. https://doi.org/10.1007/s00410-003-0464-z

Humphreys, E. D. (1995). Post-Laramide removal of the Farallon slab, western United States. Geology, 23(11), 987–990. https://doi.org/10.1130/0091-7613(1995)023<0987:plrotf>2.3.co;2

Hyndman, R. D., & Peacock, S. M. (2003). Serpentinization of the forearc mantle. Earth and Planetary Science Letters, 212(3-4), 417–432. https://doi.org/10.1016/s0012-821x(03)00263-2

Irifune, T., & Ringwood, A. E. (1993). Phase transformations in subducted oceanic crust and buoyancy relationships at depths of 600–800 km in the mantle. Earth and Planetary Science Letters, 117(1-2), 101–110. https://doi.org/10.1016/0012-821x(93)90120-x

Ito, E., Harris, D. M., & Anderson, A. T., Jr (1983). Alteration of oceanic crust and geologic cycling of chlorine and water. Geochimica et Cosmochimica Acta, 47(9), 1613–1624. https://doi.org/10.1016/0016-7037(83)90188-6

Jaeckel, K., Bebout, G. E., & Angiboust, S. (2018). Deformation-enhanced fluid and mass transfer along Western and Central Alps paleo-subduction interfaces: Significance for carbon cycling models. Geosphere, 14(6), 2355–2375. https://doi.org/10.1130/GES01587.1

Jischke, M. C. (1975). On the dynamics of descending lithospheric plates and slip zones. Journal of Geophysical Research, 80(35), 4809–4813. https://doi.org/10.1029/JB080i035p04809

Kelemen, P. B., Kikawa, E., & Miller, D. J. (2004). Proc. ODP, Init. Repts. (Vol. 209). College Station, TX: Ocean Drilling Program. https:// doi.org/10.2973/odp.proc.ir.209.2004

Kirby, S., Engdahl, R. E., & Denlinger, R. (1996). Intermediate-depth intraslab earthquakes and arc volcanism as physical expressions of crustal and uppermost mantle metamorphism in subducting slabs. Subduction: Top to Bottom, 96, 195–214.

Kohn, M. J., Castro, A. E., Kerswell, B. C., Ranero, C. R., & Spear, F. S. (2018). Shear heating reconciles thermal models with the metamorphic rock record of subduction. Proceedings of the National Academy of Sciences, 115(46), 11706–11711.

Kopp, H., Flueh, E. R., Papenberg, C., & Klaeschen, D. (2004). Seismic investigations of the O'Higgins Seamount Group and Juan Fernández Ridge: Aseismic ridge emplacement and lithosphere hydration. Tectonics, 23(2). https://doi.org/10.1029/2003tc001590

Kumar, P., & Kawakatsu, H. (2011). Imaging the seismic lithosphere-asthenosphere boundary of the oceanic plate. Geochemistry, Geophysics, Geosystems, 12(1). https://doi.org/10.1029/2010gc003358

Kusky, T. M., Windley, B. F., Wang, L., Wang, Z., Li, X., & Zhu, P. (2014). Flat slab subduction, trench suction, and craton destruction: comparison of the North China, Wyoming, and Brazilian cratons. Tectonophysics, 630, 208–221. https://doi.org/10.1016/j.tecto.2014.05.028

Lefeldt, M., Ranero, C. R., & Grevemeyer, I. (2012). Seismic evidence of tectonic control on the depth of water influx into incoming oceanic plates at subduction trenches. Geochemistry, Geophysics, Geosystems, 13(5).

LeVeque, R. J. (1996). High-resolution conservative algorithms for advection in incompressible flow. SIAM Journal on Numerical Analysis, 33(2), 627–665. https://doi.org/10.1137/0733033

Ma, Y., & Clayton, R. W. (2015). Flat slab deformation caused by interplate suction force. Geophysical Research Letters, 42, 1–9. https://doi. org/10.1002/(ISSN)1944-800710.1002/2015gl065195

Manea, V. C., Pérez-Gussinyé, M., & Manea, M. (2012). Chilean flat slab subduction controlled by overriding plate thickness and trench rollback. Geology, 40(1), 35–38. https://doi.org/10.1130/G32543.1

Mankhemthong, N., Doser, D. I., & Pavlis, T. L. (2013). Interpretation of gravity and magnetic data and development of two-dimensional cross-sectional models for the Border Ranges fault system, south-central Alaska. Geosphere, 9(2), 242–259. https://doi.org/10.1130/ ges00833.1

Martin-Short, R., Allen, R., Bastow, I. D., Porritt, R. W., & Miller, M. S. (2018). Seismic imaging of the Alaska subduction zone: Implications for slab geometry and volcanism. Geochemistry, Geophysics, Geosystems, 19(11), 4541–4560.

Martin-Short, R., Allen, R. M., & Bastow, I. D. (2016). Subduction geometry beneath south central Alaska and its relationship to volcanism. Geophysical Research Letters, 43(18), 9509–9517.

Moore, J. C., & Saffer, D. (2001). Updip limit of the seismogenic zone beneath the accretionary prism of southwest Japan: An effect of diagenetic to low-grade metamorphic processes and increasing effective stress. Geology, 29(2), 183–186. https://doi.org/10.1130/0091-7 613(2001)029<0183:ulotsz>2.0.co;2

Mostafa, M. S., Afify, N., Gaber, A., & Zaid, E. A. (2004). Investigation of thermal properties of some basalt samples in Egypt. Journal of Thermal Analysis and Calorimetry, 75(1), 179–188.

Naif, S., Key, K., Constable, S., & Evans, R. L. (2015). Water-rich bending faults at the Middle America Trench. Geochemistry, Geophysics, Geosystems, 16(8), 2582–2597. https://doi.org/10.1002/2015gc005927

Newton, R. C., Charlu, T. V., & Kleppa, O. J. (1980). Thermochemistry of the high structural state plagioclases. Geochimica et Cosmochimica Acta, 44(7), 933–941. https://doi.org/10.1016/0016-7037(80)90283-5

Niu, Y., Gilmore, T., Mackie, S., Greig, A., & Bach, W. (2002). Mineral chemistry, whole-rock compositions, and petrogenesis of Leg 176 gabbros: data and discussion. In J. H. Natland, H. J. B. Dick, D. J. Miller, & R. P. Von Herzen (Eds.), Proc. ODP, Sci. Results (Vol. 176, pp. 1–60). College Station, TX: Ocean Drilling Program.

Nye, C. (1999). The Denali volcanic gap—Magmatism at the eastern end of the Aleutian arc. Eos Transactions American Geophysical Union, 80, 46.

O'Driscoll, L. J., Humphreys, E. D., & Saucier, F. (2009). Subduction adjacent to deep continental roots: Enhanced negative pressure in the mantle wedge, mountain building and continental motion. Earth and Planetary Science Letters, 280(1-4), 61–70. https://doi. org/10.1016/j.epsl.2009.01.020

O'Driscoll, L. J., & Miller, M. S. (2015). Lithospheric discontinuity structure in Alaska, thickness variations determined bySpreceiver func- tions. Tectonics, 34(4), 694–714. https://doi.org/10.1002/2014tc003669

Olbertz, D., Wortel, M. J. R., & Hansen, U. (1997). Trench migration and subduction zone geometry. Geophysical Research Letters, 24(3), 221–224. https://doi.org/10.1029/96gl03971

Padrón-Navarta, J. A., Sánchez-Vizcaíno, V. L., Hermann, J., Connolly, J. A. D., Garrido, C. J., Gómez-Pugnaire, M. T., & Marchesi, C. (2013). Tschermak's substitution in antigorite and consequences for phase relations and water liberation in high-grade serpentinites. Lithos, 178, 186–196. https://doi.org/10.1016/j.lithos.2013.02.001

Park, J., & Rye, D. M. (2019). Broader impacts of the metasomatic underplating hypothesis. Geochemistry, Geophysics, Geosystems, 20(11), 4810–4829.

Peacock, S. A. (1990). Fluid processes in subduction zones. Science, 248(4953), 329–337. https://doi.org/10.1126/science.248.4953.329 Peacock, S. M. (1993a). Large-scale hydration of the lithosphere above subducting slabs. Chemical Geology, 108(1-4), 49–59. https://doi.org/10.1016/0009-2541(93)90317-c

Peacock, S. M. (1993b). The importance of blueschist → eclogite dehydration reactions in subducting oceanic crust. Geological Society of America Bulletin, 105(5), 684–694. https://doi.org/10.1130/0016-7606(1993)105<0684:tiobed>2.3.co;2

Peacock, S. M. (2001). Are the lower planes of double seismic zones caused by serpentine dehydration in subducting oceanic mantle? Geology, 29(4), 299–302. https://doi.org/10.1130/00917613(2001)029<0299:atlpod>2.0.co;2

Peacock, S. M. (2009). Thermal and metamorphic environment of subduction zone episodic tremor and slip. Journal of Geophysical Re- search: Solid Earth, 114(B8). https://doi.org/10.1029/2008jb005978

Peacock, S. M., & Wang, K. (1999). Seismic consequences of warm versus cool subduction metamorphism: Examples from southwest and northeast Japan. Science, 286(5441), 937–939. https://doi.org/10.1126/science.286.5441.937

Penniston-Dorland, S. C., Kohn, M. J., & Manning, C. E. (2015). The global range of subduction zone thermal structures from exhumed blueschists and eclogites: Rocks are hotter than models. Earth and Planetary Science Letters, 428, 243–254.

Pilger, R. H., Jr (1981). Plate reconstructions, aseismic ridges, and low-angle subduction beneath the Andes. The Geological Society of America Bulletin, 92(7), 448. https://doi.org/10.1130/0016-7606(1981)92<448:PRARAL>2.0.CO;2.10.1130/0016-7606(1981)92<448:praral>2.0.co;2

Plafker, G., & Berg, H. C. (1994). Overview of the geology and tectonic evolution of Alaska. In Plafker, G. & Bergs, H.C. (Eds.), The Geology of North America, The Geology of Alaska (Vol. G-1, pp. 989–1021). Boulder, CO, Geological Society of America.

Plafker, G., Hudson, T., Bruns, T., & Rubin, M. (1978). Late Quaternary offsets along the Fairweather fault and crustal plate interactions in southern Alaska. Canadian Journal of Earth Sciences, 15(5), 805–816. https://doi.org/10.1139/e78-085

Plattner, C., Malservisi, R., Dixon, T. H., LaFemina, P., Sella, G. F., Fletcher, J., & Suarez-Vidal, F. (2007). New constraints on relative motion between the Pacific plate and Baja California microplate (Mexico) from GPS measurements. Geophysical Journal International, 170(3), 1373–1380. https://doi.org/10.1111/j.1365-246x.2007.03494.x

Porter, R., Gilbert, H., Zandt, G., Beck, S., Warren, L., Calkins, J., et al. (2012). Shear wave velocities in the Pampean flat-slab region from Rayleigh wave tomography: Implications for slab and upper mantle hydration. Journal of Geophysical Research, 117(B11), B11301. https://doi.org/10.1029/2012JB009350

Powell, R., & Holland, T. (1999). Relating formulations of the thermodynamics of mineral solid solutions; activity modeling of pyroxenes, amphiboles, and micas. American Mineralogist, 84(1-2), 1–14. https://doi.org/10.2138/am-1999-1-201

Prigent, C., Warren, J. M., Kohli, A. H., & Teyssier, C. (2020). Fracture-mediated deep seawater flow and mantle hydration on oceanic transform faults. Earth and Planetary Science Letters, 532, 115988. https://doi.org/10.1016/j.epsl.2019.115988

Rüpke, L., Morgan, J. P., Hort, M., & Connolly, J. A. (2004). Serpentine and the subduction zone water cycle. Earth and Planetary Science Letters, 223(1), 17–34. https://doi.org/10.1016/j.epsl.2004.04.018

Ramos, V. A., & Folguera, A. (2009). Andean flat-slab subduction through time. Geological Society, London, Special Publications, 327, 31–54. https://doi.org/10.1144/SP327.310.1144/sp327.3

Ranero, C. R., Morgan, J. P., McIntosh, K., & Reichert, C. (2003). Bending-related faulting and mantle serpentinization at the Middle America trench. Nature, 425(6956), 367–373.

Rioux, M., Mattinson, J., Hacker, B., Kelemen, P., Blusztajn, J., Hanghøj, K., & Gehrels, G. (2010). Intermediate to felsic middle crust in the accreted Talkeetna arc, the Alaska Peninsula and Kodiak Island, Alaska: An analogue for low-velocity middle crust in modern arcs. Tectonics, 29(3). https://doi.org/10.1029/2009tc002541

Roe, P. L. (1985). Some contributions to the modelling of discontinuous flows. In Engquist, B.E., Osher, S., & Somerville, R.C.J. (Eds.), Large-scale computations in fluid mechanics, Lectures in Applied Mathematics (Vol. 22, pp. 163–193). Providence, RI, American Mathematical Society.

Rondenay, S., Montési, L. G. J., & Abers, G. A. (2010). New geophysical insight into the origin of the Denali volcanic gap. Geophysical Journal International, 182(2), 613–630. https://doi.org/10.1111/j.1365-246x.2010.04659.x

Rossi, G., Abers, G. A., Rondenay, S., & Christensen, D. H. (2006). Unusual mantle Poisson's ratio, subduction, and crustal structure in central Alaska. Journal of Geophysical Research: Solid Earth, 111(B9). https://doi.org/10.1029/2005jb003956

Rudnick, R. L., & Gao, S. (2003). Composition of the continental crust. Treatise on Geochemistry, 3, 659.

Saffer, D. M., & Bekins, B. A. (1998). Episodic fluid flow in the Nankai accretionary complex: Timescale, geochemistry, flow rates, and fluid budget. Journal of Geophysical Research, 103(B12), 30351–30370. https://doi.org/10.1029/98jb01983

Saffer, D. M., & Tobin, H. J. (2011). Hydrogeology and mechanics of subduction zone forearcs: Fluid flow and pore pressure. Annual Review of Earth and Planetary Sciences, 39, 157–186. https://doi.org/10.1146/annurev-earth-040610-133408

Seno, T., & Gonzalez, D. G. (1987). Faulting caused by earthquakes beneath the outer slope of the Japan Trench. Journal of Physics of the Earth, 35(5), 381–407.

Seno, T., & Yamanaka, Y. (1996). Double seismic zones, compressional deep trench-outer rise events, and superplumes. Subduction: Top to Bottom, 96, 347–355.

Skinner, S. M., & Clayton, R. W. (2010). An evaluation of proposed mechanisms of slab flattening in Central Mexico. Pure and Applied Geophysics, 168, 1461–1474. https://doi.org/10.1007/s00024-010-0200-3

Stein, C. A., & Stein, S. (1992). A model for the global variation in oceanic depth and heat flow with lithospheric age. Nature, 359(6391), 123–129. https://doi.org/10.1038/359123a0

Stern, R. J. (2002). Subduction zones. Reviews of Geophysics, 40(4), 3-1.

Stevenson, D. J., & Turner, J. S. (1977). Angle of subduction. Nature, 270, 334–336. https://doi.org/10.1038/270334a0

Tovish, A., Schubert, G., & Luyendyk, B. P. (1978). Mantle flow pressure and the angle of subduction: Non-Newtonian corner flows. Jour- nal of Geophysical Research, 83(B12), 5892–5898. https://doi.org/10.1029/jb083ib12p05892

Turcotte, D. L. & Schubert, G. (1982). Geodynamics. Wiley, p. 435.

Ulmer, P., & Trommsdorff, V. (1995). Serpentine stability to mantle depths and subduction-related magmatism. Science, 268(5212), 858– 861. https://doi.org/10.1126/science.268.5212.858

Usui, T., Nakamura, E., Kobayashi, K., Maruyama, S., & Helmstaedt, H. (2003). Fate of the subducted Farallon plate inferred from eclogite xenoliths in the Colorado Plateau. Geology, 31(7), 589–592. https://doi.org/10.1130/0091-7613(2003)031<0589:fotsfp>2.0.co;2

van Hunen, J., van den Berg, A. P., & Vlaar, N. J. (2000). A thermo-mechanical model of horizontal subduction below an overriding plate. Earth and Planetary Science Letters, 182(2), 157–169. https://doi.org/10.1016/s0012-821x(00)00240-5

van Hunen, J., van den Berg, A. P., & Vlaar, N. J. (2002). On the role of subducting oceanic plateaus in the development of shallow flat subduction. Tectonophysics, 352(3-4), 317–333. https://doi.org/10.1016/s0040-1951(02)00263-9

van Keken, P. E., Currie, C., King, S. D., Behn, M. D., Cagnioncle, A., He, J., et al. (2008). A community benchmark for subduction zone modeling. Physics of the Earth and Planetary Interiors, 171(1-4), 187–197. https://doi.org/10.1016/j.pepi.2008.04.015

van Keken, P. E., Hacker, B. R., Syracuse, E. M., & Abers, G. A. (2011). Subduction factory: 4. Depth-dependent flux of H2O from subducting slabs worldwide. Journal of Geophysical Research: Solid Earth, 116(B1). https://doi.org/10.1029/2010jb007922

van Keken, P. E., Kiefer, B., & Peacock, S. M. (2002). High-resolution models of subduction zones: Implications for miner- al dehydration reactions and the transport of water into the deep mantle. Geochemistry, Geophysics, Geosystems, 3(10), 20. https://doi.org/10.1029/2001GC000256

van Keken, P. E., Wada, I., Abers, G. A., Hacker, B. R., & Wang, K. (2018). Mafic high-pressure rocks are preferentially exhumed from warm subduction settings. Geochemistry, Geophysics, Geosystems, 19(9), 2934–2961. https://doi.org/10.1029/2018gc007624

Veenstra, E., Christensen, D. H., Abers, G. A., & Ferris, A. (2006). Crustal thickness variation in south-central Alaska. Geology, 34(9), 781–784. https://doi.org/10.1130/g22615.1

Vlaar, N. J. (1983). Thermal anomalies and magmatism due to lithospheric doubling and shifting. Earth and Planetary Science Letters, 65(2), 322–330. https://doi.org/10.1016/0012-821x(83)90170-x

von Huene, R., Miller, J. J., & Weinrebe, W. (2012). Subducting plate geology in three great earthquake ruptures of the western Alaska margin, Kodiak to Unimak. Geosphere, 8(3), 628–644. https://doi.org/10.1130/ges00715.1

Wada, I., & Wang, K. (2009). Common depth of slab-mantle decoupling: Reconciling diversity and uniformity of subduction zones. Geo- chemistry, Geophysics, Geosystems, 10(10). https://doi.org/10.1029/2009gc002570

Wada, I., Wang, K., He, J., & Hyndman, R. D. (2008). Weakening of the subduction interface and its effects on surface heat flow, slab dehydration, and mantle wedge serpentinization. Journal of Geophysical Research: Solid Earth, 113(B4). https://doi.org/10.1029/2007jb005190

Waldbaum, D. R, & Thompson, J. B (1968). Mixing properties of sanidine crystalline solutions: 2. Calculations based on volume data. American Mineralogist, 53, 2000–2017

Wang, Y., & Tape, C. (2014). Seismic velocity structure and anisotropy of the Alaska subduction zone based on surface wave tomography. Journal of Geophysical Research: Solid Earth, 119(12), 8845–8865. https://doi.org/10.1002/2014jb011438

Waples, D. W., & Waples, J. S. (2004). A review and evaluation of specific heat capacities of rocks, minerals, and subsurface fluids. Part 2: fluids and porous rocks. Natural Resources Research, 13(2), 123–130.

Ward, K. M. (2015). Ambient noise tomography across the southern Alaskan Cordillera. Geophysical Research Letters, 42(9), 3218–3227.

Ward, K. M., & Lin, F. C. (2018). Lithospheric structure across the Alaskan cordillera from the joint inversion of surface waves and receiver functions. Journal of Geophysical Research: Solid Earth, 123, 8780–8797. https://doi.org/10.1029/2018JB015967

Wei, C., & Powell, R. (2003). Phase relations in high-pressure metapelites in the system KFMASH (K2O–FeO–MgO–Al2O3–SiO2–H2O) with application to natural rocks. Contributions to Mineralogy and Petrology, 145(3), 301–315. https://doi.org/10.1007/s00410-003-0454-1

Wells, R., Bukry, D., Friedman, R., Pyle, D., Duncan, R., Haeussler, P., & Wooden, J. (2014). Geologic history of Siletzia, a large igneous province in the Oregon and Washington Coast Range: Correlation to the geomagnetic polarity time scale and implications for a long- lived Yellowstone hotspot. Geosphere, 10(4), 692–719. https://doi.org/10.1130/ges01018.1

White, R. W., Powell, R., Holland, T. J. B., & Worley, B. A. (2000). The effect of TiO2 and Fe2O3 on metapelitic assemblages at greenschist and amphibolite facies conditions: mineral equilibria calculations in the system K2O-FeO-MgO-Al2O3-SiO2-H2O-TiO2-Fe2O3. Journal of Metamorphic Geology, 18, 497–511. https://doi.org/10.1046/j.1525-1314.2000.00269.x

White, R. W., Powell, R., & Johnson, T. E. (2014). The effect of Mn on mineral stability in metapelites revisited: new a -x relations for manganese-bearing minerals. Journal of Metamorphic Geology, 32(8), 809–828. https://doi.org/10.1111/jmg.12095

White, R. W., Powell, R., & Phillips, G. N. (2003). A mineral equilibria study of the hydrothermal alteration in mafic greenschist facies rocks at Kalgoorlie, Western

Australia. Journal of Metamorphic Geology, 21(5), 455–468. https://doi.org/10.1046/j.1525-1314.2003.00454.x

Windley, B. F., Maruyama, S., & Xiao, W. J. (2010). Delamination/thinning of sub-continental lithospheric mantle under Eastern China: the role of water and multiple subduction. American Journal of Science, 310(10), 1250–1293. https://doi.org/10.2475/10.2010.03

Woodland, A. B., Kornprobst, J., & Tabit, A. (2006). Ferric iron in orogenic lherzolite massifs and controls of oxygen fugacity in the upper mantle. Lithos, 89(1-2), 222–241. https://doi.org/10.1016/j.lithos.2005.12.014

Workman, R. K., & Hart, S. R. (2005). Major and trace element composition of the depleted MORB mantle (DMM). Earth and Planetary Science Letters, 231(1-2), 53–72. https://doi.org/10.1016/j.epsl.2004.12.005

Worthington, L. L., Van Avendonk, H. J., Gulick, S. P., Christeson, G. L., & Pavlis, T. L. (2012). Crustal structure of the Yakutat terrane and the evolution of subduction and collision in southern Alaska. Journal of Geophysical Research: Solid Earth, 117(B1). https://doi. org/10.1029/2011jb008493

Wunder, B., & Schreyer, W. (1997). Antigorite: High-pressure stability in the system MgO SiO2 H2O (MSH). Lithos, 41(1-3), 213–227. https://doi.org/10.1016/s0024-4937(97)82013-0

Yáñez, G., Cembrano, J., Pardo, M., Ranero, C., & Selles, D. (2002). The Challenger-Juan Fernández-Maipo major tectonic transition of the Nazca-Andean subduction system at 33–34°S: geodynamic evidence and implications. Journal of South American Earth Sciences, 15(1), 23–38. https://doi.org/10.1016/s0895-9811(02)00004-4

Zheng, Y., Chen, R., Xu, Z., & Zhang, S. (2016). The transport of water in subduction zones. Science China Earth Sciences, 59(4), 651–682. https://doi.org/10.1007/s11430-015-5258-4

CHAPTER 3: SEISMIC AND MODELING EVIDENCE FOR HYDRATION OF THE ALASKAN FLAT-SLAB SUBDUCTION REGION

Authors: Petersen, S.E., Porter, R.C.

3.1 ABSTRACT

Water plays an important role in subduction zone processes, and it is increasingly evident that the presence of mineral-bound H_2O in subducting slabs impacts the behavior of low-angle subduction systems. Using the Abers and Hacker (2016) toolbox, thermal modeling, and mineral phase equilibria results, we predict P and S wave velocities within the Alaskan flat-slab subduction zone and compare these to published seismic velocity models. This allows us to test hydration models for southern Alaska. Results are consistent with the subducting slab containing at least 3 wt% water held in the 20-km thick crust and upper 10 km of the subducting mantle. This hydration likely impacts the buoyancy and rheology of the subducting slab and overriding plate.

3.2 INTRODUCTION

Flat-slab subduction (FSS) occurs in convergent margins where the downgoing oceanic plate assumes a shallow or horizontal angle beneath the overriding plate. This form of subduction occurs in ~10% of subduction zones worldwide by length (Gutscher et al., 2000). Several hypotheses have been debated as to the cause of FSS, including fast convergence rates, young (warmer) oceanic slabs, the subduction of thicker crust (i.e. buoyant aseismic ridges), slab suction, and the incorporation of water into subducting slabs (Jischke, 1975; Stevenson and Turner, 1977; Pilger, 1981; Gutscher, 2002; O'Driscoll et al., 2009; Ramos and Folguera, 2009; Skinner and Clayton, 2010; Manea et al., 2011; Porter et al., 2012; Gardner et al., 2013; Knezevic Antonijevic et al., 2015; Ma and Clayton, 2015; Petersen et al., 2021). In this work, we combine seismic data with several modeling approaches to better understand the hydration state of low-angle subduction in Alaska and its impact on regional subduction.

Water is an important component in all subduction systems regardless of subduction geometry due to its impacts on subduction behavior including volcanism, mineralogy, and overall rheology of the system (i.e. Peacock, 1990; Rupke et al., 2004; van Keken et al., 2002; van Keken et al., 2011). In some hot and steep subduction systems, dehydration reactions in the downgoing oceanic slab occur within the first ten kilometers from the trench as it sinks into the underlying asthenosphere due to increases in pressure and temperature (van Keken et al., 2011). As the slab subducts deeper, convection in the asthenospheric wedge continues to warm the downgoing oceanic plate, driving further dehydration reactions and leading to the release of additional volatiles. These volatiles typically lead to mantle melting and volcanic arc formation. In FSS systems, the shallow angle of subduction keeps the downgoing lithosphere at relatively low pressures further inboard of the trench and cuts off corner flow, resulting in a much cooler thermal system (English et al., 2003; van Hunen et al., 2000; van Hunen et al., 2002; Petersen et al., 2021). These cooler conditions delay dehydration reactions within the subducting slab and, as a result, inhibit volcanism. Volcanism is commonly absent in these systems until slab break-off or rollback allows for the upwelling hot asthenosphere to interact with any present volatiles (Humphreys, 1995; Petersen et al., 2021). Since the shallow slab dehydrates further from the trench, less dense hydrous minerals remain stable well inboard from the plate margin than in typical-angle subduction. Because hydrous phases are generally less dense than anhydrous phases, this is a potential mechanism for maintaining positive slab buoyancy, which may contribute to its shallow subduction angle.

A recent study (Petersen et al., 2021) demonstrated that, in Alaska, a dry subducting oceanic plateau in the FSS region would not be buoyant enough to maintain its current shallow subduction angle without invoking dynamic mechanisms for low-angle subduction. However, it is difficult however to quantify the amount of water contained in the subducting slab, or to determine where water may be concentrated in the subduction system. It has been suggested that subducting aseismic ridges (such as the Yakutat Plateau in Alaska) could be holding more water in their composition than typical oceanic crust, possibly due to an increased amount of hydrothermal circulation during their formation and fracturing due to melt intrusions (Park and Rye, 2019), or possibly due to outer rise bending and faulting allowing for water infiltration along deep cracks (Peacock, 2001; Yáñez et al., 2002; Ranero et al., 2003; Lefeldt et al., 2012; Porter et al., 2012; Zheng et al., 2016).

Seismic velocities are sensitive to temperature (T), pressure (P), composition (X), hydration state, and the presence or absence of melt. The non-uniqueness of seismic data makes isolating any one of these factors challenging using only seismic observations. To overcome this, we combine thermal and phase-equilibria modelling to constrain P-T-X states in order to better isolate the effects of hydration. Seismic wave speeds are usually reduced when traveling through hydrated mineral assemblages due to anelastic relaxation (Karato and Jung, 1998). However, high temperatures can also reduce seismic velocities due to anharmonic and anelastic effects (Gueguen and Mercier, 1973; Minster and Anderson, 1981) as can the presence of partial melt (Hammond and Humphreys, 2000). The effect of melt on seismic velocities is widely debated (Anderson and Sammis, 1970; Karato and Jung, 1998; van der Lee, 2002; Dunn and Forsyth, 2003; Schutt and Dueker, 2008; Porter et al., 2019). Thermal modeling shows that the relatively cold temperatures of FSS systems like Alaska's make it unlikely that melt is present. Therefore, the primary controllers of seismic velocity in Alaska's FSS zone are temperature, pressure, composition, and/or hydration. By using alternate methods to constrain pressure, temperature, and composition, hydration can be better constrained with seismic data.

The seismic velocities of earth material are typically measured using one of two techniques. The velocities of whole rock samples can be measured within a lab setting (Carlson, 2014). Alternatively, elastic data for individual minerals can be averaged to predict seismic velocities for an arbitrary rock composition if mineral abundances are known and the constituent mineral elastic properties can be adequately described (Bina and Helffrich, 1992).

In this study, we attempt to better understand upper mantle hydration in the Alaskan flat-slab region by comparing predictions of seismic velocity at varying hydration states to published seismic velocity models. To accomplish this, we use thermal and phase equilibria modeling to constrain temperature and pressure. We then combine these results with estimates of rock chemical composition to calculate stable mineral assemblages and, subsequently, use these to predict seismic velocities for the Alaskan flat slab region at varying degrees of hydration. The recent deployment of dense seismic instrumentation as part of EarthScope's Transportable Array (TA) in Alaska has made it possible to image the flat-slab region of Alaska in higher resolution than was previously possible. This study tests the hypothesis that the presence of hydration in the subducting slab is a contributing factor to Alaskan low-angle subduction.

3.3 BACKGROUND

In southern Alaska, the Pacific Plate is subducting to the northwest beneath the North American plate at approximately 5 cm/yr a (see Figure 3.1) (Plattner et al., 2007; Elliott et al., 2010; Argus et al., 2010; Worthington et al., 2012; Bauer et al., 2014; Ward et al., 2015). Within our study region, the Yakutat plateau is subducting along with the Pacific plate at an angle of approximately 7 degrees, and then steepens to approximately 24 degrees at 400 km inboard from the trench (Figure 3.1). Subduction has been ongoing in Alaska for the last 213 Ma (Rioux et al., 2010), but low-angle subduction is thought to have initiated in this region ~20 Ma and is associated with the subduction of the 20 km thick Yakutat oceanic plateau (Bruns, 1983; Davis and Plafker, 1986, Bauer et al., 2014).

The Yakutat block is a microplate wedged between the North American and Pacific plates at the southeastern margin of Alaska (Figure 3.1), and it is theorized that this oceanic plateau formed at the Yellowstone hotspot (Wells et al., 2014) as the conjugate to the Siletzia Province that accreted to present-day Oregon. The Yakutat then traveled north with the Pacific Plate to its present position along the Queen Charlotte-Fairweather fault system (Davis and Plafker, 1986; Wells et al., 2014). The Yakutat crust consists of an oceanic plateau approximately 20-27 km thick (overlain by many kilometers of sediments in some parts) (Veenstra et al., 2006; Christeson et al., 2010, Bauer et al., 2014) that is accreting to the Alaskan continent in the east, and subducting at a low angle along with the Pacific Plate at its western edge (in our study region). Magnetic and gravity studies conducted in the FSS region indicate that much of the sediments that overlay the Yakutat oceanic plateau are being subcreted near the Cook Inlet in Alaska (Mankhemthong et al., 2013).

The FSS region in Alaska is characterized by the absence of arc volcanism and this region, devoid of modern volcanism, is referred to as the Denali gap (Plafker and Berg, 1994; Nye, 1999; Eberhart-Phillips et al., 2006; Wang and Tape, 2014; Martin-Short et al., 2016). This lack of volcanic activity occurs due to the cut-off of corner-flow in the mantle above the flat slab, which results in the absence of an asthenospheric wedge and cooler conditions than in a typical subduction zone.

Several mechanisms have been hypothesized to explain low-angle subduction, including young, hot (and presumably buoyant) oceanic lithosphere, fast trenchward overriding plate motion, fast subduction rate, overthickened and mechanically strong aseismic ridges/oceanic plateaus, and the presence of water in subducting slabs (Vlaar, 1983; Gutscher et al., 2000; van Hunen et al., 2000; van Hunen et al., 2002; English et al., 2003; Ramos and Folguera, 2009; Skinner and Clayton, 2010; Manea et al., 2011; Porter et al., 2012; Gardner et al., 2013; Knezevic Antonijevic et al., 2015; Ma and Clayton, 2015; Petersen et al., 2021). In the case of Alaska, many of these hypotheses can be ruled out. The subducting oceanic lithosphere is not especially young (55 Ma), and the subduction rate and overriding plate motion are not especially high (5 cm/yr and 2.3 cm/yr respectively). Plate rigidity could potentially prevent an anhydrous Yakutat slab from subducting (per van Hunen et al., 2002), but is not necessary to sustain FSS in Alaska with the presence of a modest amount of hydration (1-1.5 % chemically bound water in the subducting slab) (Petersen et al., 2021).

The amount of water and distribution of hydration throughout the subducting crust and mantle needs further investigation. It is thought that water is introduced into subducting slabs via fracture networks in the oceanic crust (Peacock, 2001; Ranero et al., 2003; Lefeldt et al., 2012) that may allow water to penetrate as deep as 20 km into the slab's lithospheric mantle (Seno and Gonzalez, 1987; Seno and Yamanaka, 1996; Ranero et al., 2003; Kopp et al., 2004; Fromm et al., 2006; Clouard et al., 2007; Lefeldt et al., 2012; Porter et al., 2012). Serpentinized mantle velocities are greatly reduced relative to anhydrous peridotite, and should be noticeable in seismic imaging if present in significant quantities (i.e. Peacock, 1993; Hacker et al., 2003). We expect that hydration is concentrated along faults and fractures in the crust, and that these fractures serve as the primary pathway for introducing water into the upper mantle. Therefore, for the purpose of calculating stable mineral assemblages, we consider an assumption of water-saturation along fractures to be appropriate, and that portions of the crust and upper mantle not close to fractures are likely unaltered/anhydrous.

Within subducting slabs, seismic velocities are reduced with the presence of hydrous minerals with the effects most pronounced in the mantle. For example, anhydrous peridotites are largely composed of forsterite (Mg-olivine), which has P and S wave velocities of 8.59 km/s and 4.95 km/s respectively at 500°C and 3.0 GPa (Abers and Hacker, 2016). When water is introduced, forsterite becomes antigorite (Mg-serpentine), which has P and S wave velocities of 6.89 km/s and 3.78 km/s respectively (Abers and Hacker, 2016). Within the crust anhydrous metamorphosed gabbroic crust is largely composed of pyroxenes and almandine (garnet) at 30-150 km depth (Petersen et al., 2021). Pyroxenes generally have P and S wave velocities of 6.62-9.38 km/s and 3.55-5.22 km/s respectively at 500°C and 3.0 GPa (variations depending on composition). Almandine has P and S wave velocities of 8.36 km/s and 4.66 km/s at the same conditions. When hydration is introduced to metamorphosed gabbros, the hydrous minerals lawsonite (8.03 km/s P wave, 4.05 km/s S wave), amphiboles such as glaucophane (7.8 km/s P wave, 4.53 km/s S wave), and small amounts of chlorite (7 km/s P wave, 3.56 km/s S wave) are formed (Petersen et al., 2021). The seismic velocities mentioned above are taken from Abers and Hacker (2016). With some dependence on modal distribution, the seismic velocities are only slightly reduced in gabbros (up to 0.5 km/s P wave, 0.4 km/s S wave) with the introduction of hydration, while hydrous peridotites have much greater velocity reductions (up to 1.5 km/s P wave, 1 km/s S wave).

3.4 METHODS

3.4.1 Thermal and Phase Equilibria Modeling

We use results from previously published thermal and phase equilibria models to estimate seismic velocities for the Alaskan flat slab region (Petersen et al., 2021). To estimate mineral assemblages, we use the results produced by a finite difference thermal modeling code (*ThermodSubduct*) with 2 km grid resolution (see Figure 3.2). *ThermodSubduct* is designed for modeling the time-dependent thermal evolution of subduction zones through time (Petersen et al., 2021). The thermal modeling in Alaska incorporated shear heating along the fault (effective frictional coefficient of 0.03) and isoviscous mantle cornerflow in the mantle wedge region, below 50 km depth. The fault geometry used for our modeling is shown in Figure 3.2, which shows the subduction trench at 150 km the A-A’ across the transect. The slab subducts at approximately seven degrees, steepening to 24 degrees at ~550 km across the A-A’ transect (400 km from the trench). We use in this study the temperature outputs calculated at 20 m.y., which is the approximate length of time that FSS has been ongoing in southeastern Alaska (Finzel et al., 2011).

For our numerical simulations, we assume that the subducting slab is 80 km thick (the top 20 km being oceanic crust) based on models of lithospheric age and the depth of the lithosphere-asthenosphere boundary (LAB) determined in previous Sp receiver function studies of the Alaskan region (Kumar and Kawakatsu, 2011; O'Driscoll and Miller, 2015). We assume for our numerical models that the thickness of the overlying Alaskan continental crust is 35 km thick based on receiver function studies (Veenstra et al., 2006; O'Driscoll and Miller, 2015).

We calculated stable mineral assemblages using *Perple_X* (Connolly, 2005). This code calculates stable mineral assemblages given a user-specified bulk composition and specified pressure-temperature ranges, solution models, and a thermodynamic dataset. The bulk composition assumed for the Yakutat basalt, which we applied to the upper 5 km of the subducting crust, is the average of 19 analyses of ocean floor drill samples reported in Davis and Plafker (1983). Our previous work (Petersen et al., 2021) compared the mineral phases predicted by *Perple_X* for both the Yakutat basalt composition and a general mid-ocean ridge basalt (MORB) composition (Gale et al., 2013), and found that results were similar. For the purpose of studying the Alaskan FSS zone, we prefer the use of the Yakutat basalt composition over that of the MORB, as it likely is a better estimate of bulk crustal composition for the Yakutat upper crust.

For the lower 15 km of the subducting oceanic crust, we assumed a composition determined by averaging the analyses of 176 oceanic gabbro samples (Niu et al., 2002). We assumed a depleted MOR mantle (DMM) peridotite composition from Workman and Hart (2005) for the simulation of mineral stabilities below the slab Moho (20-80 km depth). Within this 60 km- thick lower layer of the slab, we consider that hydration is limited to the upper 10 km of the subducting mantle, localized along cracks and fractures, with anhydrous peridotite in between. We simulate these conditions by using a weighted average of anhydrous and water-saturated peridotite simulations, discussed in more detail later on. All calculations (including those models that are water-saturated) assume that the lower 50 km of the slab is completely anhydrous. We find this to be a reasonable assumption due to the fact that the overlying anomalously thick (20 km) Yakutat crust may present an obstacle to water infiltrating to depths below the Moho, as found in typical subduction zones (i.e. 15-30 km below the Moho in Fromm et al., 2006; Lefeldt et al., 2012), where the oceanic crust is only 5-10 km thick.

Our mineral assemblage calculations were done using the *Perple_X* dataset HP11ver (Holland and Powell, 2011). More information on the *Perple_X* methodology used for this study can be found in Petersen et al. (2021). *Perple_X* simulations of stable mineral assemblages predict that metamorphic dehydration reactions begin hundreds of kilometers inboard of the trench (Petersen et al., 2021). Metamorphic reactions are likely inhibited until temperatures exceed 250°C and 0.5 GPa. This is due to kinetic impediments to hydration reactions at low temperatures. This temperature is first exceeded in the crust at approximately X=250 km on our model across the A-A' transect (100 km from the trench, see Figures 3.1 and 3.2). For a more detailed overview of the methodology used for our temperature, pressure, and *Perple_X* mineral assemblage calculations, see Petersen et al., (2021).

For each composition (basalt, gabbro, and peridotite), we calculated a completely anhydrous and fully water-saturated model. In order to vary the amount of hydration in our models, we use a weighted average of the two models (water-saturated and anhydrous) in order to simulate a slab that has hydration concentrated along faults and fractures. These variations in weighting are used to simulate variable degrees of fracturing which, in turn, would lead to variable hydration. While it is difficult to quantify the amount of faulting and fracturing within the already-subducted Yakutat plateau, we tested various degrees of hydration in order to compare results with observational seismic studies in the Alaska region.

3.4.2 Calculation of Seismic Velocities from Phase Equilibria Results

We use the methodology of Abers and Hacker (Hacker and Abers, 2004; Abers and Hacker, 2016) to calculate seismic velocities for this study. Although certain *Perple_X* thermodynamic databases incorporate mineral data for seismic wave velocities and can be used to predict seismic wave velocities, we have opted against them for several reasons. Firstly, we chose the HP11ver database (Holland and Powell, 2011) for our phase equilibria calculations in order to incorporate silicate mineral phases that include Fe^{3+}-bearing components. Because the incorporation of Fe^{3+} into metamorphic phase equilibria can significantly affect the calculation of mineral assemblages, we consider Fe^{3+} important to incorporate (i.e. Cottrell and Kelley, 2011). However, the HP11ver database does not allow for the prediction of seismic wave velocities. Secondly, although *Perple_X* has a more extensive mineral database for seismic wave speed velocities than the Abers and Hacker Matlab toolbox, the methodology of *Perple_X* is dependent on mineral laboratory experiments. Concerns have been raised about the *Perple_X* method of seismic velocity calculation, as the alteration and retrogression of exposed natural samples tends to reduce their wave speeds relative to the same rocks at depth (Carlson, 2014), and requires accurate pressure and temperature derivatives in order to extrapolate to conditions at depth (Aber and Hackers, 2016). Alternatively, Abers and Hacker predict seismic velocities based on rock composition, where mineral abundances are known and the minerals used have adequately described mineral elastic properties (Bina and Helffrich, 1992; Abers and Hacker, 2016). The Abers and Hacker approach therefore only uses minerals that have proper measurements of shear moduli, or it can be estimated from the isothermal bulk modulus (Hacker and Abers, 2004). If no derivative terms are available, they are scaled from those of similar minerals

(Hacker and Abers, 2003). We therefore prefer the Abers and Hacker methodology for the prediction of seismic wave speeds in our work.

We used the updated version of the 2004 Hacker and Abers toolbox (Hacker and Abers, 2004; Abers and Hacker, 2016) and imported the mineral assemblages calculated within *Perple_X* into the Abers and Hacker Matlab toolbox. As the *Perple_X* mineral database is more extensive, corresponding mineral conversions were used to reflect analogous assemblages in the Abers and Hacker database. We present our selection of minerals used within the Abers and Hacker toolbox from those predicted by *Perple_X* in Table 1.

As the Abers and Hacker toolbox does not contain seismic wave speeds for every mineral we predicted using *Perple_X*, we had to make some assumptions about these minerals. For example, small amounts of corundum were predicted in our *Perple_X* calculations for anhydrous peridotite, but this mineral is not contained within the Abers and Hacker database. We changed the small amount of corundum (Al_2O_3 <2% by volume) contained in our bulk composition to sillimanite (Al_2SiO_5) for our seismic wave speed calculation, a high-T aluminum silicate. For all the minerals we converted in this manner, their bulk composition was <2% by volume, and we do not expect these conversions to have greatly affected our seismic wave speed calculations.

Using the Abers and Hacker toolbox, we generated tables of seismic wave speed values for each starting major oxide composition across a 100x100 grid of possible temperatures and pressures. We then query these tables at temperatures and pressures predicted within our thermal model (see Figure 3.2). These were then used to generate 2D cross sections of seismic velocity across our A-A’ transect (Figure 3.1) for P wave velocities, S wave velocities, and Vp/Vs. Vp/Vs ratios were calculated by dividing our S wave velocity results by our P wave velocity calculations. We show Vp/Vs ratios in addition to P and S-wave velocities, as a high Vp/Vs ratio can be indicative of the presence of hydration - especially serpentinization (Christensen, 1996; Hyndman and Peacock, 2003; Rossi et al, 2006).

We calculated results for a fully anhydrous slab, a water-saturated slab (with the exception of the anhydrous lower 50 km, as shown in the top panel of Figure 3.2), and three separate hybrid models of hydration. The hybrid models weigh the water-saturated and anhydrous results in the upper crust, lower crust, and upper mantle. Because a constant Vp/Vs ratio is assumed for each layer (upper crust, lower crust, and upper mantle), localized regions of hydration within layers that might exist are not represented. However, the P- and S-wave seismic tomography that we use for comparison integrates data over broad regions (Nayak et al., 2020), so we do not consider this to be an issue for our modeling approach.

For our hybrid models, we test three different models of varying hydration. Model 1 weighs 50% to the saturated model in the upper 5 km of the crust (basaltic layer), equating to 2.7% chemically bound water, and is anhydrous throughout the remainder of the slab. Model 2 weighs 35% to the saturated model in the upper 5 km of the crust (~1.0-1.8 wt% H_2O), 30% to the saturated model in the lower gabbroic crust (~1-1.5 wt% H_2O), and 25% to the saturated model in the upper 10 km of the subducting mantle (~1-2 wt% H_2O). Model 3 weighs 60% to the saturated model in the upper 5 km of the crust (~2-3 wt% H_2O), 55% to the saturated model in the lower gabbroic crust (~2.4-2.6 wt% H_2O), and 40% to the saturated model in the upper 10 km of the subducting mantle (~1.8-3 wt% H_2O).

We chose these three models of hydration in order to represent three potential hydration scenarios within the subducting slab. Model 1 represents a slab that has hydration limited to the upper crust, with little alteration occurring at depth. This could be interpreted as an essential anhydrous slab, with little fracturing occurring at depth, and most alteration occurring due to seafloor interaction near the surface. Model 2 represents a conservative amount of hydration occurring throughout the crust and into the mantle (1-2% chemically bound water, decreasing as the slab subducts and dehydrates). Model 3 represents a slab much more hydrated than the other two models, with chemically bound water in all hydrated layers at ~3%, decreasing as the slab subducts and dehydrates.

3.4.3 Overview of Published Seismic Velocity Models Used in This Study

For this study we assessed the potential application of several recent seismic studies in Alaska, and selected two seismic studies (from Nayak et al., 2020) to compare with our forward modeling results. Although many other seismic velocity models for Alaska exist (i.e. Eberhart-Phillips, 2006; Wang and Tape, 2014; Ward, 2015; Jiang et al., 2018; Martin-Short et al., 2018; Ward and Lin, 2018; Feng and Ritzwoller, 2019; Berg et al., 2020), we selected the models that provide the best results for application to our study region in terms of station coverage, data extent, and methodology.

These two models incorporate seismic data from the EarthScope Alaska Transportable Array, Southern Alaska Lithosphere and Mantle Observation Network, and onshore stations of the Alaska Amphibious Community Seismic experiment. The models use methods that show improvements (compared with other Alaskan seismic tomography studies) in resolution in the crust and uppermost mantle due in part to the inclusion of short-period stations and recently deployed temporary and permanent broadband stations (Nayak et al., 2018; Nayak et al., 2020). They also showed particular improvements in resolution compared with other studies in the southeastern region of Alaska where this study is focused (Nayak et al., 2020).

The first model used in this study (model AKEP2020) covers a region 1900 km north-northeast-south-southwest by 1600 km east-southeast-west-northwest centered on Anchorage. The second model (AKAN2020) covers a region extending 46.4° in longitude and 21.2° in latitude centered on 61.5° north, 150° west. Thus, the AKEP2020 model used in this study has higher resolution in the FSS region of Alaska (25-km inversion grid), while the

AKAN2020 model covers a larger geographical area, but has coarser resolution (40-km inversion grid). AKEP2020 represents the model domain with an earth-flattening Cartesian system, while AKAN2020 represents the model domain in spherical geographic coordinates.

The two models incorporate regional body-wave data and surface-wave data from ambient noise in a joint inversion for Vp and Vs (AKAN2020) or Vp and Vp/Vs (AKEP2020) using two different joint inversion methods. AKEP2020 uses a joint inversion method using the Eberhart-Phillips and Fry (2017) algorithm, while the AKAN2020 model uses a joint inversion with the Fang et al. (2016) algorithm. Differences between the two models can be attributed to the differences in geographical extent and resolution, as well as the type of measurements (group velocity in AKEP2020 vs. phase velocity in AKAN2020), model parameterization, and accounting for finite-frequency effects (Nayak et al., 2020). Both models have sufficient resolution to 100 km depth.

3.5 RESULTS

We present our P wave velocity forward modeling results calculated using the Abers and Hacker Matlab toolbox and plotted along the A-A’ transect (Figure 3.1) in Figure 3.3. We show results with an anhydrous slab, a fully saturated slab, and hybrid models 1-3. Model 1 represents the least hydrous scenario of the three hybrid models while Model 3 represents the most hydrous. We present the anhydrous and saturated results as endmembers for our various hydration scenarios. In Figure 3.4, we show the P wave velocity models AKEP2020 and AKAN2020 (Nayak et al., 2020) along the same 850 km cross section of A-A’ (Figure 3.1). We note that the AKEP2020 and AKAN2020 models calculated similar velocities within the subducting crust, but AKAN2020 has slightly lower velocities in the subducting mantle (up to 0.5 km/s slower).

Our S wave velocity modeling results are shown in Figure 3.5, and show the same hydration states and compositions as those seen for P wave velocities in Figure 3.3. Figure 3.6

presents the AKEP2020 and AKAN2020 S wave velocity models. Similar to the P wave velocity results in Figure 3.4, the two S wave models calculated similar velocities in the subducting crust, with slight differences in the subducting mantle. Again, AKAN2020 S wave velocities are slower than those calculated in the AKEP2020 model by up to 0.3 km/s.

Our estimated Vp/Vs ratios are shown in Figure 3.7 for an anhydrous slab, saturated slab, and all three hybrid models. AKEP2020 and AKAN2020 Vp/Vs ratios are shown in Figure 3.8. Here we see that Vp/Vs ratios are much higher in AKAN2020 within the subducting crust and mantle when compared with AKEP2020. Ratios are close to 2 for AKAN2020 in the subducting crust between 300 and 600 km across the transect, while in this same region the AKEP2020 model has a Vp/Vs values ranging from 1.79-1.83. The Vp/Vs ratios produced by the AKAN2020 model are very high, and we prefer the more typical ratios produced by the AKEP2020 model.

Figures 3.9, 3.10, and 3.11 present Vp, Vs, and Vp/Vs values for all models at 500 km across the A-A’ transect (Figure 3.1). In these figures, we can compare the values from our calculations with those of AKEP2020 and AKAN2020. In each figure we present both an unsmoothed and smoothed version of our forward models for comparison with AKEP2020 and AKAN2020. We do this because the seismic tomography models AKEP2020 and AKAN2020 have lower resolution (25-km horizontal resolution for AKEP2020 and 40 km horizontal resolution for AKAN2020) than the 1-km node spacing used in our calculations. Thus, vertical smearing and lower resolution will cause any sharp changes in seismic wave speeds to be smoothed in the seismic tomography models. In order to better compare between our forward models and the seismic tomography models AKEP2020 and AKAN2020, we used a moving mean smoothing parameter on our forward modeling results that is shown in the lower panel of Figures 3.9-3.11.

The Vp and Vs values predicted (Figures 3.9 and 3.10) for our anhydrous model (plotted in red) are generally much higher than either AKEP2020 or AKAN2020 (plotted as black lines). Our saturated results presented in Figures 3.9 and 3.10 (plotted in blue) are generally lower than either AKEP2020 or AKAN2020, with the exception of the anhydrous portion of the slab. As previously discussed, this layer was assumed to be anhydrous in all models, including the water-saturated model. Our hybrid models are plotted in green. Our Model 3 best matches the P-wave velocities observed in both AKEP2020 and AKAN2020 (Figure 3.9). Both Model 3 and our saturated model match closely with AKEP2020 and AKAN2020 for S wave velocities (Figure 3.10).

In Figure 3.11, we see that our anhydrous model (plotted in red) has lower Vp/Vs than either AKEP2020 or AKAN2020 (plotted in black). The estimated Vp/Vs ratios for the water-saturated model (plotted in blue) are higher in the subducting slab than the AKEP2020 model. However, even our water-saturated model's Vp/Vs ratios are lower values than those of AKAN2020 in all regions of the slab. Our hybrid models (plotted in green) again show that Model 3 more closely matches the values of AKEP2020 than Model 1 or 2.

In Figure 3.12 we show the predicted effects of hydration by mapping the difference in P- and S-wave seismic velocities between our water-saturated and anhydrous models. Water-saturated regions of the mantle show a much greater reduction in seismic wave speeds (up to 1.5 km/s P wave and 1 km/s S wave) than regions of oceanic crust (up to 0.7 km/s P wave and 0.6 km/s S wave). Comparing our calculations of P and S wave velocities (Figures 3.3 and 3.5 respectively) with the seismic imaging for P and S wave velocities (Figures 3.4 and 3.6 respectively), we see that the velocities predicted by our model for an anhydrous slab are much higher than observed in either the AKEP2020 or AKAN2020 models. Our hybrid Model 1 only assumes hydration in the upper 5 km of the subducting crust, and we see that this scenario also predicts higher P and S wave speeds in the majority of the slab than indicated in the seismic tomography data.

Model 2 in Figures 3.3 and 3.5 assumes a moderate amount of hydration in the slab, equating to about 1-1.5 % chemically bound H_2O in the subducting crust (20 km thick) and hydrated portion of the subducting mantle (10 km thick). In the crust, the velocities predicted by this model are approximately 4.5-4.6 km/s (S wave) and 7.7-7.9 km/s (P wave). AKEP2020 measures seismic velocities of approximately 4.1-4.2 km/s (S wave) and 7.2-7.5 km/s (P wave) in the crust. AKAN2020 observes even lower velocities, but has coarser grid spacing and lower resolution than AKEP2020. Our Model 2 therefore estimates slightly higher seismic velocities than either AKEP2020 or AKAN2020 in the crust. In the upper (hydrated) slab mantle, Model 2 also predicts higher velocities than is observed. This can be seen clearly in Figures 3.9 and 3.10 at 500 km across the A-A’ transect.

Model 3 in Figures 3.3 and 3.5 assume approximately 3% chemically bound H_2O in the subducting crust and hydrated portion of the subducting mantle. Model 3 predicts S wave velocities of approximately 4.2-4.4 km/s (crust) and 4.4-4.6 km/s (upper mantle), and P wave velocities of approximately 7.5-7.7 km/s (crust) and 7.9-8.0 km/s (upper mantle). These values are more similar to those of AKEP2020 and AKAN2020, where we observe S wave velocities of 4.0-4.4 km/s in the crust and 4.3-4.6 km/s in the upper mantle. P wave velocities in AKEP2020 and AKAN2020 are 7.3-7.7 km/s in the crust and 7.9-8.0 km/s in the upper mantle. In Figure 3.9 we see that the smoothed version of Model 3 (lower panel) is a close match to the seismic tomography models AKEP2020 and AKAN2020 for P wave velocity. In Figure 3.10 which shows the S wave velocity predictions at 500 km across the A-A’ transect, we see that AKEP2020 and AKAN2020 are most similar to the saturated and Model 3 predictions. Our saturated model predicts slightly lower S wave velocities than AKEP2020, and Model 3 predicts slightly higher S wave velocities.

The Vp/Vs ratio results vary between AKEP2020 and AKAN2020 models (see Figures 3.8 and 3.11). Particularly between 300-500 km across the A-A’ transect and between 25-75 km depth, AKAN2020 has a Vp/Vs ratio of up to 0.06 higher than AKEP2020. The AKEP2020 inversion solves for Vp and Vp/Vs directly, whereas for AKAN2020, the inversion solves for Vp and Vs. It is widely recognized that a Vp/Vs model obtained by dividing Vp by Vs is prone to substantial artifacts (Eberhart-Phillips, 1990; Thurber and Ritesma, 2015; Watkins et al., 2018; Nayak et al., 2020). We therefore focus our Vp/Vs interpretation using the AKEP2020 model only.

The AKEP2020 Vp/Vs model (upper panel, Figure 3.8) shows high ratios (1.79-1.85) in the subducting slab between 400-600 km across the A-A’ transect and between 25-80 km depth. In this region, our saturated model or hybrid model 3 most closely matches the values predicted by the AKEP2020 model (see Figures 3.7 and 3.11). The similarities here could be indicative of hydration, however there is some uncertainty as to the interpretation of Vp/Vs ratios (Wagner et al., 2019). The results are indicative of hydration, but this identifies an area where more work is needed from both a mineral physics and observational seismology standpoint.

Table 3.1. Conversions used from *Perple_X* predicted mineral assemblages to those in the Abers and Hacker (2016) database.

Basalt		Gabbro		Peridotite	
Perple_X predicted minerals	Hacker and Abers	*Perple_X* predicted minerals	Hacker and Abers selection	*Perple_X* predicted	Hacker and Abers selection
Anhydrous minerals					
clinopyroxene (acmite)	ac (acmite)	orthopyroxene (Fe-Mg)	en (enstatite)	olivine	fo (forsterite)
garnet (Fe1.6, Mg1.2, Ca.2)	alm (almandine)	garnet (Fe2, Ca.6, Mg.4)	alm (almandine)	garnet (Mg)	py (pyrope)
quartz	qz (quartz)	clinopyroxene 1 (Ca-Mg)	di (diopside)	clinopyroxene	di (diopside)
rutile	rut (rutile)	clinopyroxene 2 (Na-Al-Mg-Fe)	cats (Ca-Tschermack pyroxene)	orthopyroxene	en (enstatite)
magnetite	mt (magnetite)	kyanite	ky (kyanite)	ilmenite	ilm (ilmenite)
spinel	sp (spinel)	quartz	qz (quartz)	spinel	sp (spinel)
kyanite	ky (kyanite)	rutile	rut (rutile)	corundum	sill (sillimanite)
orthopyroxene (enstatite)	en (enstatite)	albite	lAb (low-temperature albite)	rutile	rut (rutile)
sphene	ttn (titanite)	ilmenite	ilm (ilmenite)		
ilmenite	ilm (ilmenite)				
albite	lAb (low-T albite)				
Saturated minerals					
quartz	qz (quartz)	lawsonite	law (lawsonite)	olivine	fo (forsterite)
rutile	rut (rutile)	clinopyroxene (Ca-Mg)	di (diopside)	clinopyroxene	di (diopside)
garnet (Fe1.6, Mg1.2, Ca.2)	alm (almandine)	chlorite (Mg-chlorite)	clin (clinochlore, Mg chlorite)	chlorite (Mg-chlorite)	clin (clinochlore, Mg chlorite)
clinopyroxene (acmite)	ac (acmite)	amphibole (glaucophane)	fgl (ferroglaucophane)	antigorite	atg (antigorite)
chlorite (Mg-chlorite)	clin (clinochlore, Mg	garnet (Fe1.6, Mg1.2, Ca.2)	alm (almandine)	garnet (pyrope)	py (pyrope)
biotite (phlogopite)	phl (phlogopite)	quartz	qz (quartz)	orthopyroxene	en (enstatite)
mica (muscovite)	mu (muscovite)	rutile	rut (rutile)	ilmenite	ilm (ilmenite)
amphibole (glaucophane)	fgl (ferroglaucophane)	talc	ta (talc)		
lawsonite	law (lawsonite)	sphene	ttn(titanite)		
talc	ta (talc)				
sphene	ttn (titanite)				

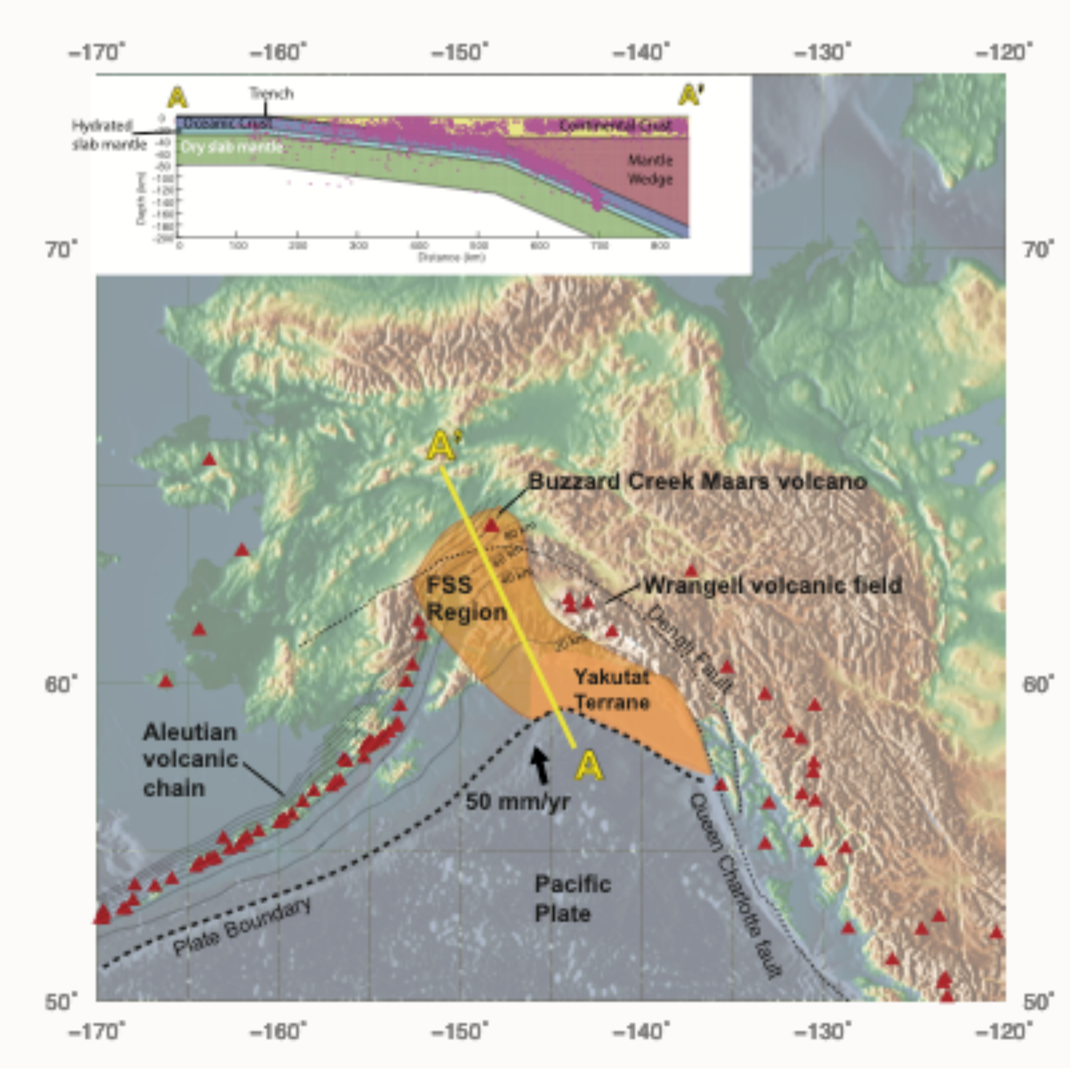

Figure 3.1. Map showing study region in Alaska. A-A’ yellow line shows the 850 km transect through the FSS region used in this study. Flat slab subduction region and associated Yakutat terrane are highlighted in orange. The contours show slab contours with a contour interval of 20 km. Faults are shown as dotted black lines. Red triangles indicate active volcanoes.

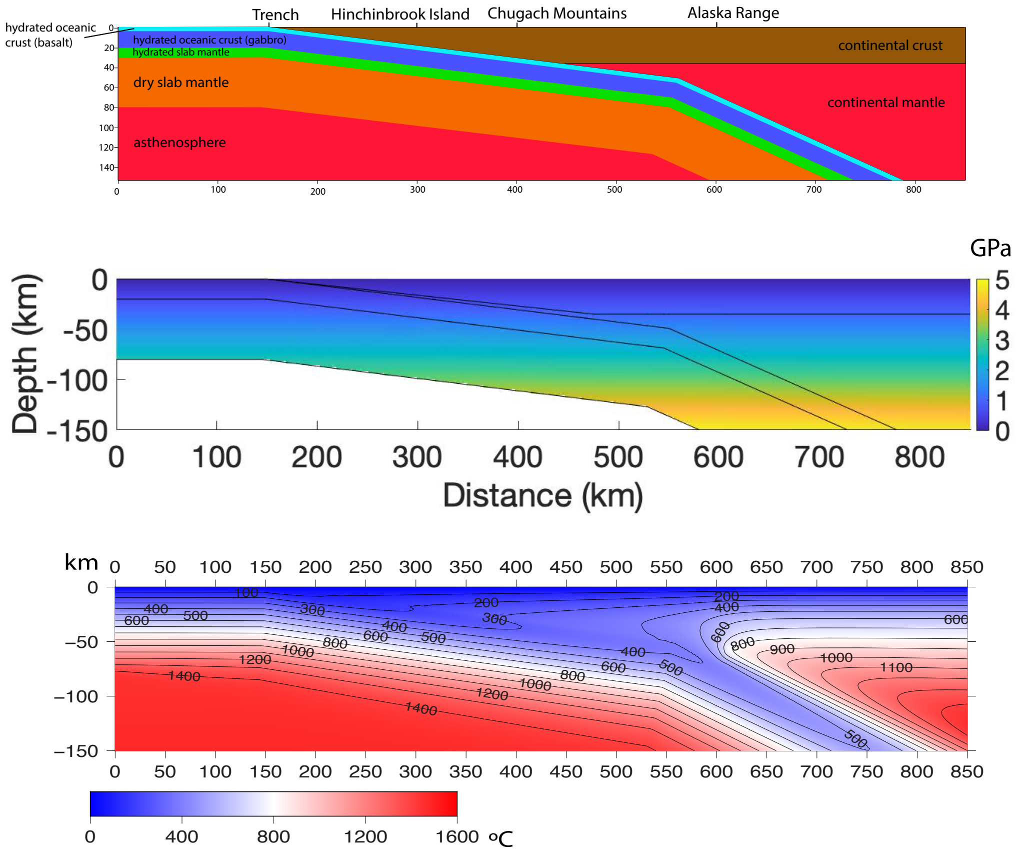

Figure 3.2. Model setup and assumed compositions for this study (top panel), calculated pressures (middle panel), and temperatures calculated using *ThermodSubduct* (lower panel) along the A-A' transect (Figure 3.1).

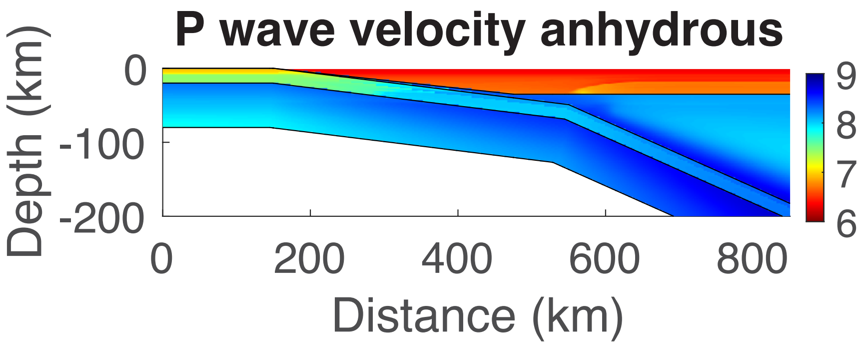
P wave velocity anhydrous
Depth (km)
0
-100
-200
0
200
400
600
800
Distance (km)
9
8
7
6

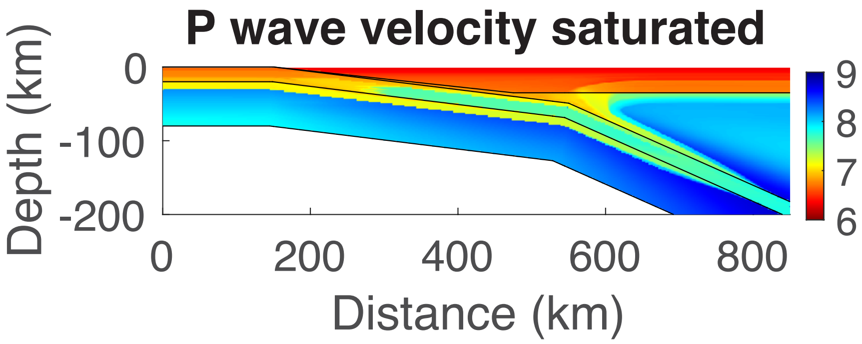
P wave velocity saturated
Depth (km)
0
-100
-200
0
200
400
600
800
Distance (km)
9
8
7
6

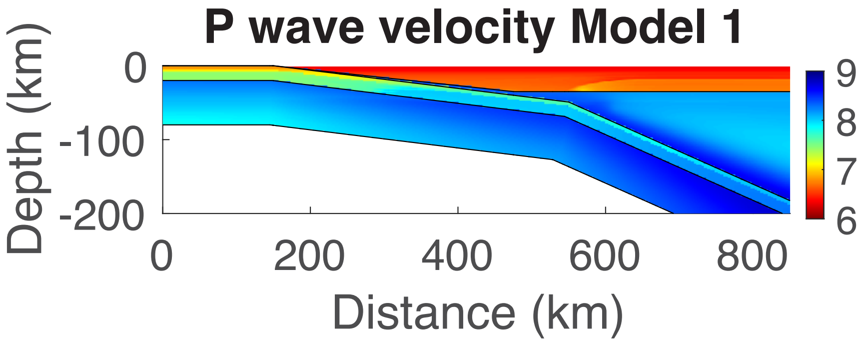
P wave velocity Model 1
Depth (km)
0
-100
-200
0
200
400
600
800
Distance (km)
9
8
7
6

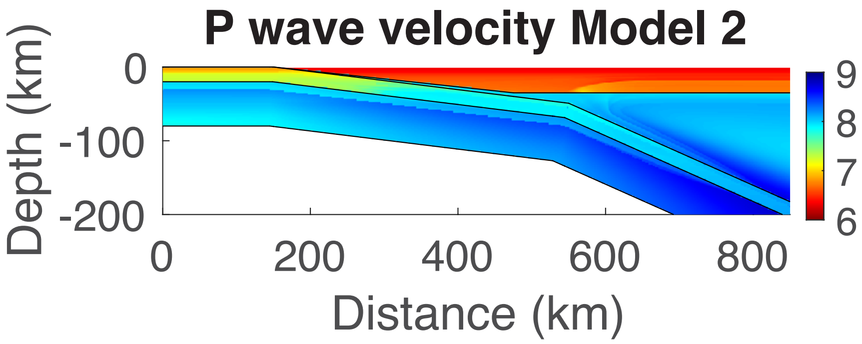
P wave velocity Model 2
Depth (km)
0
-100
-200
0
200
400
600
800
Distance (km)
9
8
7
6

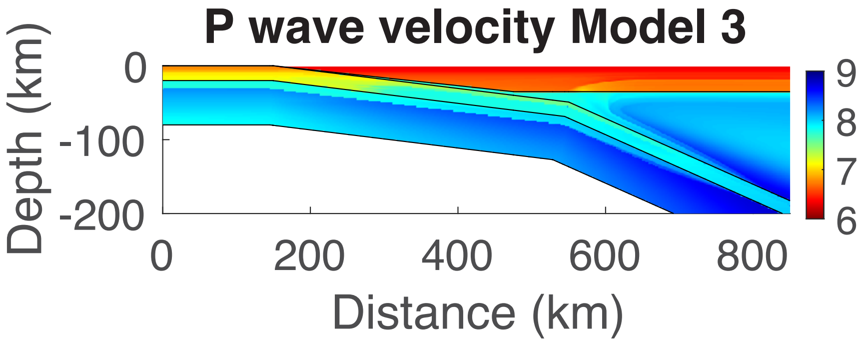
P wave velocity Model 3
Depth (km)
0
-100
-200
0
200
400
600
800
Distance (km)
9
8
7
6

Figure 3.3. P wave velocity models for all models calculated using *Perple_X* assemblages and the Abers and Hacker (2016) Matlab toolbox. Color scale is in km/s. All plots are along the A-A' transect (Figure 3.1).

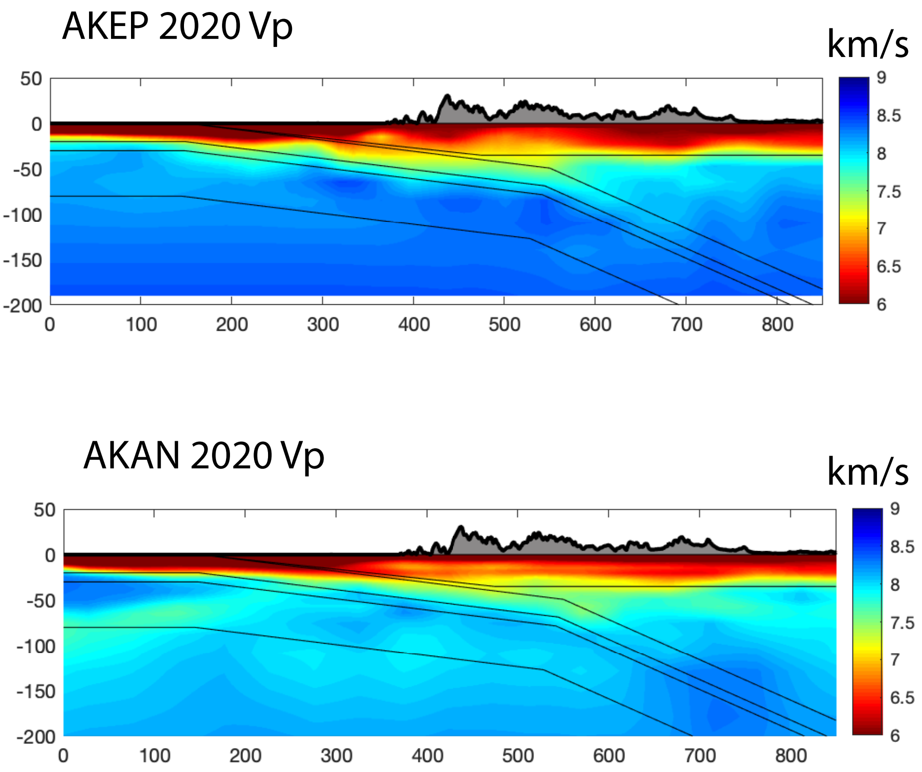

Figure 3.4. P wave velocity models AKEP2020 (top) and AKAN2020 (bottom). Color scale is in km/s. Plots are along the A-A' transect (Figure 3.1).

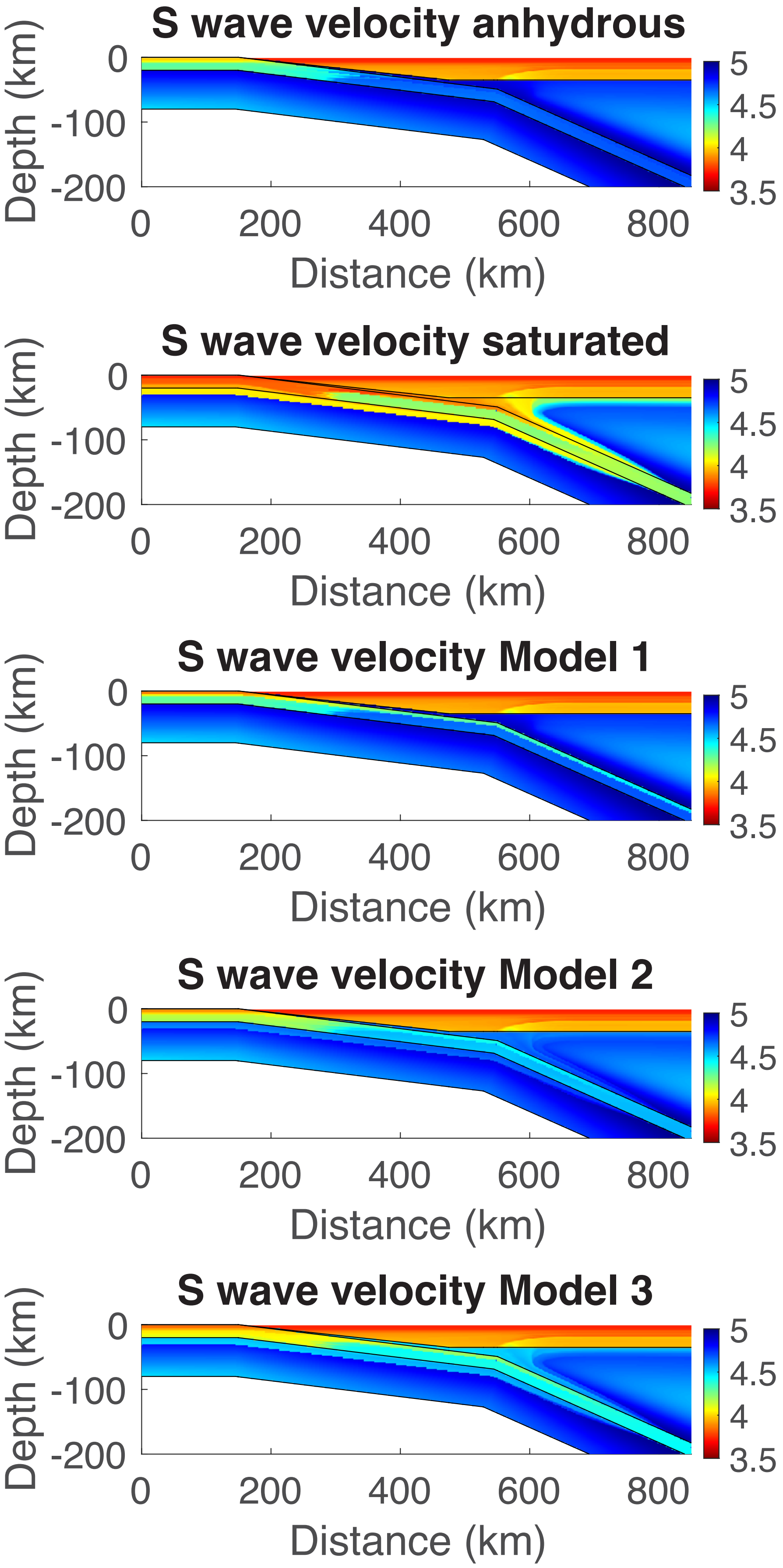
S wave velocity anhydrous
S wave velocity saturated
S wave velocity Model 1
S wave velocity Model 2
S wave velocity Model 3
Depth (km)
0
-100
-200
Distance (km)
0
200
400
600
800
5
4.5
4
3.5

Figure 3.5. S wave velocity models for all models calculated using *Perple_X* assemblages and the Abers and Hacker (2016) Matlab toolbox. Color scale is in km/s. All plots are along the A-A' transect (Figure 3.1).

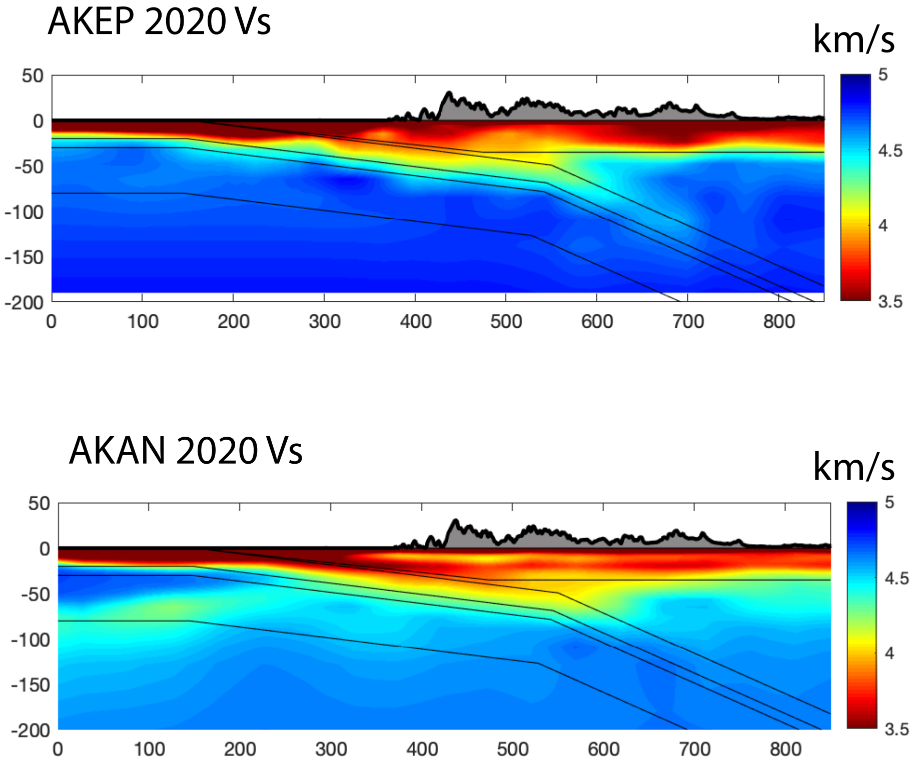

Figure 3.6. S wave velocity models AKEP2020 and AKAN2020. Color scale is in km/s. Plots are along the A-A' transect (Figure 3.1).

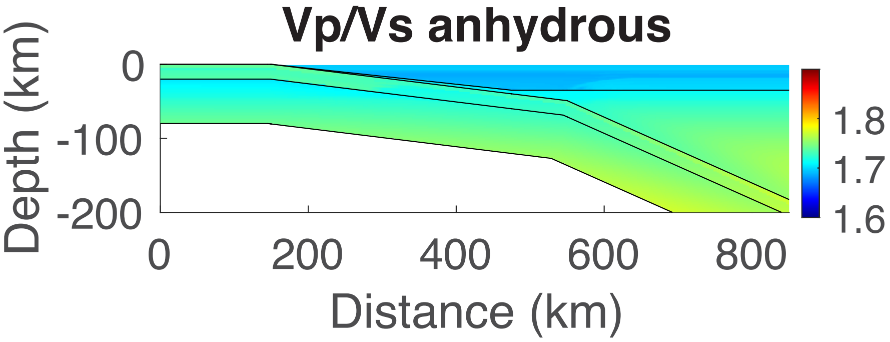
Vp/Vs anhydrous
Depth (km)
0
-100
-200
0
200
400
600
800
Distance (km)
1.8
1.7
1.6

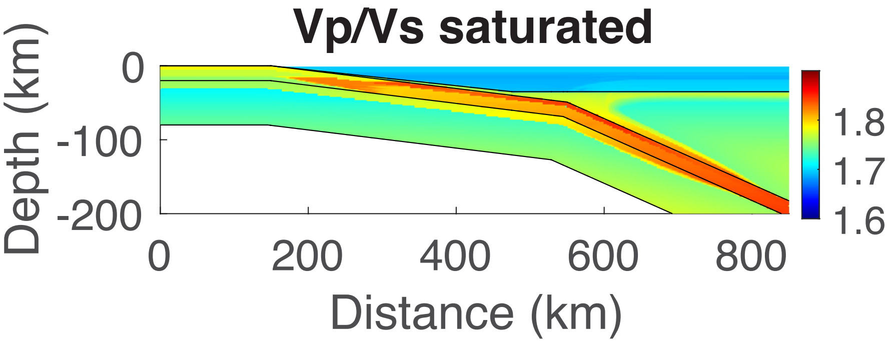
Vp/Vs saturated
Depth (km)
0
-100
-200
0
200
400
600
800
Distance (km)
1.8
1.7
1.6

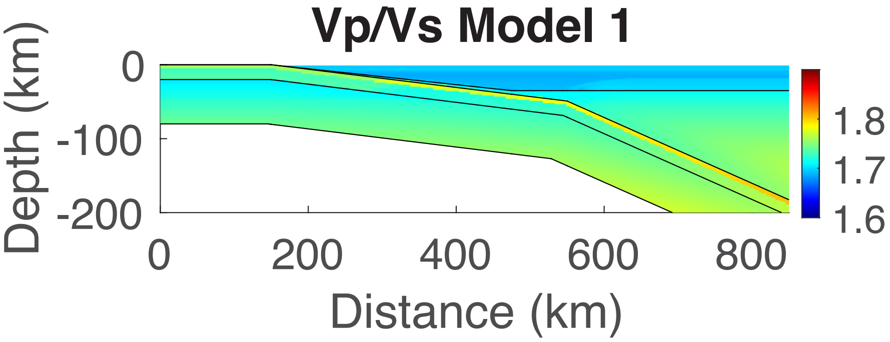
Vp/Vs Model 1
Depth (km)
0
-100
-200
0
200
400
600
800
Distance (km)
1.8
1.7
1.6

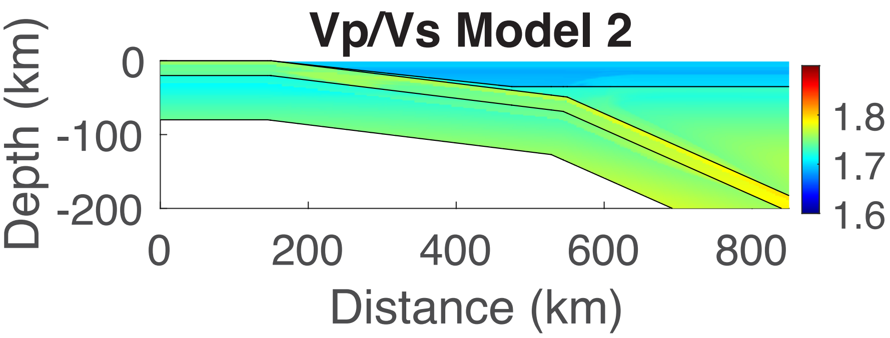
Vp/Vs Model 2
Depth (km)
0
-100
-200
0
200
400
600
800
Distance (km)
1.8
1.7
1.6

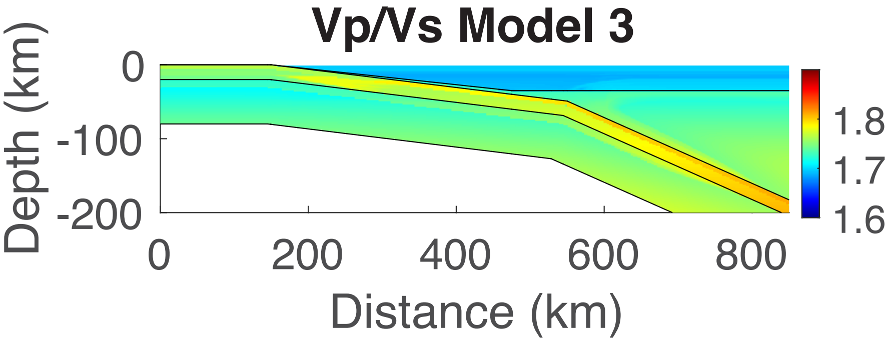
Vp/Vs Model 3
Depth (km)
0
-100
-200
0
200
400
600
800
Distance (km)
1.8
1.7
1.6

Figure 3.7. Vp/Vs ratios for all models calculated using *Perple_X* assemblages and the Abers and Hacker (2016) MATLAB toolbox. All plots are along the A-A' transect (Figure 3.1).

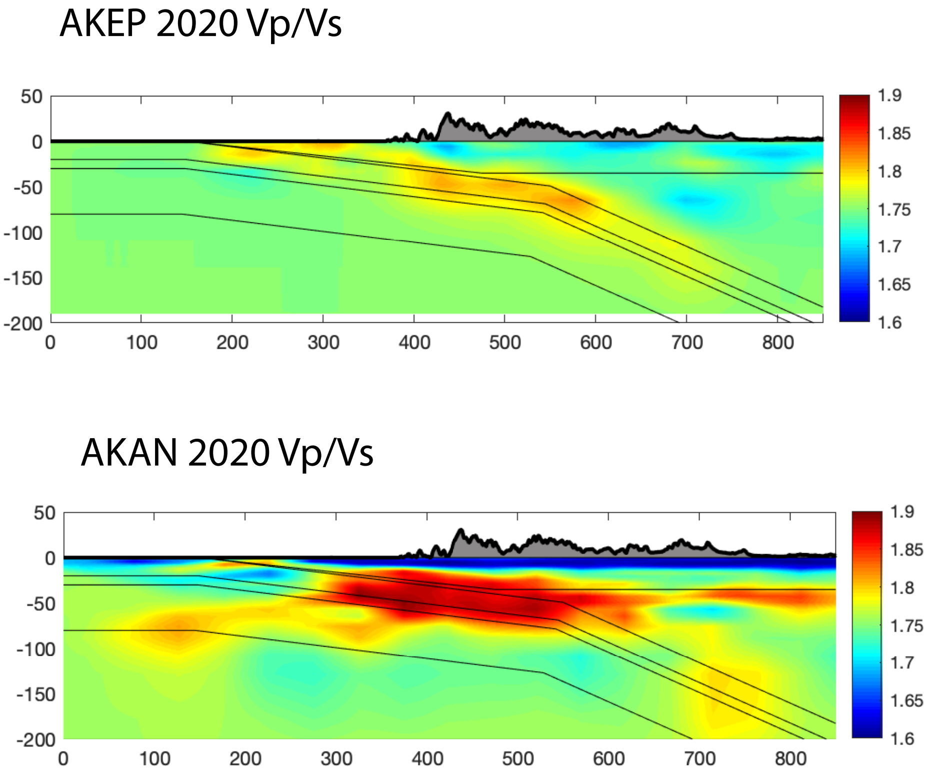

Figure 3.8. Vp/Vs ratio for AKEP2020 and AKAN2020. Plots are along the A-A' transect (Figure 3.1).

3.6 DISCUSSION

Our calculations made using our estimates for temperatures and mineral assemblages as inputs to the Abers and Hacker Matlab toolbox provide several insights into the Alaskan FSS system. We show the effect of hydration on predicted seismic velocities in Figures 3.3 and 3.5. The effect is particularly large in the subducting mantle and overlying mantle wedge (see Figure 3.12). Within the subducting crust, our results show that hydration causes a greater reduction in velocities within the upper basaltic crust than in the lower gabbroic crust. In the upper crust, P wave velocities are reduced by up to 1 km/s and S wave velocities are reduced by up to 0.9 km/s. In the lower gabbroic crust however, hydration reduces P wave velocities by only 0.5 km/s and S wave velocities by 0.4 km/s. One possible reason for this is that the Yakutat basalt has higher amounts of potassium than the gabbroic composition. This can be explained by higher levels of seawater alteration of the basalt near the surface, or could be a reflection of the higher differentiation levels associated with basalts compared with gabbros. Potassium allows for the stabilization of micas, which have relatively low seismic velocities compared to the hydrous amphibole (glaucophane) that is formed in the gabbroic crust.

While our predicted seismic velocities agree well with observational seismic tomography, there are inherent uncertainties in comparing lab-based observations of seismic velocity to field measurements. First, the estimations of seismic velocity wave speeds using the methodology of Abers and Hacker (2016) is not without some uncertainties. The calculations are dependent on lab experimentation to determine elastic properties of various minerals (Hacker et al., 2003; Hacker and Abers, 2004; Abers and Hacker, 2016). Some of these uncertainties can be resolved with further physical measurements, but currently there are still uncertainties in single-mineral thermo-elastic parameters, uncertainties due to calculational approximations, and uncertainties arising from scaling single-crystal data to rock properties (Hacker et al., 2003). There are also uncertainties in the field observations and limitations in resolution as AKEP2020 and AKAN2020 each have much lower grid resolution than our forward models. Finally, seismic tomography is not exclusively sensitive to hydration state as variations in temperature, pressure and composition affect the rock and mineral elastic properties, which, in turn, control seismic velocity. Thus, a region of slower seismic wave speeds could be due to the presence of hydrous rock assemblages like serpentinite, but they could also be due to high temperatures or the presence of melt (Gueguen and Mercier, 1973; Minster and Anderson, 1981; Karato, 1986; Karato and Jung, 1998). However, our thermal modeling results and mineral assemblages predicted by *Perple_X* generally agree with the metamorphic rock record for flat-slab subduction zone systems that are analogous to Alaska, such as the Laramide FSS zone (Usui et al., 2003; Hernández-Uribe and Palin, 2019; Petersen et al., 2021). As we calculated pressure by incorporating densities from our predicted mineral assemblages, our model effectively controls temperature, composition, and pressure. Additionally, the temperatures predicted by our thermal model are too low for the presence of melt. We therefore constrain everything except hydration in order to better interpret seismic wave speeds.

Our hybrid models (Model 1-3) assume a consistent ratio between saturated and anhydrous conditions in each layer, which may be unrealistic. Certain regions of the subducting slab may have greater concentrations of fractures or higher permeability, which would allow for larger volumes of water to interact with the rocks. Portions of the slab may also be subject to rehydration if mineral reactions in the underlying slab release water, which would then migrate upwards and be absorbed into hydrous layers at shallow depths.

Despite the limitations of our forward models and the seismic tomography models, they provide insight into the conditions of the Alaskan FSS zone and indicate that hydration is likely present within the subducting slab. Results are consistent with chemically bound water present at approximately 3 wt %, and possibly higher in some places. Previous work has shown that in this same region of Alaska, an anhydrous model of this subduction zone produces a slab that is too dense to maintain the observed subduction geometry by slab buoyancy alone (Petersen et al., 2021). This same study predicted that at least 1-1.5 wt% water was necessary in the slab to maintain buoyancy (synonymous with our hybrid Model 2 in this study). The results of this study indicate that the seismic velocities predicted for an anhydrous slab are much faster than those observed within the region, and that a slab with 1-1.5 wt% water exhibits slightly higher seismic velocities than what we observe seismically. Even with the uncertainty in our calculations we can therefore conclude that the subducting slab has at least some modest amount of hydration within the slab and that this hydration is contributing to its positive buoyancy.

Reduced velocities observed in AKEP2020 and AKAN2020 models within the mantle wedge, particularly in the mantle or continental crust overriding the subducting slab exhibit seismic velocities similar to our saturated models in Figures 3.3 and 3.5. This is consistent with the hypothesis that the dehydration of the subducting crust has introduced a significant amount of hydration into the continental lithosphere. Within Alaska, the low angle of subduction has cut off mantle wedge convection in this area, and temperatures are too low to produce volcanism within the region of the Denali Gap (with the exception of the Buzzard Creek Maars volcanic field, shown in Figure 3.1), even with significant lithospheric hydration.

These results have important implications for flat-slab subduction zones. Overthickened aseismic ridges and oceanic plateaus like the Yakutat likely contain significant amounts of water, contributing to their buoyancy and subduction angle. As they subduct, they are hydrating the overriding mantle and continental crust. During ensuing slab rollback, the upwelling mantle could cause volcanic activity through interactions with the hydrated continental mantle and crust.

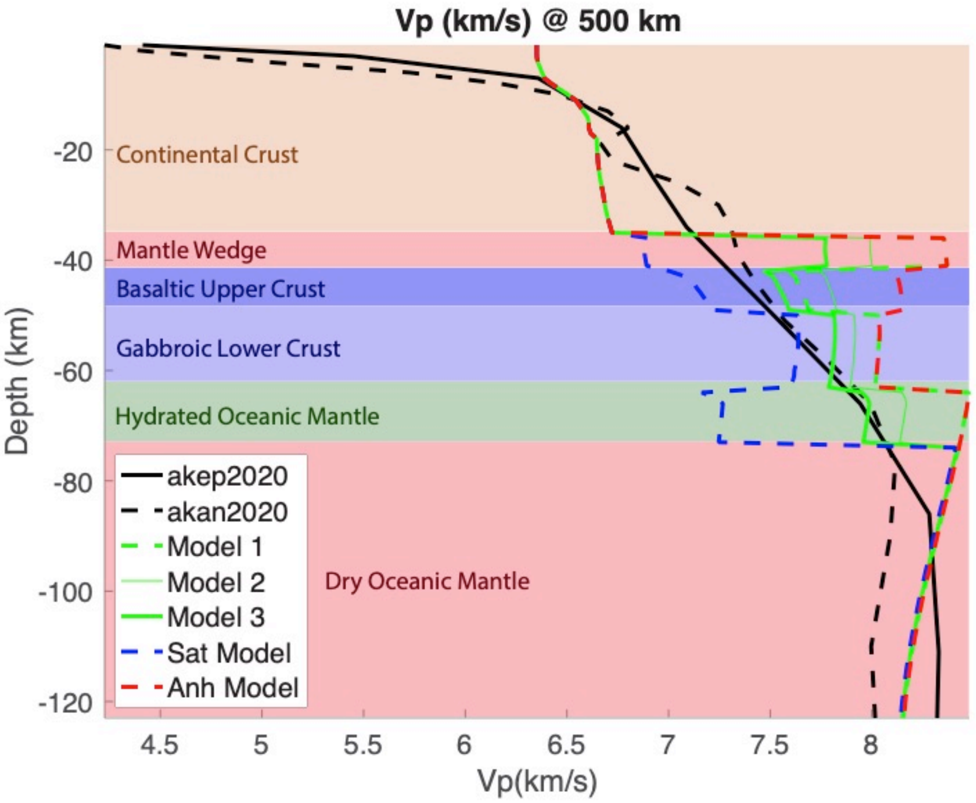
Vp (km/s) @ 500 km
Depth (km)
-20
-40
-60
-80
-100
-120
Continental Crust
Mantle Wedge
Basaltic Upper Crust
Gabbroic Lower Crust
Hydrated Oceanic Mantle
Dry Oceanic Mantle
akep2020
akan2020
Model 1
Model 2
Model 3
Sat Model
Anh Model
4.5
5
5.5
6
6.5
7
7.5
8
Vp(km/s)

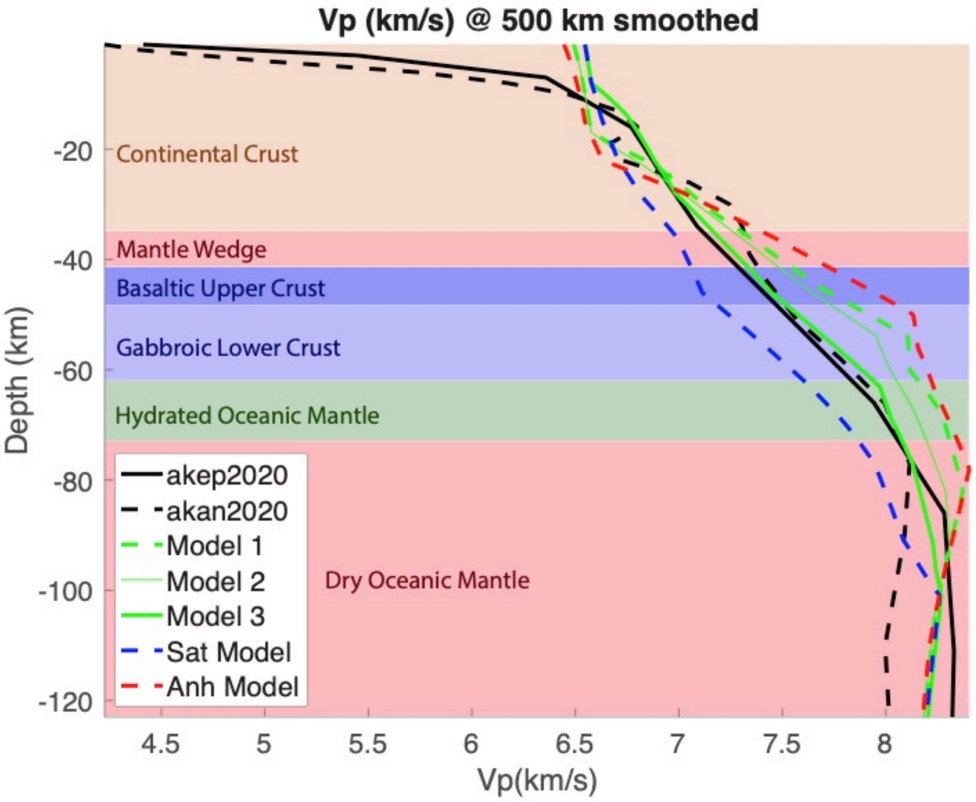
Vp (km/s) @ 500 km smoothed
Depth (km)
-20
-40
-60
-80
-100
-120
Continental Crust
Mantle Wedge
Basaltic Upper Crust
Gabbroic Lower Crust
Hydrated Oceanic Mantle
Dry Oceanic Mantle
akep2020
akan2020
Model 1
Model 2
Model 3
Sat Model
Anh Model
4.5
5
5.5
6
6.5
7
7.5
8
Vp(km/s)

Figure 3.9. P wave velocity versus depth, results taken at 500 km along the A-A' transect (Figure 3.1). Unsmoothed forward modeling results (top) alongside AKEP2020 (black solid line) and AKAN2020 (black dotted line). Smoothed forward modeling results (bottom) alongside AKEP2020 (black solid line) and AKAN2020 (black dotted line). Hybrid models 1-3 are plotted in green, saturated in blue, and anhydrous in red. The associated compositional layers are labeled and colored for clarity, continental crust (brown), mantle wedge (red), basaltic upper crust (dark blue), gabbroic lower crust (light blue), hydrated oceanic mantle (green), and dry oceanic mantle (red).

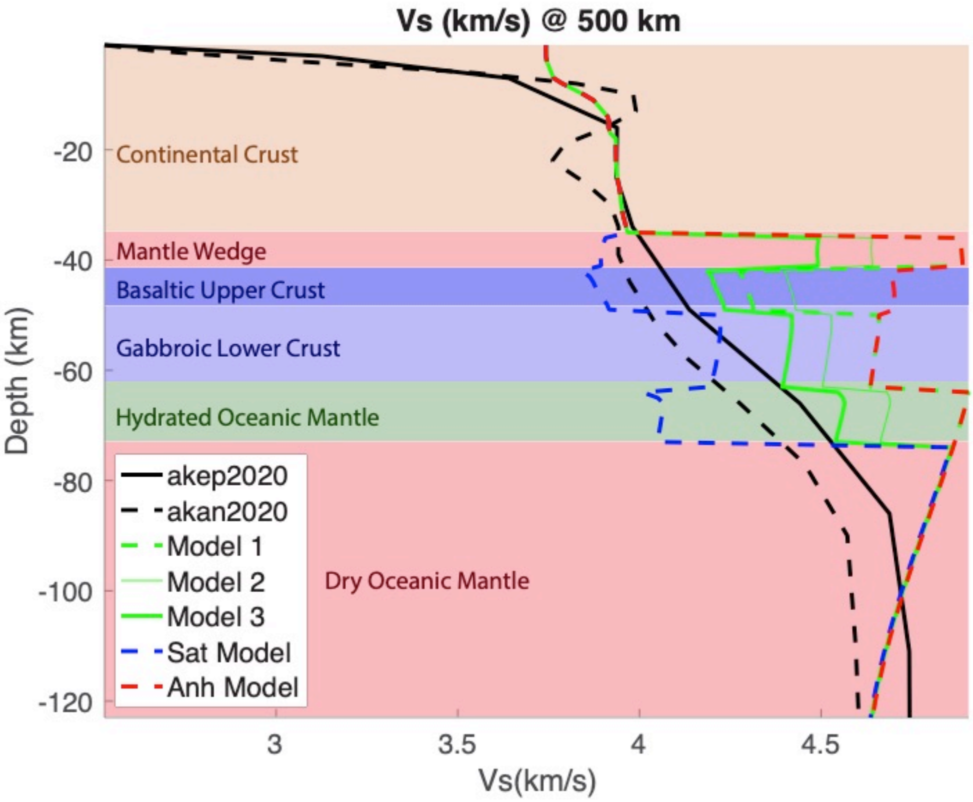
Vs (km/s) @ 500 km
Depth (km)
-20
-40
-60
-80
-100
-120
3
3.5
4
4.5
Vs(km/s)
Continental Crust
Mantle Wedge
Basaltic Upper Crust
Gabbroic Lower Crust
Hydrated Oceanic Mantle
Dry Oceanic Mantle
akep2020
akan2020
Model 1
Model 2
Model 3
Sat Model
Anh Model

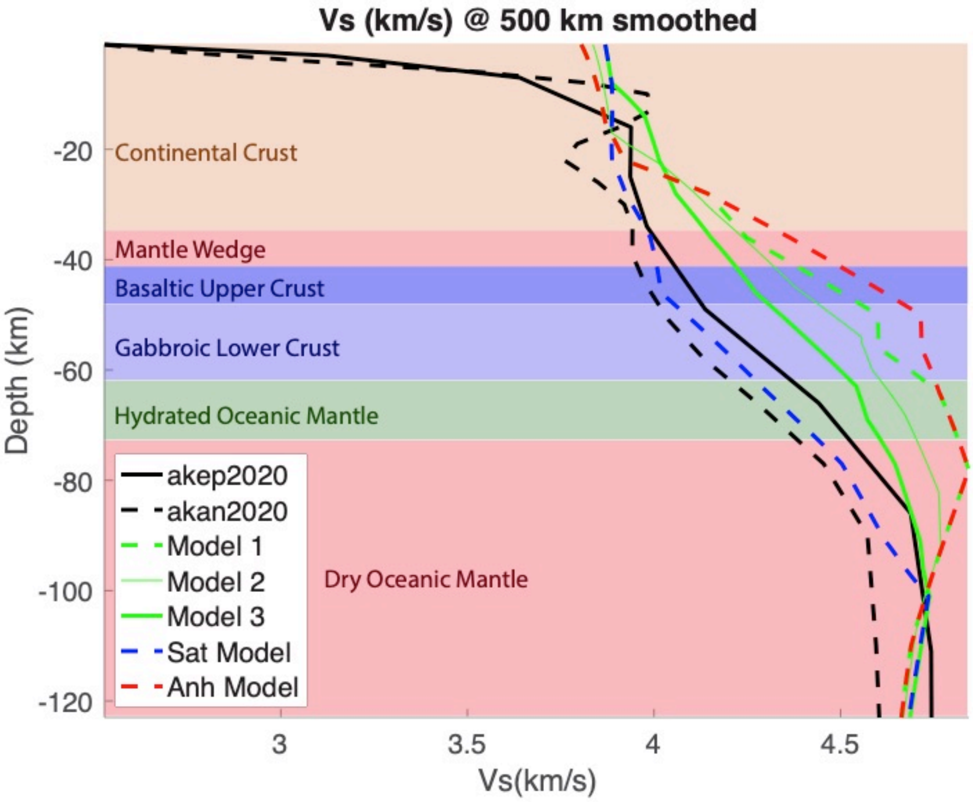
Vs (km/s) @ 500 km smoothed
Depth (km)
-20
-40
-60
-80
-100
-120
3
3.5
4
4.5
Vs(km/s)
Continental Crust
Mantle Wedge
Basaltic Upper Crust
Gabbroic Lower Crust
Hydrated Oceanic Mantle
Dry Oceanic Mantle
akep2020
akan2020
Model 1
Model 2
Model 3
Sat Model
Anh Model

Figure 3.10. S wave velocity versus depth, results taken at 500 km along the A-A' transect (Figure 3.1). Unsmoothed forward modeling results (top) alongside AKEP2020 (black solid line) and AKAN2020 (black dotted line). Smoothed forward modeling results (bottom) alongside AKEP2020 (black solid line) and AKAN2020 (black dotted line). Hybrid models 1-3 are plotted in green, saturated in blue, and anhydrous in red. The associated compositional layers are labeled and colored for clarity, continental crust (brown), mantle wedge (red), basaltic upper crust (dark blue), gabbroic lower crust (light blue), hydrated oceanic mantle (green), and dry oceanic mantle (red).

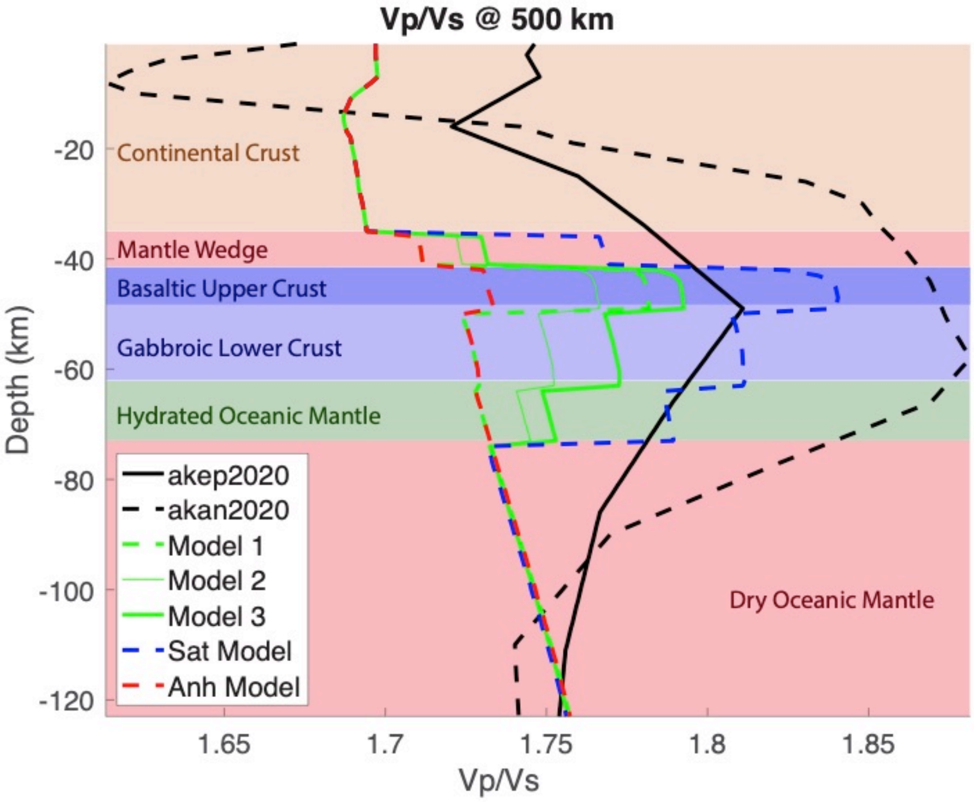
Vp/Vs @ 500 km
Continental Crust
Mantle Wedge
Basaltic Upper Crust
Gabbroic Lower Crust
Hydrated Oceanic Mantle
Dry Oceanic Mantle
akep2020
akan2020
Model 1
Model 2
Model 3
Sat Model
Anh Model
Depth (km)
-20
-40
-60
-80
-100
-120
1.65
1.7
1.75
1.8
1.85
Vp/Vs

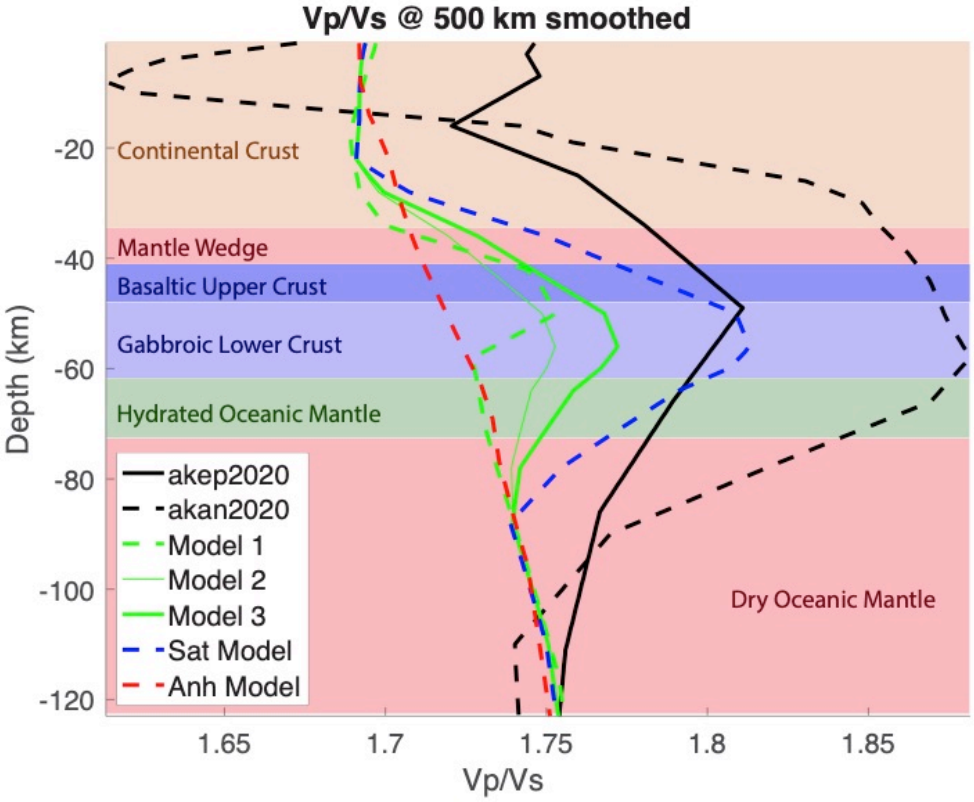
Vp/Vs @ 500 km smoothed
Continental Crust
Mantle Wedge
Basaltic Upper Crust
Gabbroic Lower Crust
Hydrated Oceanic Mantle
Dry Oceanic Mantle
akep2020
akan2020
Model 1
Model 2
Model 3
Sat Model
Anh Model
Depth (km)
-20
-40
-60
-80
-100
-120
1.65
1.7
1.75
1.8
1.85
Vp/Vs

Figure 3.11. Vp/Vs ratio versus depth, results taken at 500 km along the A-A' transect (Figure 3.1). Unsmoothed forward modeling results (top) alongside AKEP2020 (black solid line) and AKAN2020 (black dotted line). Smoothed forward modeling results (bottom) alongside AKEP2020 (black solid line) and AKAN2020 (black dotted line). Hybrid models 1-3 are plotted in green, saturated in blue, and anhydrous in red. The associated compositional layers are labeled and colored for clarity, continental crust (brown), mantle wedge (red), basaltic upper crust (dark blue), gabbroic lower crust (light blue), hydrated oceanic mantle (green), and dry oceanic mantle (red).

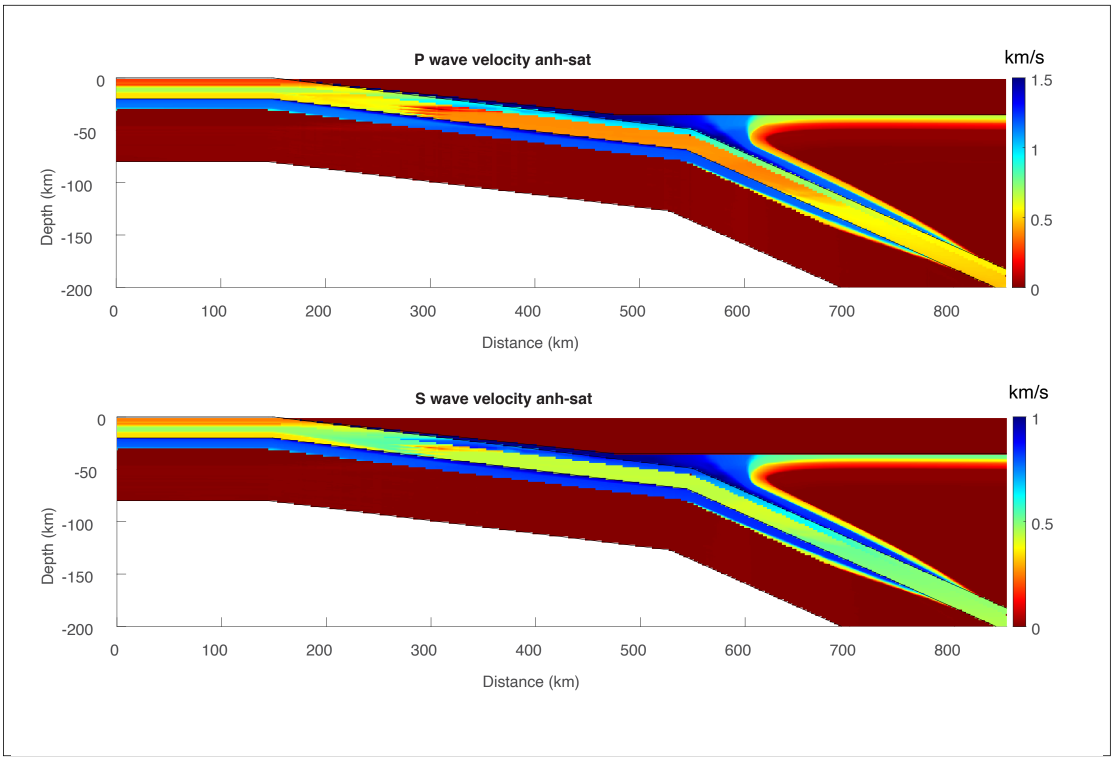

Figure 3.12. The difference between anhydrous and saturated modeled results for P wave velocity (upper panel) and S wave velocity (lower panel).

3.7 CONCLUSION

Constraining temperature and composition in the Alaskan flat-slab subduction region has allowed for calculations of seismic velocities with varying degrees of hydration. Our results are consistent with approximately 3% chemically bound H_2O within the subducting Alaskan flat-slab. When released from the subducting slab due to pressure and temperature increases, this water is likely incorporated into the overriding continental mantle and overriding continental crust, which would impact their mineralogy and rheology as well.

Using thermal and mineral phase equilibria forward modeling provides an opportunity to more accurately constrain the amount and location of hydration in subduction zone systems by constraining temperature, pressure, and composition which allows for the isolation of hydration effects on seismic velocity Our models indicate that hydration can reduce seismic velocities in the subducting crust by up to 0.6 km/s (P wave) or 0.5 km/s (S wave), and up to 1.5 km/s (P wave) or 1 km/s (S wave) in the subducting mantle. This allows for more informed interpretations of seismic tomography and has implications for other subduction systems where seismic data are available.

3.8 ACKNOWLEDGMENTS

This work was funded by NSF Awards EAR-1645227 and EAR-1829520. The IRIS Earth Model Collaboration (http://ds.iris.edu/ds/products/emc/) provided access to the seismic tomography models used in this study. IRIS Data Services are funded through NSF Cooperative Agreement EAR-1261681 titled Seismological Facilities for the Advancement of Geoscience and EarthScope (SAGE).

3.9 REFERENCES

Abers, G. A., & Hacker, B. R. (2016). A MATLAB toolbox and Excel workbook for calculating the densities, seismic wave speeds, and major element composition of minerals and rocks at pressure and temperature. Geochemistry, Geophysics, Geosystems, 17(2), 616-624.

Anderson, D. L., & Sammis, C. (1970). Partial melting in the upper mantle. Physics of the Earth and Planetary Interiors, 3, 41-50.

Argus, D. F., R. G. Gordon, M. B. Heflin, C. Ma, R. J. Eanes, P. Willis, W. R. Peltier, and S. E. Owen (2010), The angular velocities of the plates and the velocity of Earth's centre from space geodesy, Geophys. J. Int., 180(3), 913–960, doi:10.1111/j.1365-246X.2009.04463.x.

Bauer, M. A., Pavlis, G. L., and Landes, M. (2014). Subduction geometry of the Yakutat terrane, southeastern Alaska. Geosphere, 10(6), 1161-1176.

Berg, E. M., Lin, F. C., Allam, A., Schulte-Pelkum, V., Ward, K. M., & Shen, W. (2020). Shear Velocity Model of Alaska Via Joint Inversion of Rayleigh Wave Ellipticity, Phase Velocities, and Receiver Functions Across the Alaska Transportable Array. Journal of Geophysical Research: Solid Earth, 125(2), e2019JB018582.

Bina, C. R., & Helffrich, G. R. (1992). Calculation of elastic properties from thermodynamic equation of state principles. Annual Review of Earth and Planetary Sciences, 20(1), 527-552.

Bruns, T. R. (1983). Model for the origin of the Yakutat block, an accreting terrane in the northern Gulf of Alaska. Geology, 11(12), 718-721.

Carlson, R. L. (2014). The effects of alteration and porosity on seismic velocities in oceanic basalts and diabases. Geochemistry, Geophysics, Geosystems, 15(12), 4589-4598.

Christensen, N. I. (1996). Poisson's ratio and crustal seismology. Journal of Geophysical Research: Solid Earth, 101(B2), 3139-3156.

Christeson, G. L., Gulick, S. P., van Avendonk, H. J., Worthington, L. L., Reece, R. S., and Pavlis, T. L. (2010). The Yakutat terrane: Dramatic change in crustal thickness across the Transition fault, Alaska. Geology, 38(10), 895-898.

Connolly, J. A. (2005). Computation of phase equilibria by linear programming: a tool for geodynamic modeling and its application to subduction zone decarbonation. Earth and Planetary Science Letters, 236(1-2), 524-541.

Davis, A. S., and Plafker, G. (1986). Eocene basalts from the Yakutat terrane: Evidence for the origin of an accreting terrane in southern Alaska. Geology, 14(11), 963-966.

Dunn, R. A., & Forsyth, D. W. (2003). Imaging the transition between the region of mantle melt generation and the crustal magma chamber beneath the southern East Pacific Rise with short-period Love waves. Journal of Geophysical Research: Solid Earth, 108(B7).

Eberhart-Phillips, D. (1990). Three-dimensional P and S velocity structure in the Coalinga region, California. Journal of Geophysical Research: Solid Earth, 95(B10), 15343-15363.

Eberhart-Phillips, D., Christensen, D. H., Brocher, T. M., Hansen, R., Ruppert, N. A., Haeussler, P. J., and Abers, G. A. (2006). Imaging the transition from Aleutian subduction to Yakutat collision in central Alaska, with local earthquakes and active source data. Journal of Geophysical Research: Solid Earth, 111(B11).

Eberhart-Phillips, D., & Fry, B. (2017). A new scheme for joint surface wave and earthquake travel-time inversion and resulting 3-D velocity model for the western North Island, New Zealand. Physics of the Earth and Planetary Interiors, 269, 98-111.

Eberhart-Phillips, D., A. Nayak, N. Ruppert, and C. Thurber (2020), Alaska 2020 update for USGS G19AP00019: Initial Development of Alaska Community Seismic Velocity Models, https://zenodo.org/record/3727244.

Elliott, J. L., Larsen, C. F., Freymueller, J. T., and Motyka, R. J. (2010). Tectonic block motion and glacial isostatic adjustment in southeast Alaska and adjacent Canada constrained by GPS measurements. Journal of Geophysical Research: Solid Earth, 115(B9).

English, J. M., Johnston, S. T., & Wang, K. (2003). Thermal modelling of the Laramide orogeny: testing the flat-slab subduction hypothesis. Earth and Planetary Science Letters, 214(3-4), 619–632. https://doi.org/10.1016/s0012-821x(03)00399-6

Fang, H., Zhang, H., Yao, H., Allam, A., Zigone, D., Ben-Zion, Y., ... & van der Hilst, R. D. (2016). A new algorithm for three-dimensional joint inversion of body wave and surface wave data and its application to the Southern California plate boundary region. Journal of Geophysical Research: Solid Earth, 121(5), 3557-3569.

Feng, L., & Ritzwoller, M. H. (2019). A 3-D shear velocity model of the crust and uppermost mantle beneath Alaska including apparent radial anisotropy. Journal of Geophysical Research: Solid Earth, 124(10), 10468-10497.

Gale, A., Dalton, C. A., Langmuir, C. H., Su, Y., and Schilling, J. G. (2013). The mean composition of ocean ridge basalts. Geochemistry, Geophysics, Geosystems, 14(3), 489-518.

Gardner, T.W., Fisher, D.M., Morell, K.D., and Cupper, M.L., (2013), Upper-plate deformation in response to flat slab subduction inboard of the aseismic Cocos Ridge, Osa Peninsula, Costa Rica: Lithosphere, v. 5, no. 3, p. 247–264, doi: 10.1130/L251.1.

Gutscher, M.-A.A., Maury, R., Eissen, J.P., and Bourdon, E., (2000), Can slab melting be caused by flat subduction?: Geology, v. 28, no. 6, p. 535, doi: 10.1130/0091-7613(2000)28<535:CSMBCB>2.0.CO;2.

Gutscher, M.A. (2002), Andean subduction styles and their effect on thermal structure and interplate coupling: Journal of South American Earth Sciences, v. 15, no. 1, p. 3–10, doi: 10.1016/S0895-9811(02)00002-0.

Gueguen, Y., & Mercier, J. M. (1973). High attenuation and the low-velocity zone. Physics of the Earth and Planetary Interiors, 7(1), 39-46.

Hacker, B. R., Abers, G. A., & Peacock, S. M. (2003). Subduction factory 1. Theoretical mineralogy, densities, seismic wave speeds, and H2O contents. Journal of Geophysical Research: Solid Earth, 108(B1).

Hacker, B. R., & Abers, G. A. (2004). Subduction Factory 3: An Excel worksheet and macro for calculating the densities, seismic wave speeds, and H2O contents of minerals and rocks at pressure and temperature. Geochemistry, Geophysics, Geosystems, 5(1).

Hammond, W. C., & Humphreys, E. D. (2000). Upper mantle seismic wave velocity: Effects of realistic partial melt geometries. Journal of Geophysical Research: Solid Earth, 105(B5), 10975-10986.

Han, T., Gurevich, B., Fu, L. Y., Qi, Q., Wei, J., & Chen, X. (2020). Combined effects of pressure and water saturation on the seismic anisotropy in artificial porous sandstone with aligned fractures. Journal of Geophysical Research: Solid Earth, 125(1), e2019JB019091.

Hekinian, R. (2000). Petrology of the ocean floor (Vol. 33). Elsevier, p. 333-359.

Hernández-Uribe, D., & Palin, R. M. (2019). A revised petrological model for subducted oceanic crust: Insights from phase equilibrium modelling. Journal of Metamorphic Geology, 37(6), 745-768.

Hori, S., Inoue, H., Fukao, Y., & Ukawa, M. (1985). Seismic detection of the untransformed 'basaltic' oceanic crust subducting into the mantle. Geophysical Journal International, 83(1), 169-197.

Humphreys, E. D. (1995). Post-Laramide removal of the Farallon slab, western United States. Geology, 23(11), 987-990.

Hyndman, R. D., & Peacock, S. M. (2003). Serpentinization of the forearc mantle. Earth and Planetary Science Letters, 212(3-4), 417-432.

IRIS DMC (2011). Data Services Products: EMC, A repository of Earth models, https://doi.org/10.17611/DP/EMC.1.

Jischke, M.C., (1975), On the dynamics of descending lithospheric plates and slip zones: Journal of Geophysical Research-Solid Earth and Planets, v. 80, no. 35, p. 4809–4813, doi: 10.1029/JB080i035p04809.

Karato, S. I. (1986). Does partial melting reduce the creep strength of the upper mantle?. Nature, 319(6051), 309-310.

Karato, S. I., & Jung, H. (1998). Water, partial melting and the origin of the seismic low velocity and high attenuation zone in the upper mantle. Earth and Planetary Science Letters, 157(3-4), 193-207.

Knezevic Antonijevic, S., Wagner, L.S., Kumar, A., Beck, S.L., Long, M.D., Zandt, G., Tavera, H., and Condori, C., (2015), The role of ridges in the formation and longevity of flat slabs: Nature, v. 524, no. 7564, p. 212–215, doi: 10.1038/nature14648.

Kumar, P., and Kawakatsu, H. (2011). Imaging the seismic lithosphere-asthenosphere boundary of the oceanic plate. Geochemistry, Geophysics, Geosystems, 12(1).

Ma, Y., and Clayton, R.W., (2015), Flat slab deformation caused by interplate suction force: Geophysical Research Letters, v. 42, p. 1–9, doi: 10.1002/(ISSN)1944-8007.

Manea, V.C., PÈrez-GussinyÈ, M., and Manea, M., (2011), Chilean flat slab subduction controlled by overriding plate thickness and trench rollback: Geology, v. 40, no. 1, p. 35–38, doi: 10.1130/G32543.1.

Mankhemthong, N., Doser, D. I., and Pavlis, T. L. (2013). Interpretation of gravity and magnetic data and development of two-dimensional cross-sectional models for the Border Ranges fault system, south-central Alaska. Geosphere, 9(2), 242-259.

Marot, M., Monfret, T., Gerbault, M., Nolet, G., Ranalli, G., & Pardo, M. (2014). Flat versus normal subduction zones: a comparison based on 3-D regional traveltime tomography and petrological modelling of central Chile and western Argentina (29–35 S). Geophysical Journal International, 199(3), 1633-1654.

Martin-Short, R., Allen, R. M., and Bastow, I. D. (2016). Subduction geometry beneath south central Alaska and its relationship to volcanism. Geophysical Research Letters, 43(18), 9509-9517.

Martin-Short, R., Allen, R., Bastow, I. D., Porritt, R. W., & Miller, M. S. (2018). Seismic imaging of the Alaska subduction zone: Implications for slab geometry and volcanism. Geochemistry, Geophysics, Geosystems, 19(11), 4541-4560.

Minster, J. B., & Anderson, D. L. (1981). A model of dislocation-controlled rheology for the mantle. Philosophical Transactions of the Royal Society of London. Series A, Mathematical and Physical Sciences, 299(1449), 319-356.

Nye, C. (1999). The Denali volcanic gap—Magmatism at the eastern end of the Aleutian arc. Eos Trans. AGU, 80, 46.

O'Driscoll, L.J., Humphreys, E.D., and Saucier, F., (2009), Subduction adjacent to deep continental roots: Enhanced negative pressure in the mantle wedge, mountain building and continental motion: Earth and Planetary Science Letters, v. 280, no. 1-4, p. 61–70, doi: 10.1016/j.epsl.2009.01.020.

O'Driscoll, L. J., and Miller, M. S. (2015). Lithospheric discontinuity structure in Alaska, thickness variations determined by Sp receiver functions. Tectonics, 34(4), 694-714.

Park, J., & Rye, D. M. (2019). Broader impacts of the metasomatic underplating hypothesis. Geochemistry, Geophysics, Geosystems, 20(11), 4810-4829.

Peacock, S. M. (1993). Large-scale hydration of the lithosphere above subducting slabs. Chemical Geology, 108(1-4), 49-59.

Petersen, S. E., Hoisch, T. D., & Porter, R. C. (2021). Assessing the Role of Water in Alaskan Flat-Slab Subduction. Geochemistry, Geophysics, Geosystems, 22, e2021GC009734. https://doi.org/10.1029/2021GC009734

Pilger, R. H., Jr (1981). Plate reconstructions, aseismic ridges, and low-angle subduction beneath the Andes. The Geological Society of America Bulletin, 92(7), 448. https://doi.org/10.1130/0016-7606(1981)92<448:PRARAL>2.0.CO;2.10.1130/0016-7606(1981)92<448:praral>2.0.co;2

Plafker, G., & Berg, H. C. (1994). Overview of the geology and tectonic evolution of Alaska. In Plafker, G. & Bergs, H.C. (Eds.), The Geology of North America, The Geology of Alaska (Vol. G-1, pp. 989–1021). Boulder, CO, Geological Society of America.

Plattner, C., Malservisi, R., Dixon, T. H., LaFemina, P., Sella, G. F., Fletcher, J., and Suarez-Vidal, F. (2007). New constraints on relative motion between the Pacific plate and Baja California microplate (Mexico) from GPS measurements. Geophysical Journal International, 170(3), 1373-1380.

Porter, R., Gilbert, H., Zandt, G., Beck, S., Warren, L., Calkins, J., Alvarado, P., and Anderson, M., (2012), Shear wave velocities in the Pampean flat-slab region from Rayleigh wave tomography: Implications for slab and upper mantle hydration: Journal of Geophysical Research-Solid Earth and Planets, v. 117, no. B11, p. B11301, doi: 10.1029/2012JB009350.

Porter, R. C., van der Lee, S., & Whitmeyer, S. J. (2019). Synthesizing EarthScope data to constrain the thermal evolution of the continental US lithosphere. Geosphere, 15(6), 1722-1737.

Ramos, V.A., and Folguera, A., (2009), Andean flat-slab subduction through time: Geological Society, London, Special Publications, v. 327, no. 1, p. 31, doi: 10.1144/SP327.3.

Rioux, M., Mattinson, J., Hacker, B., Kelemen, P., Blusztajn, J., Hanghøj, K., and Gehrels, G. (2010). Intermediate to felsic middle crust in the accreted Talkeetna arc, the Alaska Peninsula and Kodiak Island, Alaska: An analogue for low-velocity middle crust in modern arcs. Tectonics, 29(3).

Rossi, G., Abers, G. A., Rondenay, S., & Christensen, D. H. (2006). Unusual mantle Poisson's ratio, subduction, and crustal structure in central Alaska. Journal of Geophysical Research: Solid Earth, 111(B9).

Rudnick, R. L., and Gao, S. (2003). Composition of the continental crust. Treatise on geochemistry, 3, 659.

Schutt, D. L., & Dueker, K. (2008). Temperature of the plume layer beneath the Yellowstone hotspot. Geology, 36(8), 623-626.

Skinner, S.M., and Clayton, R.W., (2010), An Evaluation of Proposed Mechanisms of Slab Flattening in Central Mexico: Pure and applied geophysics,, p. 1–14, doi: 10.1007/s00024-010-0200-3.

Stevenson, D.J., and Turner, J.S., (1977), Angle of subduction: Nature, v. 270, p. 334–336, doi: 10.1038/270334a0.

Thurber, C., Ritsema, J., Romanowicz, B., & Dziewonski, A. (2015). Seismic tomography and inverse methods. Deep Earth Seismology, 307-337.

Usui, T., Nakamura, E., Kobayashi, K., Maruyama, S., & Helmstaedt, H. (2003). Fate of the subducted Farallon plate inferred from eclogite xenoliths in the Colorado Plateau. Geology, 31(7), 589-592.

van der Lee, S. (2002). High-resolution estimates of lithospheric thickness from Missouri to Massachusetts, USA. Earth and Planetary Science Letters, 203(1), 15-23.

van Hunen, J., van den Berg, A. P., & Vlaar, N. J. (2000). A thermo-mechanical model of horizontal subduction below an overriding plate. Earth and Planetary

Science Letters, 182(2), 157–169. https://doi.org/10.1016/s0012-821x(00)00240-5

van Hunen, J., van den Berg, A. P., & Vlaar, N. J. (2002). On the role of subducting oceanic plateaus in the development of shallow flat subduction. Tectonophysics, 352(3-4), 317–333. https://doi.org/10.1016/s0040-1951(02)00263-9

van Keken, P. E., Currie, C., King, S. D., Behn, M. D., Cagnioncle, A., He, J., Katz, R.F., Lin, S.-C, Spiegelman, M. and Wang, K. (2008). A community benchmark for subduction zone modeling. Physics of the Earth and Planetary Interiors, 171(1-4), 187-197.

van Keken, P. E., Hacker, B. R., Syracuse, E. M., & Abers, G. A. (2011). Subduction factory: 4. Depth-dependent flux of H2O from subducting slabs worldwide. Journal of Geophysical Research: Solid Earth, 116(B1).

Veenstra, E., Christensen, D. H., Abers, G. A., and Ferris, A. (2006). Crustal thickness variation in south-central Alaska. Geology, 34(9), 781-784.

Wagner, L.S., Walter, M.J., Lin, Y., and Foustoukos, D.I. (December 10, 2019). The effects of hydration and silica enrichment on the seismic velocity structure of the continental mantle lithosphere [Conference Presentation Abstract]. American Geophysical Union Fall Meeting 2019, San Francisco, CA. https://agu.confex.com/agu/fm19/meetingapp.cgi/Paper/489192

Wang, Y., and Tape, C. (2014). Seismic velocity structure and anisotropy of the Alaska subduction zone based on surface wave tomography. Journal of Geophysical Research: Solid Earth, 119(12), 8845-8865.

Ward, K. M. (2015). Ambient noise tomography across the southern Alaskan cordillera. Geophysical Research Letters, 42(9), 3218-3227.

Ward, K. M., & Lin, F.-C. (2018). Lithospheric structure across the Alaskan cordillera from the joint inversion of surface waves and receiver functions. Journal of Geophysical Research: Solid Earth, 123, 8780– 8797. https://doi.org/10.1029/2018JB015967

Watkins, W. D., Thurber, C. H., Abbott, E. R., & Brudzinski, M. R. (2018). Local earthquake tomography of the Jalisco, Mexico region. Tectonophysics, 724, 51-64.

Wells, R., Bukry, D., Friedman, R., Pyle, D., Duncan, R., Haeussler, P., and Wooden, J. (2014). Geologic history of Siletzia, a large igneous province in the Oregon and Washington Coast Range: Correlation to the geomagnetic polarity time scale and implications for a long-lived Yellowstone hotspot. Geosphere, 10(4), 692-719.

Worthington, L. L., Van Avendonk, H. J., Gulick, S. P., Christeson, G. L., and Pavlis, T. L. (2012). Crustal structure of the Yakutat terrane and the evolution of subduction and collision in southern Alaska. Journal of Geophysical Research: Solid Earth, 117(B1).

CHAPTER 4: THE COLORADO PLATEAU AND BASIN AND RANGE PROVINCE: A STUDY OF ISOSTATIC RESPONSE AND UPLIFT

Authors: Petersen, S.E., and Porter, R.C.

4.1 ABSTRACT

The Colorado Plateau is a high (~2 km), relatively-undeformed block within the North American Cordillera that was located at sea level during the late Cretaceous. Given its tectonic quiescence, the mechanisms for plateau uplift are not well understood. Quantifying the isostatic state of the Colorado Plateau can provide insight into the factors that contribute to its modern high surface elevation. To do this, we integrate several large datasets to accurately represent its thermal state, composition, and degree of hydration, all of which contribute to lithospheric densities. These datasets include seismic, heat flux, climate, crustal compositional, and topographical data. We use these data to calculate densities for the Colorado Plateau and the adjacent Great Basin Province and Southern Basin and Range Provinces. Densities are calculated using estimates of sediment thickness and metamorphic phase equilibria calculations for the lower crust and upper mantle. We also quantify the maximum amount of isostatic uplift that can be attributed to hydration of the lower crust of the Colorado Plateau based on our phase equilibria modelling. Results indicate that the interior of the Colorado Plateau is supported isostatically, while the margin of the CP and adjacent Great Basin Province and Southern Basin and Range Province are supported by density variations below the bottom of our model or dynamic forces such as small-scale upper mantle convection. Hydration of the lower crust can potentially support up to to 1600 meters of uplift in the interior of the Colorado Plateau, but cannot account for the high elevations observed on the southern and western margins of the Colorado Plateau.

4.2 INTRODUCTION

The Colorado Plateau (CP) is a physiographic province located in the southwestern United States. The region is unique in that it has uplifted to its current elevation (~2 km) with little internal deformation (~1% shortening) (Davis, 1978). The CP is located between the basement-involved uplifts of the Rocky Mountains to the east and the extensional province of the Basin and Range to the west and south (Figure 4.1). The timing and mechanism for uplift for the Colorado Plateau remain enigmatic and have been a matter of substantial debate (e.g. Flowers et al., 2010 and references therein). Previous studies have hypothesized numerous mechanisms to explain the modern surface elevation of the Colorado Plateau (CP), many of which are not mutually exclusive. These include crustal thickening due to channelized mid-crustal flow (i.e. McQuarrie and Chase, 2000), convective removal of lithospheric mantle (Bird, 1979; England and Houseman, 1988), chemical modification of the lithosphere by volatile addition (Humphreys et al., 2003), lithospheric delamination and subsequent asthenospheric upwelling (Spencer, 1996), melt extraction followed by heating along plateau margins (Roy et al., 2004), lower-crustal hydration associated with Laramide subduction (Jones et al., 2015; Levandowski et al., 2018), and various combinations of these (Porter et al., 2017). While the timing and mechanisms by which the Colorado Plateau has undergone uplift are debated, many researchers are coming to the consensus that the uplift has happened in a few stages since Late Cretaceous time (Pederson et al., 2002) and involved little to no internal deformation of the Colorado Plateau lithosphere (i.e. Davis, 1978; Morgan and Swanberg, 1985; Spencer, 1996; Gilbert et al., 2003).

Questions remain about the timing and mechanisms for CP uplift. How is the current elevation of the CP being sustained? Is the high topography of the CP due to dynamic forces or isostatic support? Is it a region-wide phenomena, or are smaller and more localized factors at work? How much uplift can be attributed to different processes? When did uplift occur?

Here we present new density models of the CP calculated by integrating several recent datasets in order to evaluate the isostatic state of the CP relative to the adjacent Southern Basin and Range Province (SBRP) and Great Basin Province (GBP). We also estimate the isostatic effects of hydrating an initially anhydrous Colorado Plateau lithosphere. While other studies have attempted to determine the isostatic response of the CP (i.e. Chase et al., 2002; Pederson et al., 2002, Levandowski et al., 2018), we use more recent datasets designed to better understand lower-crustal mineralogy in order to more accurately calculate lithospheric density. These include estimates of crustal thickness, sediment thickness, and mantle temperatures, which are combined in order to create a complete isostatic model of the Colorado Plateau and the adjacent SBRP and GB. We incorporate mineral phase equilibria calculations of the lower crust and upper mantle, seismic data, and heat flow data to explore where hydrous phases are stable and estimate densities for the crust and upper mantle in order to determine if the Colorado Plateau is in isostatic equilibrium with the surrounding regions.

4.3 GEOLOGIC SETTING

The Colorado Plateau has a surface elevation of ~2 km above sea level, is slightly bowl-shaped, and is located adjacent to the SBRP that lies to the south, and the extending GBP to the west. The CP is also bounded by the Rio Grande Rift to the east, the Rocky Mountains to the northeast, and the Wyoming Province to the north. The crust of the CP is 30-40 km thick, and has experienced little to no internal deformation or significant crustal shortening (Davis, 1978; Morgan and Swanberg, 1985; Spencer, 1996; Flowers et al., 2010). While the interior of the CP has only experienced small-volume volcanism, including the Navajo Volcanic Field near the Four Corners Region and laccolith emplacements, the CP margin contains several recent volcanic centers (see Figure 4.1) whose eruptions concentrate from ~30 Ma to modern. Recent geophysical and geologic studies have shown that deformation and volcanism are impinging on Colorado Plateau lithosphere and migrating inward from the plateau margins (Sine et al., 2008; Roy et al., 2009; Crow et al., 2011)

Surface uplift of the Colorado Plateau is likely a response to both dynamic and isostatic support. Dynamic support involves an applied normal force from below - such as asthenospheric upwelling. Isostatic support involves crustal composition changes, crustal thickening, changes to the hydration state, or other factors that result in a decrease in lithospheric density (Levandowski et al., 2018). In this study we include thermal perturbations (i.e. thermal expansion) in our isostatic calculations. Previous authors have varied in their interpretation of warming and attributed it to both dynamic and isostatic effects (e.g. Molnar and England, 1990; Pederson et al., 2002; Jones et al., 2015). Isostatic support can also involve lithospheric mantle changes that decrease density, including advective or conductive heating, chemical changes such as depletion, or phase changes (McGetchin et al., 1980; Morgan and Swanberg, 1985).

The timing of CP uplift is not well constrained. The only certainty is that the CP was at sea level during the Cretaceous, and uplift to its current elevation has occurred since this time. The evidence for this is the presence of Cretaceous-age marine rocks exposed on the CP surface. Hypotheses for early uplift of the plateau (~80-40 Ma) primarily associate uplift with processes relating to Laramide flat-slab subduction (i.e. Humphreys et al., 2003), and rollback of the Farallon slab (40-20 Ma) following low-angle subduction (Flowers et al., 2008). Late-Tertiary uplift models of the CP (post-20 Ma) invoke mechanisms that include deep and/or shallow mantle convective processes, lithospheric delamination, heating due to the extension of the adjacent Basin and Range Province, and others (Bird, 1979; Thompson and Zoback, 1979, Parsons and McCarthy, 1995; Flowers et al., 2008; Roy et al., 2009; Porter et al., 2017).

During the subduction of the Farallon slab in Laramide time, it is hypothesized that dewatering of the slab hydrated the lithosphere of the Colorado Plateau and surrounding regions, which impacted their density structures (Humphreys et al., 2003; Jones et al., 2015; Schulze et al., 2015; Porter et al., 2017). This hypothesis is supported by isotope analysis of hydrated peridotite xenoliths in the Navajo volcanic field located near the center of the CP in the Four Corners Region (Usui et al., 2003; Smith et al., 2004; Smith et al., 2010; Schulze et al., 2015). Following flat-slab subduction the Farallon slab is thought to have “rolled-back” into a more-typical subduction geometry. During this process, hot asthenosphere is thought to have upwelled into the space vacated by the flat slab. This influx of material up to the base of the previously refrigerated and hydrated North American lithosphere is thought to have caused a time-transgressive sweep of volcanism, often referred to as the “ignimbrite flare-up” (Coney, 1978). While the surrounding regions experienced wide-spread volcanism the plateau itself experienced little to no volcanic activity, with the exception of the Navajo Volcanic Field near the Four Corners Region and laccolith emplacement (Schulze et al., 2015). Given the dearth of volcanism in the CP interior, it is possible that these slab-derived volatiles were incorporated into hydrous mineral phases that were stable due to refrigeration of the overriding lithosphere by the slab (Humphreys et al., 2003; Jones et al., 2015; Porter et al., 2017). If this is correct and the CP lithosphere remained relatively cold, the hydration in the lower lithosphere of the CP was likely retained. As hydrous mineral assemblages such as amphiboles and micas are less dense than anhydrous phases stable at similar PT conditions (i.e. Peacock et al., 1993; Porter et al., 2017), this could provide a mechanism for uplifting the plateau to its present elevation.

Additionally, it is possible that the Farallon slab could have remained intact underneath the CP, which could explain the lack of volcanism in the CP relative to the surrounding regions. When a slab underplates the continental lithosphere, it is referred to as “slab-stacking”, and has been suggested by Humphreys et al. (2015) to have occurred in the Wyoming region during Farallon flat-slab subduction. In Wyoming, the observed cool temperatures and fast seismic velocities observed to depths of 230-300 km is thought to be the result of this phenomena (Humphreys et al., 2015). We would expect that if Farallon slab-stacking occurred in the CP, we would find similar low-temperature and high-velocity signatures to similar depths beneath the CP.

Following volcanism, the adjacent Southern Basin and Range Province and Great Basin Province experienced large-magnitude extension that formed the modern Basin and Range topography. Tertiary extension and related warming in the SBRP and GBP thinned the lithosphere in both regions up to the margins of the CP. This resulted in a large 5-10 km “step” between the thinner lithosphere of the SBRP/GBP and the thicker lithosphere of the CP (Levander et al., 2011).

It is theorized that the existence of this lithospheric step has resulted in an adiabatic upwelling of the underlying undepleted mantle, causing thermochemical erosion along the margins of the CP (Levander et al., 2011). Migrating extension towards the interior of the CP may be driving small-scale convection in the upper mantle, where we observe young (<1 Ma) volcanism and deformation in the Colorado Plateau margins (Sine et al., 2008; Van Wijk et al., 2010; Reid et al., 2012).

Geological evidence indicates that the crust of the Colorado Plateau has remained stable for several hundred million years, which precludes shortening as a mechanism for uplift. This is consistent with the idea that the sustained high elevation of the Plateau is at least partially supported by warming and hydration-induced retrogression of the lower crust by both Farallon slab-derived fluids, and the accumulation of sediments during the Cretaceous and Early Tertiary (Flowers et al., 2008; Porter et al., 2017; Levandowski et al., 2018). However, these isostatic support mechanisms may not be sufficient to completely explain the high elevation of the modern CP. Recent work has shown that ~290 m of isostatically supported uplift can be attributed to hydration of the lower crust (Porter et al., 2017). Sedimentation during the Cretaceous may have contributed ~250 m of relative uplift (Levandowski et al., 2018). Warming the lower crust could also provide additional uplift primarily along the plateau margins where low seismic velocities are observed in the upper mantle (Porter et al., 2017). In order to explain the entirety of the 1.6-2 km of CP elevation, it is possible that dynamic mechanisms, such as small-scale convection, need to be invoked to fully explain the modern surface elevations.

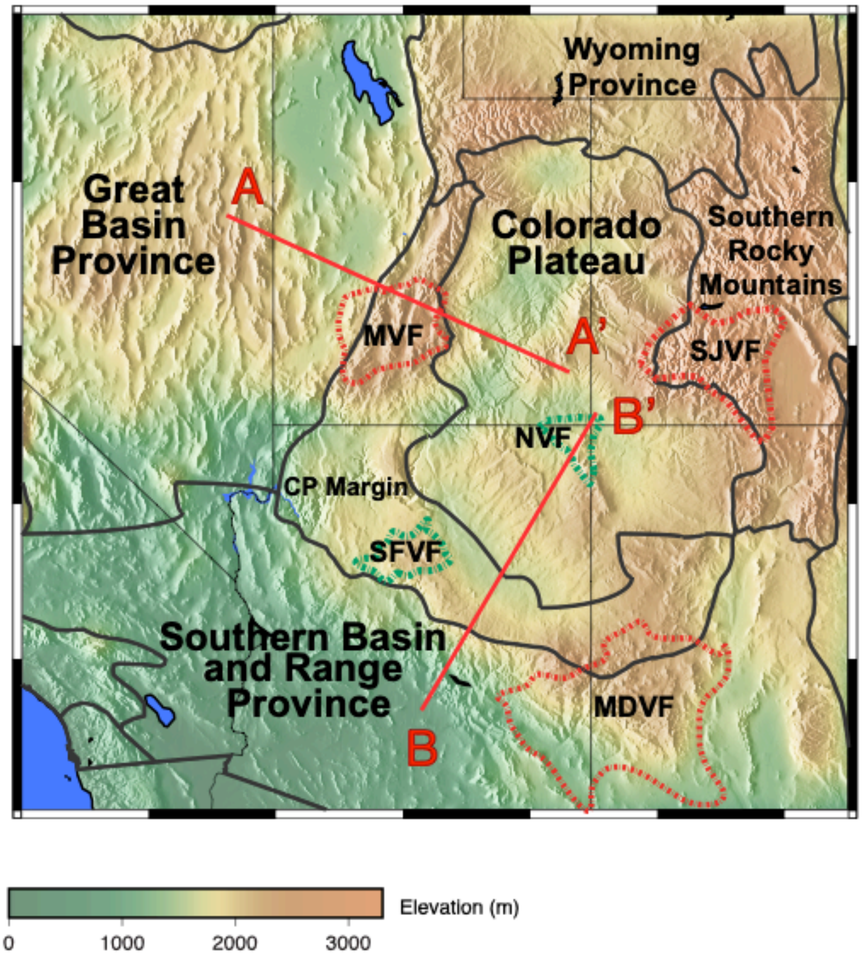

Figure 4.1. Map of the study region and locations of A-A' and B-B' cross sections. The topography is low-pass filtered, and gray lines show the outlines of major provinces. Red and green outlines indicate recent volcanic centers. MVF = Marysvale Volcanic Field, SJVF = San Juan Volcanic Field, NVF = Navajo Volcanic Field, SFVF = San Francisco Volcanic Field, MDVF = Mogollon-Datil Volcanic Field.

4.4 METHODS

4.4.1 Data and Methods Overview

To evaluate the isostatic state of the modern Colorado Plateau relative to the Basin and Range Province and the Great Basin Province and to an initially anhydrous plateau, we integrate several datasets to calculate 3D models of density across each province. First, thermal conditions for the lithosphere are estimated using surface temperatures (PRISM Climate Group, 2018), Moho temperatures (Schutt et al., 2018), crustal thickness estimates (Buehler and Shearer, 2016), LAB depth and temperatures from Porter and Reid (2021), and heat flow data from the International Heat Flow Commission (IHFC database, www.https://ihfc-iugg.org). While Buehler and Shearer (2016) may not provide the most accurate crustal thickness estimates available, these values were chosen for consistency with temperature data as their results were input in Schutt et al.'s (2018) Moho temperature calculations. Next, we combine estimates of major oxide chemistries (Condie and Selverstone, 1999) with temperature and pressure calculations to predict stable mineral assemblages and associated densities. Finally, we define layers and layer thicknesses using Precambrian basement depths for sediment (Marshak et al., 2017), topography data from the Global Multi-Resolution Topography Data Synthesis (Carbotte et al., 2009), Moho depths (Buehler and Shearer, 2016), and LAB depths (Porter and Reid, 2021).

We calculated pressures at the compensation depths using three separate density models. We selected a compensation depth of 50 km for our models, which was chosen to be deeper than the Moho throughout our study region. As isostatic equilibrium is defined by equal pressures at the compensation depth, we would expect to find similar pressure values beneath the CP and adjacent GB and SBRP if they are in isostatic equilibrium with each other. Conversely, if pressures are much higher or lower beneath the CP compared with the adjacent regions, they are not in a state of isostatic equilibrium which may be indicative of dynamic effects. If pressures are lower beneath the CP, it would suggest downward dynamic effects. Observed low pressures would suggest that the topography is lower than expected, indicating that some other process is creating a downward pull. If the pressures are higher beneath the CP, it would suggest upward dynamic effects, indicating that other dynamic mechanisms are required to explain the support of the CP's high topography.

4.4.2 Temperature Calculations

In order to calculate geotherms for our phase equilibria modelling efforts, we follow the methodology of Lösing et al., (2020). We incorporate heat flux data, surface temperatures, Moho and LAB temperatures, and crustal thickness into these calculations using a Bayseian Monte-Carlo-Markov-Chain (MCMC) approach. This approach is used to calculate vertical geotherms at 1-km depth intervals for each 5-km node across the study region. In our calculations, our priors are heat flow (which are allowed to range from 10-200 mW/m^2), upper crustal heat production (range: 2-6 μW/m^3), and the thickness of the upper crustal heat-producing layer (range: 2-20 km), for which we use scale parameters of 5, 0.1, and 0.5 respectively for each iteration. We also use hyperpriors for Moho temperature (ranging from 37-117 °C), lithospheric thickness (ranging from 100-200 km), and heat flow (ranging from 50-150 mW/m^2), for which we use scale parameters of 4, 4, and 8 respectively. Heat flow is included in both the prior and hyperprior with different ranges because it is required as an input into the forward model and is also used as a mechanism for evaluating the likelihood of each model run. The justification for this is that heat flow measurements are a necessary input into the geotherm calculations and data from the region are known to have high uncertainties, especially in the southern Colorado Plateau where groundwater flow is shown to reduce heat flow measurements (Morgan et al., 2010). To calculate geotherms, at each grid point we input surface temperature, crustal thickness, depth increment, and maximum model depth as fixed values. In our modelling, heat flow, heat production, and heat producing layer thickness were allowed to vary in each realization. Geotherms were then calculated using a Bayesian MCMC at each 5 km lateral gridpoint from surface LAB depth in 1-km depth increments for 10,000 iterations. In this modelling, at depths deeper than the 1300 °C adiabat, we assume an adiabatic increase in temperature of 0.3 °C per km. We use forward constraints Moho temperature, heat flow, and lithospheric thickness to calculate a composite likelihood for each model based on the hyperpriors. We choose the final geotherm based on the composite likelihood, which uses the sum of the likelihoods for Moho temperature, LAB temperature, and heat flow data. The "best" model, used for phase equilibria calculations, was calculated by taking an average of all models weighted by their composite likelihoods.

4.4.3 Density Calculation and Phase Equilibria Simulations

For our density calculations, we define four layers in the SBRP and GBP. These include an upper layer of sediment, upper crust, lower crust, and upper mantle. We use the same layering for the CP and CP margins as for the SBRP and GBP, but with the addition of a middle crust layer due to the crustal thickness of the Colorado Plateau and CP margins (> 40 km in places) relative to the SBRP and GBP. The layers are separated in our models by variations in composition, which, in turn, impacts density. We define the densities of the sedimentary, upper crustal layers, and mid-crustal layers of each province using the values and references from Table 4.1 for all models. We ran three different models - Model 1 used the constants for the lower crust in Table 4.1, and a constant value of 3300 kg/m^3 for the mantle. Model 2 densities were calculated using metamorphic phase equilibria calculations for both the lower crust and the upper mantle, assuming water-saturated conditions in the lower crust for both the CP and CP margins. Model 3 densities were calculated using metamorphic phase equilibria conditions for both the lower crust and the upper mantle, assuming anhydrous conditions in the lower crust and mantle in all provinces.

To calculate densities in this manner, we used *Perple_X* (Connolly, 2005), version 6.7.9. *Perple_X* calculates stable mineral assemblages given a user-specified bulk oxide composition and specified pressure-temperature conditions, solution models, and thermodynamic data sets. *Perple_X* allows for the calculation of rock densities by incorporating the mineral densities from these assemblages. In order to model stable mineral assemblages, we chose a bulk composition to represent the lower continental crust, and a depleted MOR (mid-ocean ridge) mantle peridotite composition to represent the lithospheric mantle.

The bulk composition chosen for the lower crust was taken from Condie and Selverstone (1999), a study which combined field, xenolith, and seismic data of the Colorado Plateau in order to determine a geochemical model for the crust. We chose a depleted MOR composition for the mantle based on Workman and Hart (2005). For each composition, we adjusted the reported weight% values of FeO_{TOTAL} to Fe_2O_3 and FeO using the $Fe^{3+}/\sum Fe$ ratio from Cottrell and Kelley (2011). All calculations were done using the *Perple_X* dataset HP11ver (Holland and Powell, 2011). The chemical system assumed for the simulations of the continental crust was SiO_2-TiO_2-Al_2O_3-FeO-Fe_2O_3-MgO-CaO-Na_2O-K_2O±H_2O. The chemical system assumed for the simulation of the mantle peridotite was SiO_2-TiO_2-Al_2O_3-FeO-Fe_2O_3-MgO-CaO-Na_2O-MnO. The bulk compositions and solution models used are listed in Table 4.2.

Continental crust density calculations were performed for both anhydrous and water-saturated conditions. We only calculated anhydrous conditions for the peridotite in the upper mantle as estimated temperatures exceed the stability field for serpentinite (Rupke et al., 2004). We used the hydrous simulations for calculations of density in the lower crust of the CP, to model the maximum effects of hydration from Farallon slab interactions (i.e. Humphreys et al., 2003; Jones et al., 2015; Schulze et al., 2015; Porter et al., 2017). In the Southern Basin and Range Province and Great Basin Provinces, we use the anhydrous continental crust simulations to calculate densities in the lower crust.

We iteratively calculate pressures in the earth using our estimated densities in Table 4.1 at the surface, and then progressing downward inputting the constants listed in Table 4.1 for the sedimentary and upper/middle crust layers. In the lower crust and mantle layers, we used the calculated densities of overlying layers to estimate pressure, and at each gridpoint we used the P-T conditions to estimate densities. In this way pressure estimates incorporated the density calculations for stable mineral assemblages generated by *Perple_X*.

Table 4.1. Density constants assigned to the Colorado Plateau, Colorado Plateau Margin, Southern Basin and Range Province, and Great Basin Province.

Layer	Colorado Plateau (kg/m^3)	CP Margin (kg/m^3)	Southern Basin and Range (kg/m^3)	Southern Great Basin Province (kg/m^3)
sedimentary layer	2500[1]	2670[2]	2670[2,3]	1930[4]
upper crust	2730[1]	2800[2]	2775[2,3]	2689[4]
middle crust	2816[1]	2816[1]	-	-
lower crust	2985[1]	2950[2]	2910[2,3]	3178[4]

Note: References: [1] Condie and Severstone (1999), [2] Hendricks and Plescia (1992), [3] Bashir et al., (2011), [4] Benz et al., (1990)

Table 4.2. Bulk compositions and solution models used in *Perple_X* modeling

Major oxides	Continental crust (Condie and Selverstone, 1999)	Mantle peridotite (Workman and Hart, 2005)	Solution models used for anhydrous continental crust	Solution models used for saturated continental crust	Solution models used for peridotite
SIO2	51.58	44.72	Cpx(HP)	Cpx(HP)	Cpx(HP)
TiO2	0.93	0.13	Gt(WPH)	Gt(WPH)	Gt(WPH)
AL2O3	16.09	3.98	Opx(HP)	Opx(HP)	O(HP)

FeO	8.6856	8.02	Pl(I1,HP)	Pl(I1,HP)	Pl(I1,HP)
Fe2O3	1.8386	0.18	San	San	Opx(HP)
MgO	5.92	38.74	Sp(HP)	Sp(HP)	Sp(HP)
CaO	8.33	3.18		Mica(CHA1)	
Na2O	3.13	0.13		GlTrTsPg	
K2O	1.34	-		Ep(HP)	
MnO	-	0.13		Chl(HP)	
				Bio(HP)	

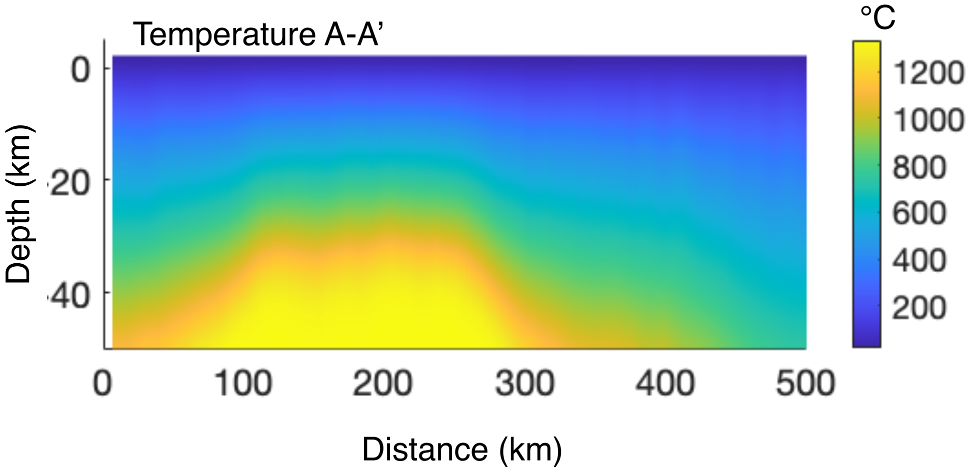

Figure 4.2. Temperatures calculated across the A-A’ transect (see Figure 4.1 for cross section location). Temperatures are in °C.

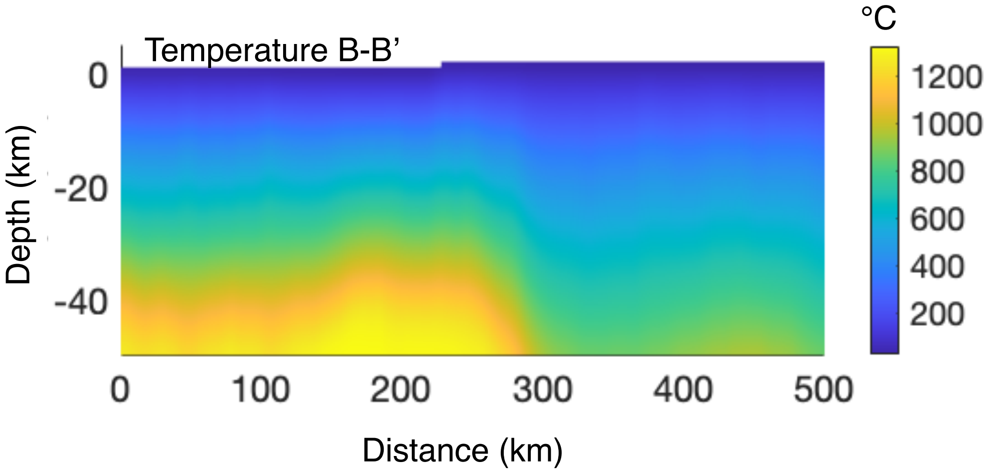

Figure 4.3. Temperatures calculated across the B-B' transect (see Figure 4.1 for cross section location). Temperatures are in °C.

4.5 RESULTS

Our results are presented for our temperature and phase equilibria calculations, as well as our density and uplift calculations across the study region, shown in Figure 4.1. We plot some results across the two cross sections, A-A' and B-B' in order to evaluate relative differences between the GBP (A-A') or SBRP (B-B') with the CP and its margins. Two cross sections, A-A' and B-B' (Figures 4.2 and 4.3) show the temperature variations between these provinces. Our MCMC calculations reveal hotter lower-crustal and upper-mantle temperatures within the GBP, SBRP, and CP margins compared with those calculated for the interior of the CP.

An example of the results of our phase equilibria calculations for the CP lower crust are shown in Figure 4.4. This example is taken at 36.7° latitude, -110.1° longitude. In Figure 4.4a we calculate that H_2O is mineral-bound in epidote, chlorite, biotite, and amphibole (Fe-hornblende) in the shallower portions of the lower crust (0.6-0.7 GPa and 450-550°C). At greater depths (0.7-1.0 GPa and 550-650°C), mineral-bound H_2O is held in white mica (margarite), chlorite, biotite, and amphibole (Fe-hornblende). At depths greater than 33 km (upwards of 1.0 GPa and 650°C), mineral-bound H_2O is held only in micas. The simulations for an anhydrous lower crust (Figure 4.6b) show assemblages primarily composed of plagioclase, pyroxenes and garnet.

We plot pressures at the compensation depth (50 km depth) along A-A' in Figure 4.5 and B-B' in Figure 4.6 for our three density models. Model 1 (plotted as a blue line in Figures 4.5 and 4.6) shows the calculated pressure using constants only for density (Table 4.1). Model 2 (plotted as a red line in Figures 4.5 and 4.6) shows results that incorporate our metamorphic phase equilibria calculations to estimate density in the lower crust and upper mantle. In Model 2, water-saturated conditions are assumed in the lower crust for the CP and CP margins. Model 3 (plotted as a yellow line in Figures 4.5 and 4.6) also incorporates metamorphic phase equilibria calculations to estimate density in the lower crust and upper mantle, but assumes anhydrous conditions in all provinces. For all models, we calculate somewhat higher pressures in the SBRP (1.52-1.56 GPa) than the CP (1.50-1.54 GPa, excluding a spike in Model 3 at ~380 km in Figure 4.6 which will be discussed later). In the GBP, we also calculate higher pressures (1.55-1.62 GPa) than is calculated in the CP (1.50-1.55 GPa) for all three models.

We calculated the difference in density (Figure 4.7) and pressure (Figure 4.8) along transects A-A' and B-B'. The results indicate that the incorporation of hydration can decrease densities in the CP lower crust by as much as 250 kg/m^3 and decrease pressure at the bottom of the models by up to 0.04 GPa. Our calculation of the difference in pressure at the compensation depth (50 km) between Models 2 (water-saturated) and Model 3 (anhydrous) is shown in Figure 4.9. At this depth, pressure is decreased by up to 0.05 GPa with the incorporation of water in the lower crust.

To locate pressure anomalies across the region, we subtracted the average regional pressure at the compensation depth from Models 2 and 3 (Figure 4.10). In our anhydrous Model 3 (Figure 4.10a) we observe higher than average pressures in the northeastern corner of the plateau near the Rocky Mountains, and also in the CP margins. Regions with positive pressure differences greater than 0.04 GPa are observed in the vicinity of the Marysvale Volcanic Field to the west and Mogollon-Datil Volcanic Field to the southeast (see Figure 4.1). Regions in the CP away from these three high pressure zones have near-average or just below average pressures. The water-saturated results of Model 2 (Figure 4.10b) reveal pressures much lower (-0.05 GPa) than the calculated average in much of the CP interior, with zones of high pressure still being observed near the Marysvale Volcanic Field and Mogollon-Datil Volcanic Field within the CP margins.

We calculated the amount of uplift associated with the incorporation of water into the lower crust of the CP and its margins in Figure 4.11a. This was accomplished by assuming a mean crustal density of 2750 kg/m^3. We subtracted our pressure results at the compensation depth (50 km) for Model 2 (water-saturated CP lower crust) from Model 3 (anhydrous CP). In the interior of the CP, the difference in uplift between the two models is as much as 1600 meters. The result of subtracting modern surface elevations from the results in Figure 4.11a is shown in Figure 4.10b. These values can be interpreted as the modern surface topography that cannot be explained by hydration, assuming that the anhydrous plateau was at sea level. This results in values of 0-800 m in the interior of the CP, and between 800-1600 m in the CP margins.

Figure 4.4. Cumulative % by volume mineral assemblages vs. depth for the Colorado Plateau lower crust. Results were calculated using *Perple_X* for a) water-saturated conditions and b) anhydrous conditions. Left plot shows the temperature and pressure conditions that correspond to the mineral modes. Hydrous minerals in panel a) are plotted in shades of blue and labeled with white text. Anhydrous minerals are plotted in warmer colors and are annotated with black text. Qtz = quartz, Pl = plagioclase, Mica = margarite, Ep = epidote, Gt = garnet, Cpx = clinopyroxene, Chl = chlorite, Bio = biotite, Amph = amphibole, Sph = sphene, Ru = rutile, Micr = microcline, Ky = kyanite, Opx = orthopyroxene.

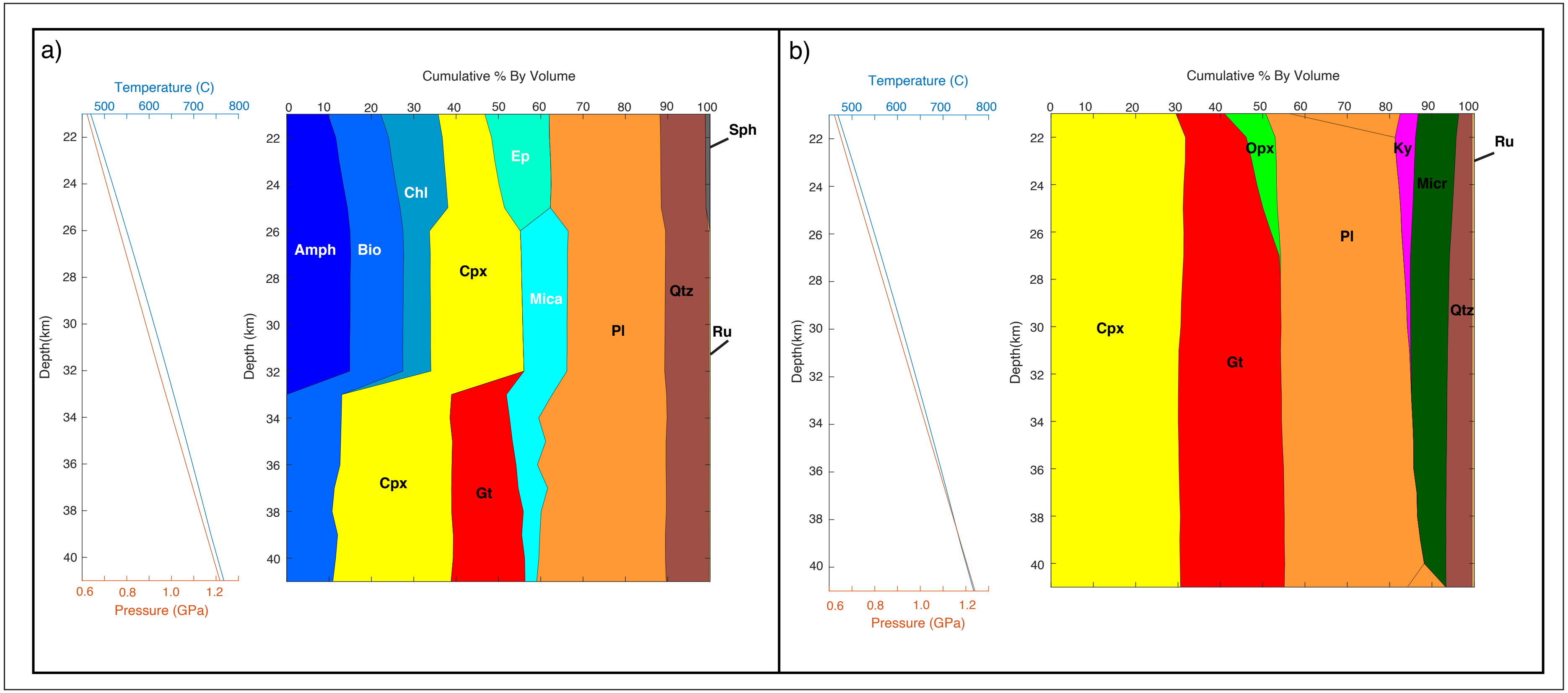
a)
Temperature (C)
500
600
700
800
Depth(km)
22
24
26
28
30
32
34
36
38
40
0.6
0.8
1.0
1.2
Pressure (GPa)
Cumulative % By Volume
0
10
20
30
40
50
60
70
80
90
100
Depth (km)
Amph
Bio
Chl
Ep
Cpx
Mica
Pl
Qtz
Sph
Ru
Cpx
Gt
b)
Temperature (C)
500
600
700
800
Depth(km)
0.6
0.8
1.0
1.2
Pressure (GPa)
Cumulative % By Volume
Opx
Ky
Micr
Ru
Cpx
Gt
Pl
Qtz

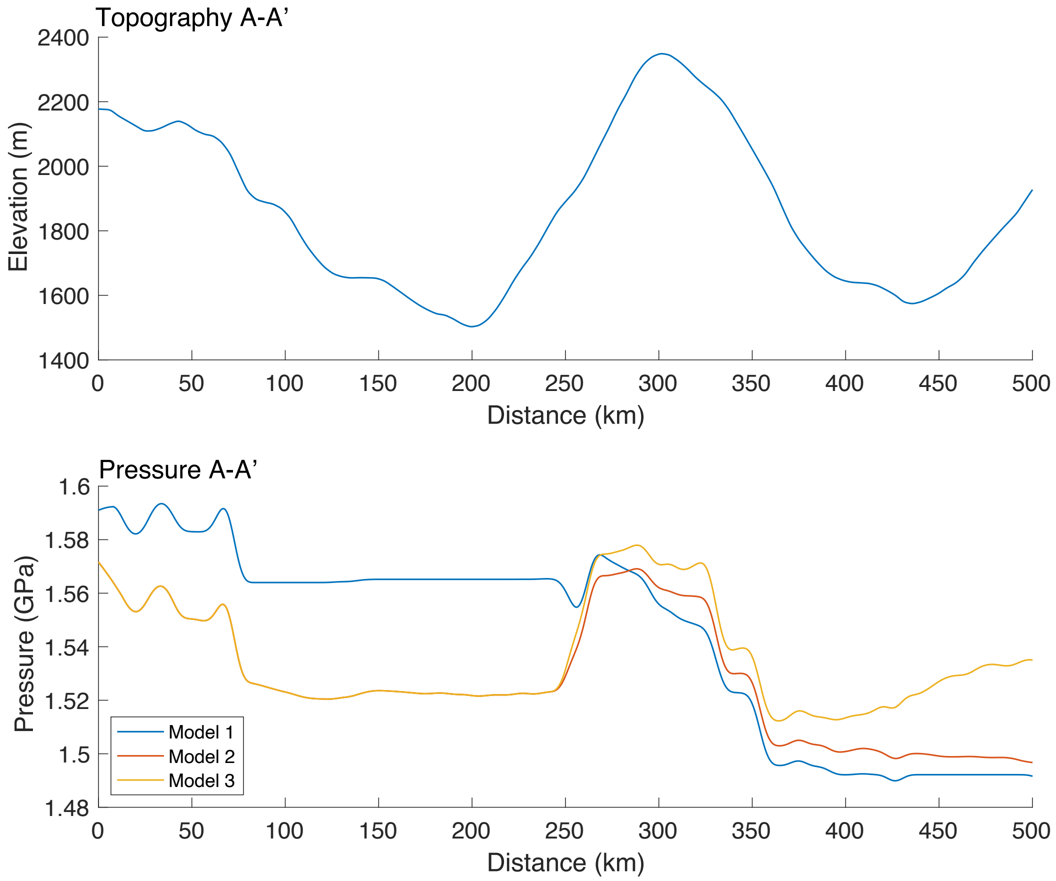

Figure 4.5. Low-pass filtered topographic elevation (top) and pressures at the compensation depth of 50 km (bottom) calculated across the A-A’ transect (see Figure 4.1 for cross section location). Model 1 (constants only for density) is the blue line. Model 2 (water-saturated simulations used for the lower crust of the CP and CP margins) is the red line. Model 3 (anhydrous simulations used for the lower crust of the CP and CP margins) is the yellow line. See the text for more detailed information on the models.

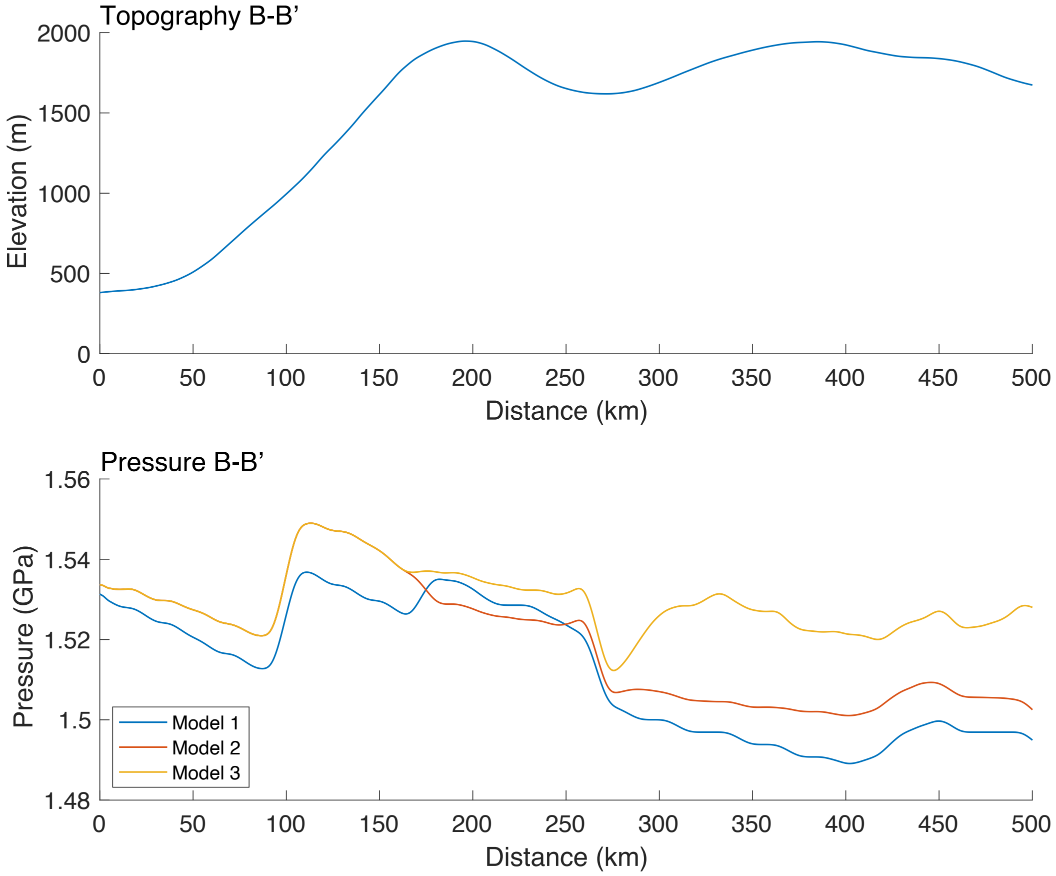

Figure 4.6. Low-pass filtered topographic elevation (top) and pressures at the compensation depth of 50 km (bottom) calculated across the B-B’ transect (see Figure 4.1 for cross section location). Model 1 (constants only for density) is the blue line. Model 2 (water-saturated simulations used for the lower crust of the CP and CP margins) is the red line. Model 3 (anhydrous simulations used for the lower crust of the CP and CP margins) is the yellow line. See the text for more detailed information on the models.

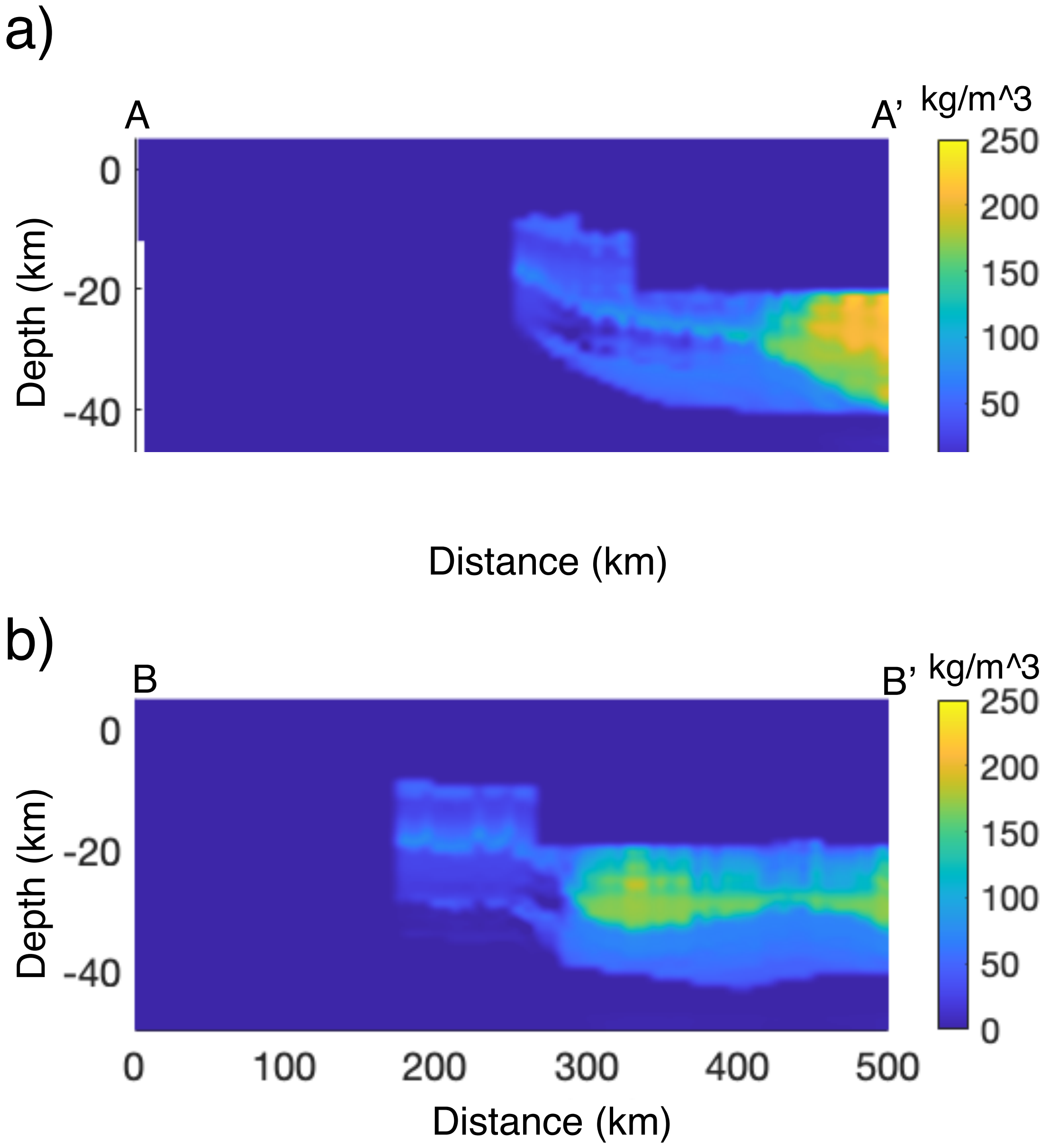

Figure 4.7. Difference in density between Model 3 (anhydrous lower crust in CP and CP margins) and Model 2 (saturated lower crust in CP and CP margins) calculated across a) the A-A' transect and b) the B-B' transect (see Figure 4.1 for cross section locations).

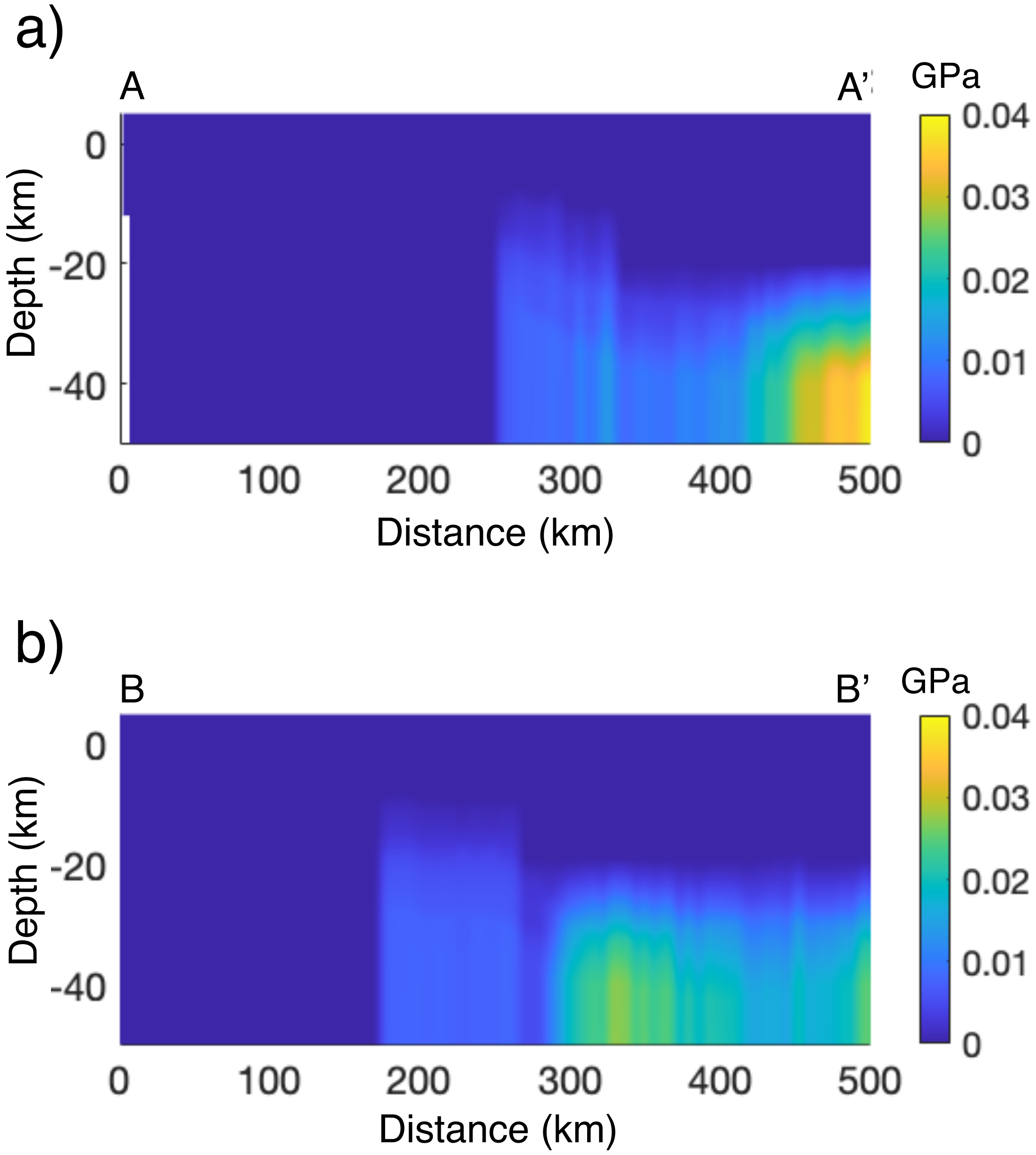

Figure 4.8. Difference in pressure between Model 3 (anhydrous lower crust in CP and CP margins) and Model 2 (saturated lower crust in CP and CP margins) calculated across a) the A-A' transect and b) the B-B' transect (see Figure 4.1 for cross section locations).

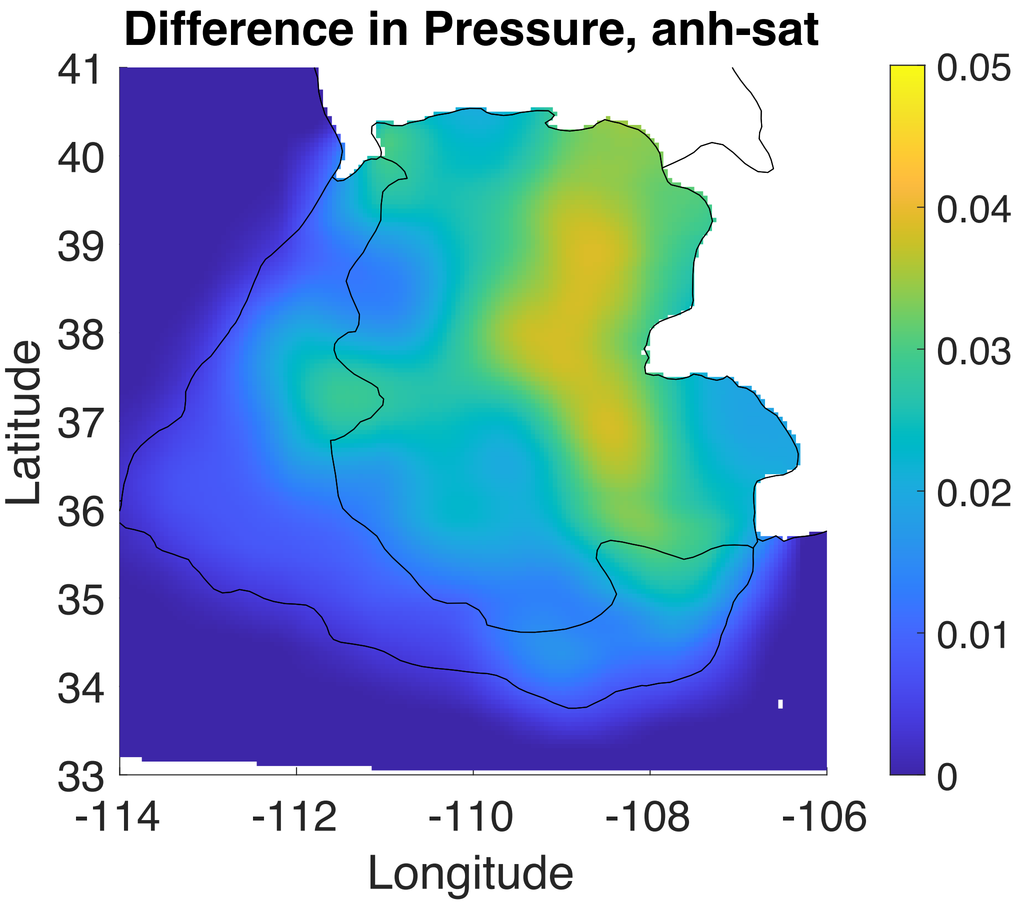

Figure 4.9. Difference in pressure between Model 3 (anhydrous lower crust in CP and CP margins) and Model 2 (saturated lower crust in CP and CP margins) at the compensation depth (50 km depth). Scale is in GPa. This shows where the effects of lower-crustal hydration are expected to be the most pronounced.

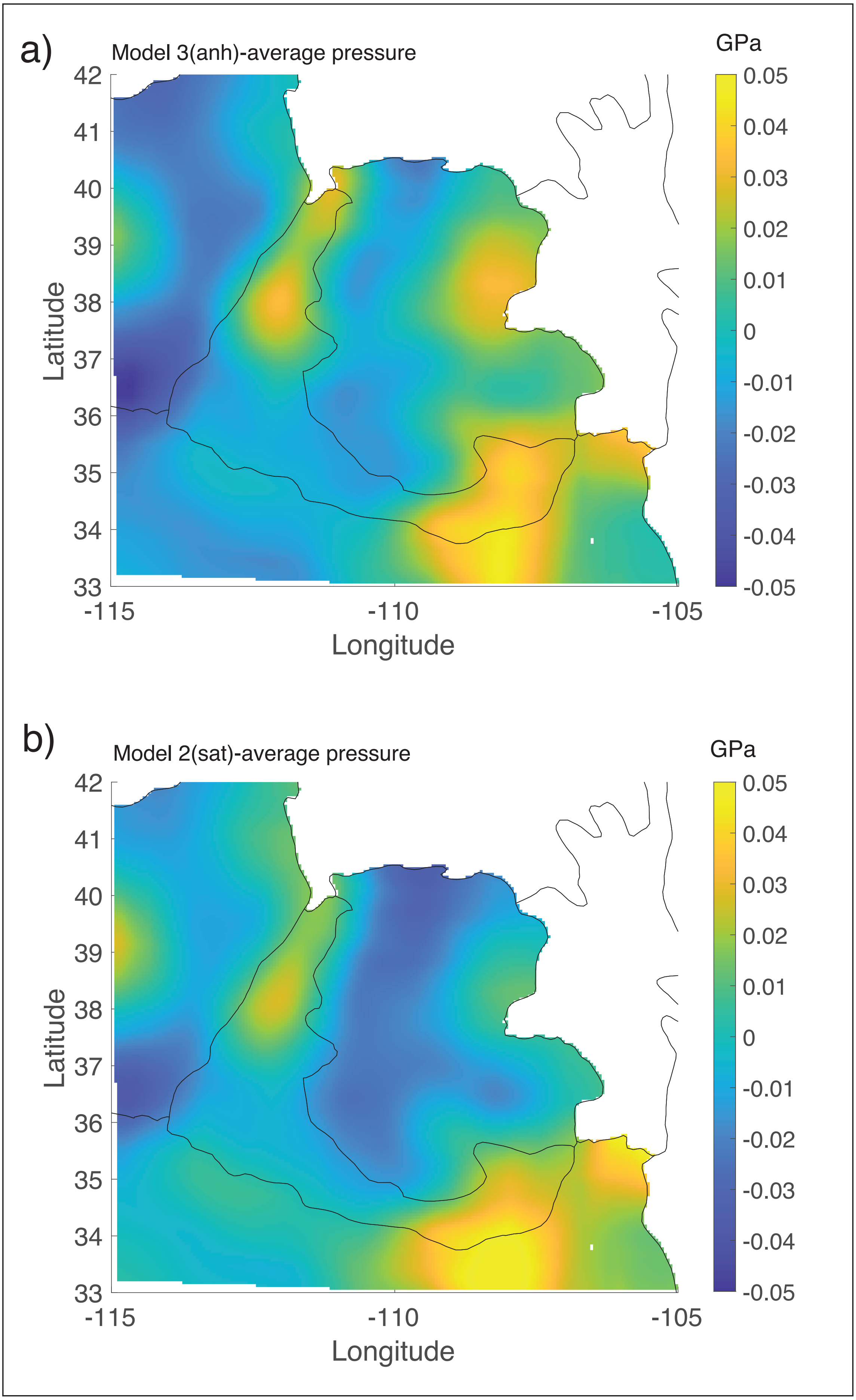
a)
Model 3(anh)-average pressure
GPa
0.05
0.04
0.03
0.02
0.01
0
-0.01
-0.02
-0.03
-0.04
-0.05
42
41
40
39
38
37
36
35
34
33
Latitude
-115
-110
-105
Longitude
b)
Model 2(sat)-average pressure
GPa
0.05
0.04
0.03
0.02
0.01
0
-0.01
-0.02
-0.03
-0.04
-0.05
42
41
40
39
38
37
36
35
34
33
Latitude
-115
-110
-105
Longitude

Figure 4.10. Difference from the average pressure for (a) anhydrous Model 3 and (b) water-saturated Model 2 in GPa. If the region was in isostatic equilibrium, it is expected that the values would be 0 throughout.

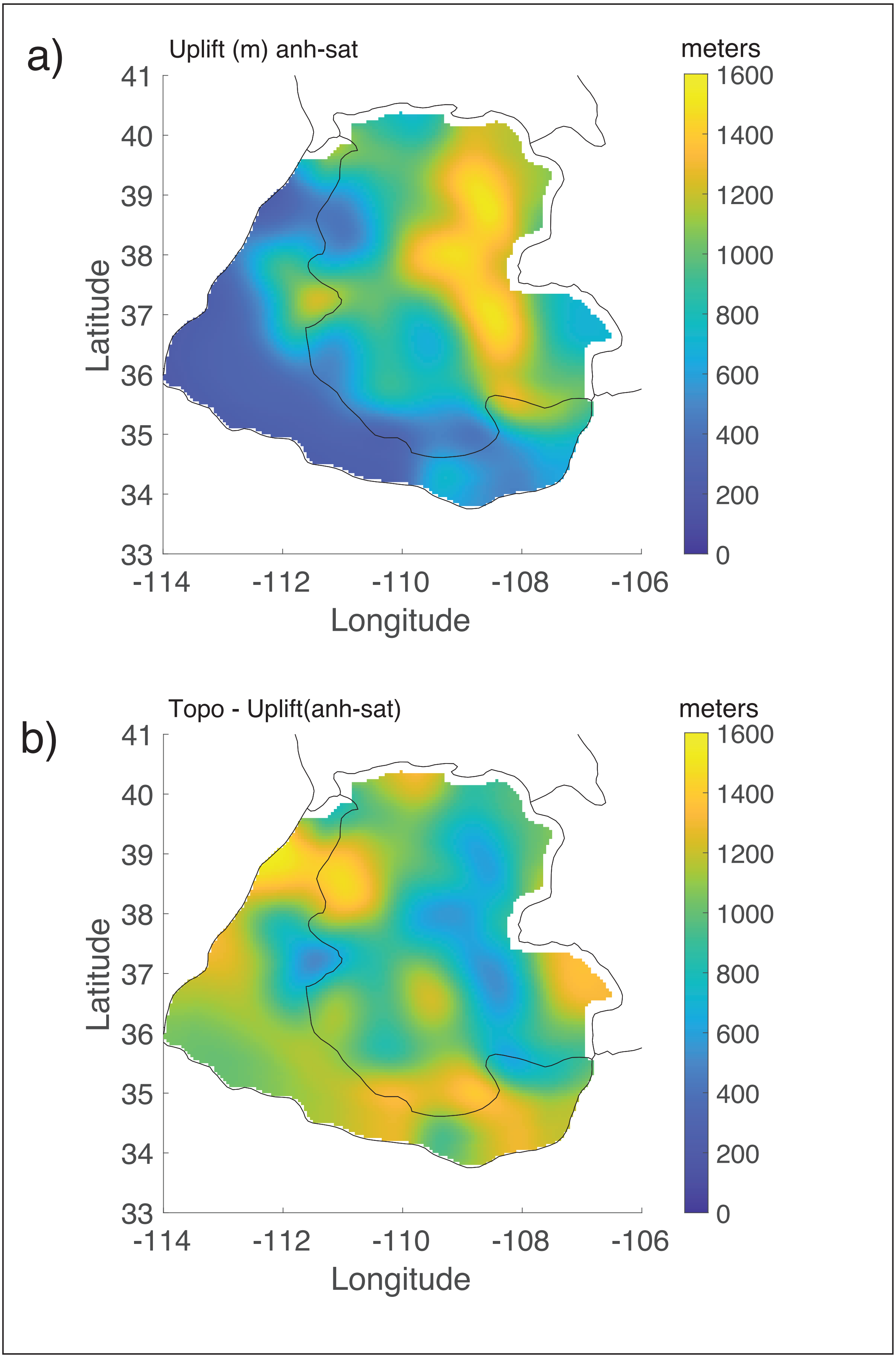
a)
Uplift (m) anh-sat
meters
1600
1400
1200
1000
800
600
400
200
0
Latitude
41
40
39
38
37
36
35
34
33
-114
-112
-110
-108
-106
Longitude
b)
Topo - Uplift(anh-sat)
meters
1600
1400
1200
1000
800
600
400
200
0
Latitude
41
40
39
38
37
36
35
34
33
-114
-112
-110
-108
-106
Longitude

Figure 4.11. Calculation of uplift in meters in the Colorado Plateau and CP margins. Map a) shows the difference in uplift between our Model 3 (anhydrous) and Model 2 (water-saturated). Map b) was calculated by subtracting the values calculated for Map a) from low-pass filtered topography of the CP and CP margins. These values can be interpreted as the modern surface topography that cannot be explained by hydration, assuming that the anhydrous plateau was at sea level.

4.6 DISCUSSION

Our results have several implications for the uplift and support of the CP's high elevations. As expected, our temperature results indicate that the CP is in a colder thermal state than either the Great Basin Province (Figure 4.2) or the Southern Basin and Range Province (Figure 4.3). This is likely due to lithospheric thinning associated with extension in both regions, which is still active in the present in the GBP. Our temperature calculations show a sharp lateral thermal gradient within the CP margins, which is the boundary region between the thinner lithosphere of the GBP and SBRP and the thicker lithosphere of the CP.

The cooler conditions within the crust of the CP allow for hydrous minerals to remain stable within the lower crust, while warmer conditions in the CP margins prohibit this. We assume that at least some hydration is present in the lower crust (per xenolith studies in the CP, e.g. Usui et al., 2003; Smith et al., 2004; Smith et al., 2010; Schulze et al., 2015). However, quantifying the extent of hydration is difficult. In this study, we simulated water-saturation in the lower crust of the CP and CP margins in our Model 2. Although it is highly unlikely that the CP lower crust is water-saturated, the phase equilibria calculations that allow for water saturation provide an upper bound for the effects of hydration on uplift. It is also possible that some hydration is present in the upper mantle beneath the CP crust. However, seismic data for the mantle beneath the CP do not show wide regions of low velocities, which is consistent with there being no widespread hydration in the mantle (e.g. Bailey et al., 2012; Buehler and Shearer, 2017). In all of our models we either assume a constant for the density of the mantle (3300 kg/m^3 in Model 1), or we simulate anhydrous peridotite using *Perple_X*.

In reality, there are likely some zones of water-saturation along cracks and faults in the lower crust and upper mantle, while regions away from these cracks are likely anhydrous, similar to what might be expected for a subducting slab (Petersen et al., 2021). Even with our modeling limitations, we can use our results to evaluate the potential effect that lower crustal hydration can have on the isostatic state of the CP.

It is important to note that we only use phase equilibria calculations for regions deeper than the middle-lower crustal boundary. In the CP, we define this as approximately 20 km depth. Shallower regions in our models are assumed to be unaltered sediments and igneous rocks that likely have not reached temperature/pressure conditions that produce metamorphic reactions which significantly alter their density state (Petersen et al., 2021). We therefore assume constants for these lithologies taken from other studies in the region (i.e. Condie and Selverstone, 1990; Bashir et al., 2011). Additionally, the assumed lithologies used for our phase equilibria simulations may not accurately represent the lithologies of the Basin and Range lower crust. In many regions of the Basin and Range Province, crustal velocities are low (Porter et al., 2014). This may indicate that our compositional estimates for the Basin and Range may not be felsic enough, which would mean we may be slightly overestimating densities and pressures in some areas of our models.

Model 1 was calculated using only constants for comparison with our models that incorporate phase equilibria calculations (Models 2 and 3). In Figures 4.5 and 4.6, we see that Model 1 calculations result in lower pressures in the GBP, CP, and SBRP than either Model 2 or Model 3. In the CP margins adjacent to the GBP (Figure 4.5), Model 1 estimates are similar to both Model 1 and Model 2. In the CP margins adjacent to the SBRP (Figure 4.6), Model 1 calculated pressures are slightly higher than either Model 2 or Model 3. One possible explanation for this is that the density constant used for the CP lower crust from Condie and Selverstone (1999) is a value estimated using measurements from the CP interior and does not account for the effects of pressure or temperature. In this region temperatures are likely much lower, meaning that using this value everywhere for the CP lower crust would result in an underestimate of pressure, which is what we observe in our results.

Additionally, our models primarily focus on differences between the CP and SBRP/GB. It is possible that there may be broad regional processes that are affecting density, which would not be reflected in our results. There also may be dynamic processes that are impacting the SBRP and GB that do not impact the CP. In effect, our models only allow for the interpretation of smaller-scale and relative effects between the provinces.

Our results for pressure across the GBP (Figure 4.5) and the SBRP (Figure 4.6) indicate that an anhydrous CP (Model 3) is essentially in isostatic equilibrium with both adjacent provinces. However, there are some isolated areas where pressures are relatively higher or lower, indicating downwelling or uplift respectively (see Figure 4.10). Hydrating the lower crust (Model 2) reduces pressures in the interior of the CP by up to 0.05 GPa (see Figure 4.9). We calculate that hydration in the lower crust could contribute to up to 1600 meters of uplift in the plateau interior relative to an anhydrous CP (see Figure 4.11a). Although we allowed for water saturation in our *Perple_X* simulations of the CP margins, we see in Figure 4.11a that little to no uplift can be associated with the presence of water. This is because of the higher temperatures calculated within the CP margins (see Figures 4.2 and 4.3). These hotter temperatures do not allow for the stabilization of hydrous minerals. We observe in Figure 4.7 that within the CP margins, rock densities are only reduced by approximately 25-50 kg/m^3 with the inclusion of water into our simulations, whereas densities in the plateau interior are reduced by up to 250 kg/m^3 with water-saturation. It is possible that volcanism in the CP margins may have felsified the crust, as seismic velocities and gravity are both low in these regions.

From our results we theorize that the Colorado Plateau interior is likely in isostatic equilibrium with the Basin and Range Province. We also note that the addition of hydration to the lower lithosphere of the CP could account for much of the elevation in the interior of the plateau. However, on the edges of the CP near recent volcanic centers, high pressures relative to the adjacent Basin and Range Province suggest that the high elevations observed here are supported dynamically rather than isostatically. Small-scale upper-mantle convection in these regions along with thermal expansion and felsification of the crust due to volcanism likely explains the elevation in these regions. Additionally, the upwelling asthenosphere in the plateau margins would likely be flowing downward beneath the plateau itself (e.g. van Wijk et al., 2010). This dynamic subsidence may be counteracted by hydration of the CP interior.

4.7 CONCLUSION

The results of this study indicate that the interior of the Colorado Plateau is largely in isostatic equilibrium with the adjacent Basin and Range. At the edges of the CP however, results indicate that the observed high elevations, which are greater than the plateau interior, are either supported through thermal expansion, or by dynamic forces such as small-scale mantle convection. Hydration in the lower crust of the CP could account for up to 1600 m of elevation in the interior, while the edges of the CP are too hot to retain much mineral-bound H_2O.

4.8 ACKNOWLDEGMENTS

This work was funded by NSF Awards EAR-1645227 and EAR-1829520.

4.9 REFERENCES

Bailey, I. W., Miller, M. S., Liu, K., & Levander, A. (2012). VS and density structure beneath the Colorado Plateau constrained by gravity anomalies and joint inversions of receiver function and phase velocity data. Journal of Geophysical Research: Solid Earth, 117(B2).

Bashir, L., Gao, S. S., Liu, K. H., & Mickus, K. (2011). Crustal structure and evolution beneath the Colorado Plateau and the southern Basin and Range Province: Results from receiver function and gravity studies. Geochemistry, Geophysics, Geosystems, 12(6).

Benz, H. M., Smith, R. B., & Mooney, W. D. (1990). Crustal structure of the northwestern Basin and Range Province from the 1986 Program for Array Seismic Studies of the Continental Lithosphere seismic experiment. Journal of Geophysical Research: Solid Earth, 95(B13), 21823-21842.

Bird, P., (1979). Continental delamination and the Colorado Plateau. J. Geophys. Res. 84 (B13), 7561–7571.

Buehler, J. S., & Shearer, P. M. (2017). Uppermost mantle seismic velocity structure beneath USArray. Journal of Geophysical Research: Solid Earth, 122(1), 436-448.

Ryan, W. B., Carbotte, S. M., Coplan, J. O., O'Hara, S., Melkonian, A., Arko, R., ... & Zemsky, R. (2009). Global multi-resolution topography synthesis. Geochemistry, Geophysics, Geosystems, 10(3).

Chase, C. G., Libarkin, J. A., & Sussman, A. J. (2002). Colorado Plateau: Geoid and means of isostatic support. International Geology Review, 44(7), 575-587.

Condie, K. C., & Selverstone, J. (1999). The crust of the Colorado Plateau: new views of an old arc. The Journal of geology, 107(4), 387-397.

Coney, P. J., 1978, Mesozoic-Cenozoic Cordilleran plate tectonics, in Smith, R. B., and Eaton, G. P., eds., Cenozoic tectonics and regional geophysics of the western Cordillera: Geological Society of America Memoir 152, p. 33–50.

Connolly, J. A. (2005). Computation of phase equilibria by linear programming: a tool for geodynamic modeling and its application to subduction zone decarbonation. Earth and Planetary Science Letters, 236(1-2), 524–541. https://doi.org/10.1016/j.epsl.2005.04.033

Cottrell, E., & Kelley, K. A. (2011). The oxidation state of Fe in MORB glasses and the oxygen fugacity of the upper mantle. Earth and Planetary Science Letters, 305(3-4), 270–282. https://doi.org/10.1016/j.epsl.2011.03.014

Crow, R., Karlstrom, K., Asmerom, Y., Schmandt, B., Polyak, V., & DuFrane, S. A. (2011). Shrinking of the Colorado Plateau via lithospheric mantle erosion: Evidence from Nd and Sr isotopes and geochronology of Neogene basalts. Geology, 39(1), 27-30.

Davis, G. H. (1978). Monocline fold pattern of the Colorado Plateau (Vol. 3, pp. 215-233). Matthews.

England, P. C., & Houseman, G. A. (1988). The mechanics of the Tibetan Plateau. Philosophical Transactions of the Royal Society of London. Series A, Mathematical and Physical Sciences, 326(1589), 301-320.

Flowers. R. M., Wernicke, B. P., & Farley, K. A. (2008). Unroofing, incision, and uplift history of the southwestern Colorado Plateau from apatite (U-Th)/He thermochronometry. Geological Society of America Bulletin, 120(5-6), 571-587.

Flowers, R. M. (2010). The enigmatic rise of the Colorado Plateau. Geology, 38(7), 671-672.

Gilbert, H. J., Sheehan, A. F., Dueker, K. G., & Molnar, P. (2003). Receiver functions in the western United States, with implications for upper mantle structure and dynamics. Journal of Geophysical Research: Solid Earth, 108(B5).

Hendricks, J. D., & Plescia, J. B. (1991). A review of the regional geophysics of the Arizona transition zone. Journal of Geophysical Research: Solid Earth, 96(B7), 12351-12373.

Holland, T. J. B., & Powell, R. (2011). An improved and extended internally consistent thermodynamic dataset for phases of petrological interest, involving a new equation of state for solids. Journal of Metamorphic Geology, 29(3), 333–383. https://doi.org/10.1111/j.1525-1314.2010.00923.x

Humphreys, E., Hessler, E., Dueker, K., Farmer, G. L., Erslev, E., & Atwater, T. (2003). How Laramide-age hydration of North American lithosphere by the Farallon slab controlled subsequent activity in the western United States. International Geology Review, 45(7), 575-595.

Jones, C. H., Mahan, K. H., Butcher, L. A., Levandowski, W. B., & Farmer, G. L. (2015). Continental uplift through crustal hydration. Geology, 43(4), 355-358.

Levandowski, W., Jones, C. H., Butcher, L. A., & Mahan, K. H. (2018). Lithospheric density models reveal evidence for Cenozoic uplift of the Colorado Plateau and Great Plains by lower-crustal hydration. Geosphere, 14(3), 1150-1164.

Lösing, M., Ebbing, J., & Szwillus, W. (2020). Geothermal heat flux in Antarctica: assessing models and observations by bayesian inversion. Frontiers in Earth Science, 8, 105.

Marshak, S., Domrois, S., Abert, C., Larson, T., Pavlis, G., Hamburger, M., ... & Chen, C. (2017). The basement revealed: Tectonic insight from a digital elevation model of the Great Unconformity, USA cratonic platform. Geology, 45(5), 391-394.

McGetchin, T. R., Burke, K. C., Thompson, G. A., & Young, R. A. (1980). Mode and mechanisms of plateau uplifts. Dynamics of plate interiors. Washington, DC, American Geophysical Union(Geodynamics Series., 1, 99-110.

McQuarrie, N., & Chase, C. G. (2000). Raising the Colorado plateau. Geology, 28(1), 91-94.

Molnar, P., & England, P. (1990). Late Cenozoic uplift of mountain ranges and global climate change: chicken or egg?. Nature, 346(6279), 29-34.

Morgan, P., & Swanberg, C. A. (1985). On the Cenozoic uplift and tectonic stability of the Colorado Plateau. Journal of Geodynamics, 3(1-2), 39-63.

Morgan, P., Sass, J. H., & Duffield, W. (2010). Geothermal Resources Evaluation Program of the Eastern San Francisco Volcanic Field, Arizona.

Parsons, T., & McCarthy, J. (1995). The active southwest margin of the Colorado Plateau: Uplift of mantle origin. Geological Society of America Bulletin, 107(2), 139-147.

Peacock, S. M. (1993). Large-scale hydration of the lithosphere above subducting slabs. Chemical Geology, 108(1-4), 49-59.

Pederson, J. L., Mackley, R. D., & Eddleman, J. L. (2002). Colorado Plateau uplift and erosion evaluated using GIS. GSA TODAY, 12(8), 4-10.

Porter, R. C., Fouch, M. J., & Schmerr, N. C. (2014). Dynamic lithosphere within the Great Basin. Geochemistry, Geophysics, Geosystems, 15(4), 1128-1146.

Porter, R., Hoisch, T., & Holt, W. E. (2017). The role of lower-crustal hydration in the tectonic evolution of the Colorado Plateau. Tectonophysics, 712, 221-231.

Porter, R., & Reid, M. (2021). Mapping the Thermal Lithosphere and Melting across the Continental US. Geophysical Research Letters, 48(7), e2020GL092197.

PRISM Climate Group, Oregon State University, http://prism.oregonstate.edu, created 18 Apr 2018.

Reid, M. R., Bouchet, R. A., Blichert-Toft, J., Levander, A., Liu, K., Miller, M. S., & Ramos, F. C. (2012). Melting under the Colorado Plateau, USA. Geology, 40(5), 387-390.

Roy, M., Kelley, S., Pazzaglia, F., Cather, S., & House, M. (2004). Middle Tertiary buoyancy modification and its relationship to rock exhumation, cooling, and subsequent extension at the eastern margin of the Colorado Plateau. Geology, 32(10), 925-928.

Roy, M., Jordan, T. H., & Pederson, J. (2009). Colorado Plateau magmatism and uplift by warming of heterogeneous lithosphere. Nature, 459(7249), 978-982.

Rüpke, L. H., Morgan, J. P., Hort, M., & Connolly, J. A. (2004). Serpentine and the subduction zone water cycle. Earth and Planetary Science Letters, 223(1-2), 17-34.

Schulze, D.J., Davis, D.W., Helmstaedt, H., Joy, B., 2015. Timing of the Cenozoic “Great Hydration” event beneath the Colorado Plateau: Th-Pb dating of monazite in Navajo volcanic field metamorphic eclogite xenoliths. Geology 43 (8), 727–730.

Schutt, D. L., Lowry, A. R., & Buehler, J. S. (2018). Moho temperature and mobility of lower crust in the western United States. Geology, 46(3), 219-222.

Sine, C. R., Wilson, D., Gao, W., Grand, S. P., Aster, R., Ni, J., & Baldridge, W. S. (2008). Mantle structure beneath the western edge of the Colorado Plateau. Geophysical Research Letters, 35(10).

Smith, D., Connelly, J.N., Manser, K., Moser, D.E., Housch, T.B., McDowell, F.W., and Mack, M.E., 2004, Evolution of Navajo eclogites and hydration of the mantle wedge below the Colorado Plateau, southwestern United States: Geochemistry, Geophysics, Geosystems, v. 5, Q04005, doi:1029/2003GC000675.

Smith, D., 2010, Antigorite peridotite, metaserpentinite, and other inclusions within diatremes on the Colorado Plateau, SW USA: Implications for the mantle wedge during low-angle subduction: Journal of Petrology, v. 51, p. 1355–1379, doi:10.1093/petrology/egq022.

Spencer, J. E. (1996). Uplift of the Colorado Plateau due to lithosphere attenuation during Laramide low-angle subduction. Journal of Geophysical Research: Solid Earth, 101(B6), 13595-13609.

Thompson, G. A., & Zoback, M. L. (1979). Regional geophysics of the Colorado Plateau. Tectonophysics, 61(1-3), 149-181.

Usui, T., Nakamura, E., Kobayashi, K., Maruyama, S., and Helmstaedt, H., 2003, Fate of the subducted Farallon plate inferred from eclogitic xenoliths in the Colorado Plateau: Geology, v. 31, p. 589–592, https://doi.org/10.1130/0091-7613(2003)031<0589:FOTSFP>2.0.CO;2

Van Wijk, J. W., Baldridge, W. S., Van Hunen, J., Goes, S., Aster, R., Coblentz, D. D., ... & Ni, J. (2010). Small-scale convection at the edge of the Colorado Plateau: Implications for topography, magmatism, and evolution of Proterozoic lithosphere. Geology, 38(7), 611-614.

Workman, R. K., & Hart, S. R. (2005). Major and trace element composition of the depleted MORB mantle (DMM). Earth and Planetary Science Letters, 231(1-2), 53-72.

CHAPTER 5: SUMMARY AND CONCLUSIONS

The results from the studies within this dissertation provide valuable insight into flat-slab subduction zone systems. In chapter 2, we examine the Alaskan flat-slab subduction region, and evaluate whether hydration is necessary to sustain a low angle of subduction many kilometers from the trench. We conclude that an anhydrous slab does not have sufficient buoyancy to maintain the observed geometry in Alaska. We estimate that 1-1.5 % chemically bound H_2O is necessary to maintain buoyancy to the observed distance from the trench (~400 km).

In chapter 3, we compare our models from chapter 2 with observed seismic data. By using our models to estimate P and S wave velocities, we evaluate the accuracy of our thermal modelling and our conclusions regarding the hydration state of the Alaskan flat-slab subduction region. By doing so we find that our models that include approximately 3% chemically bound H_2O in the subducting crust and upper mantle best match the observational seismic tomography models. This study allows for a comparison of forward modeling with observational seismic methods to provide better estimates for the hydration state of a flat-slab subduction zone than previous studies.

Through our analysis of the Alaskan flat-slab subduction zone in chapters 2 and 3, we find new valuable insights into modern flat-slab systems as a whole. Our thermal models revealed cold temperatures within the subducting slab relative to slabs in typical steeply-subducting systems. The lower temperatures within the slab allow for hydrous mineral assemblages to remain stable, which, in turn, reduce slab density. The low temperatures also delay dehydration reactions within the slab that would otherwise lead to eclogitization and densification. This allows the slab to retain slab buoyancy to several hundred kilometers inboard from the trench. We estimate hydration within the Alaskan subducting slab where it exhibits a low subduction angle. It likely contains 3% mineral-bound water throughout the 20-

km thick crust as well as in the upper ~10 km of the mantle. We find that hydration contributes to flat-slab subduction in Alaska and likely has implications for other flat-slab subduction systems. These results provide valuable insight into the important role that water plays in these low-angle subduction systems.

The methodology used in chapters 2 and 3 has potential applications for the study of other flat-slab subduction systems, and subduction systems as a whole. Bridging the gap between thermal modeling, metamorphic phase equilibria modeling, and observational geophysics is important for providing a better understanding of subduction zones and addressing broad tectonic problems. Forward modeling also allows us to better constrain variables that affect seismic wavespeed. By constraining temperature, composition, and pressure, we can isolate the effects of hydration and better interpret the hydration state of the region.

In chapter 4, we similarly attempted to evaluate the thermal and compositional state of the Colorado Plateau and surrounding region. While the Colorado Plateau is not currently near a subduction zone, it is theorized that flat-slab subduction during the Laramide orogeny may have hydrated the lower lithosphere of the Colorado Plateau. We therefore model the difference between an anhydrous lower crust and a water-saturated lower crust in the Colorado Plateau. We find in our models that hydration of the lower crust could account for up to 1600 m of uplift in the interior. However, hydration cannot account for the high elevations observed on the plateau margins. We conclude that uplift in this region is likely due to dynamic upper mantle upwelling and small-scale convection on the plateau edges.

These studies provide insight into the role that water plays in flat-slab subduction systems. We find that hydration of subducting slabs keeps them buoyant, which allows them to resist steep subduction. We also find that interactions of a subducting flat slab with the overriding continental lithosphere likely refrigerates and hydrates it. This can have implications later for both volcanism during rollback, and in the case of the Colorado Plateau, buoyancy and uplift of the continental crust.

Additionally, the methodologies used in these studies have broad implications for studying other flat-slab subduction regions, as well as tectonic systems as a whole. Using forward modeling to constrain temperature and composition allows for better interpretations of observational datasets, including but not limited to seismic datasets. The recent advancements in the volume and quality of observational data requires geoscientists to carefully analyze and interpret these data. By using the forward modeling techniques presented in this dissertation, one can constrain variables like temperature and composition, which, in turn, allows for a more informed analysis and interpretation of various geologic settings.

APPENDICES

Appendix A

This appendix contains supplementary text and figures from Chapter 2 as well as a permanent link to Dataset S1.

Contents of this Appendix

Text A1 to A5
Figures A1 to A10
Description and link for Dataset S1

Introduction

These supplementary materials provide a comparison of models calculated using *Thermodsubduct*, which uses a finite difference method, with models calculated by *PGCTherm2D*, which uses a finite element method. In addition, we take the opportunity to provide benchmarking and other code validation tests for *Thermodsubduct*, which has been updated since the release of *Thermod7* (Hoisch, 2005) to include the incorporation of frictional heating, mantle corner flow, and the method of Leveque (1996) for the simulation of advection (described in more detail below). For a discussion of benchmarking of the *PGCTherm2D* codes see Van Keken et al. (2008).

To generate models for comparison, we set up both programs to solve the same problem to the maximum extent possible, with the same fault geometry, fault velocity, physical constants, layer thicknesses, vector domain boundaries for the lower plate, mantle convection domain geometry and stream function, and boundary conditions. However, differences between models computed by the two methods are unavoidable due to different treatments of the lower boundary of the model domain (explained below), and due to Thermodsubduct being a forward model that calculates time-dependent evolutions, whereas *PGCTherm2D* calculates steady-states.

Text A1. Boundary conditions and model domains

Boundary conditions for the two modeling systems are shown in Figure A1a (*PGCTherm2D*) and Figure A1b (*Thermodsubduct*). In both systems the top boundary (Earth's surface) is kept at a constant temperature of 0 °C. The left-side boundary is also held constant and comprises the oceanic geotherm. The right-side boundary for the *PGCTherm2D* model is a composite boundary. From the surface to the inflow-outflow transition in the mantle convection domain is a constant temperature boundary consisting of the continental geotherm; below this point it is a zero heat-flux boundary. The *Thermodsubduct* model is extended to the right 230 km farther than the *PGCTherm2D* model so that the inflow-outflow transition coincides with the lower-right corner of the model domain. This allowed the entire right-side to be treated as a constant temperature boundary consisting of the continental geotherm, analogous to the treatment in *PGCTherm2D*.

The major differences between setups of the models are with the lower boundary condition and with the geometry of the model domain along this boundary. In the *Thermodsubduct* model the lower boundary is set to a constant heat flux, whereas the lower boundary of the *PGCTherm2D* model is set to a constant temperature of 1450 °C at the base of the 80 km thick oceanic lithosphere. The lower boundary of the *Thermodsubduct* model consists of the bottom of the rectangular model domain, whereas the lower boundary of the *PGCTherm2D* model domain consists of the base of the oceanic lithosphere.

Text A2. Movement and frictional heating

Boundary Movement within finite difference systems is handled by vector assignments to individual nodes within the grid. In *Thermodsubduct* movement of the lower plate is defined by a fault-bend-fold geometry consisting of three vector domains (Figure A2). Nodes within a single domain are assigned vectors with magnitude equal to the fault velocity (5 cm/yr) and direction paralleling the fault surface. Motion within the mantle cornerflow domain was assumed to be isoviscous and was calculated using the stream function of Batchelor (1967). Frictional heating was accomplished by assigning additional heat production (adding to radiogenic heat production) to nodes captured within a specified distance of the fault surface, which was assumed to 1 km in order to produce a layer of width equal to the node spacing (2 km), which is the narrowest width that can be resolved on a regular finite difference grid. Frictional heating along the subduction interface assumed a continuous temperature-dependent decrease of 1/e for every 60 °C of temperature increase starting at 300 °C (e.g., Kohn et al., 2018; Peacock et al., 1994). This simulates a reduction in frictional heating due to increasing ductility with increasing temperature. Each captured node was assigned a value for frictional heat production that corresponds to the value calculated for the closest point along the subduction interface. The values are recast from surface (2D) heating to distribute the heat production within the 2 km-wide domain.

In *PGCTherm2D* the finite element model is defined by polygonal domains that have vertical left and right boundaries. Subdomain boundaries are defined by a series of points that indicate the upper and lower extent of the domains for different layers (i.e, crust, mantle) and for movement (see Figure A3). Each subdomain is assigned physical properties. Each horizontal domain must have an equal number of nodes defining it along the transect; the intersections are aligned along the vertical boundaries and represent changes (physical properties, fault angle change, corner flow domains, etc). The vertical domain boundaries used in *PGCTherm2D* presented challenges to simulating the fault-bend-fold geometry of the lower plate used in the *Thermodsubduct* model due to the non-vertical sides of the vector domain boundaries. To accomplish this in *PGCTherm2D*, non-vertical domain boundaries were approximated by a series of narrow vertical domains (Figure A3 shows model *PGCTherm2D* domains). Frictional heating is separately defined as occurring within a layer of specified width centered along the fault surface. A width of 2 km was specified to be consistent with the *Thermodsubduct* model. All run parameters for the *PGCTherm2D* model are given in Datset S1. Motion within the mantle cornerflow domain is assumed to be isoviscous and was calculated using the stream function of Batchelor (1967).

Text A3. *Thermodsubduct* benchmarking and code validation tests

Thermodsubduct uses the implicit alternating direction method for solving the 2D heat conduction equation, which is unconditionally stable for any choice of time step and node spacing (e.g., Carnihan et al., 1969). Advection within the arrays is calculated for isoviscous flow using a regular staggered Eulerian grid following Leveque (1996), in combination with the Superbee flux limiter (Roe, 1985). This method is stable for Courant numbers <1.0. The maximum Courant number calculated for models in the current study is 0.625. This method simulates motion along discontinuities (faults) in physical arrays without producing the spurious oscillations that tend to develop with less sophisticated methods. Taken together these methods approximate the solution to the PDE that describes 2D heat conduction and advection. Reducing the node spacing and/or time step reduces discretization errors and improves the accuracy of the simulation.

Thermodsubduct codes were benchmarked and tested using several approaches. To evaluate discretization error, we used a numerical simulation to solve the same problem that is solved analytically by eq. 18 of Bickle and McKenzie (1987), which is the solution to a 1d boundary value problem involving both heat conduction and advection. The solution in Bickle and McKenzie (1987) is cast in terms of dimensionless values and a Peclet number. The problem is defined by an initially linear geotherm that is held at a constant temperature at the top and bottom boundaries; uplift occurs at a specified constant rate while maintaining the constant temperature boundaries causing progressive heating within the system. Note that this problem was constructed to model temperature change associated with vertical fluid flow through a uniform porosity at a constant rate; however, because fluid flux and velocity are the same dimensions this solution also applies to uniform uplift. The test was set up for a system with a Peclet number of 8 and used dimensioned values to give the model physical meaning: a total depth of 20 km, a linear initial geotherm of 20 °C/km, thermal diffusivity of 0.011 cm2/s (1.1×10-6 m2/s), grid spacing of 1 km, time step of 1000 years, and uplift velocity of 13.89 mm/yr. Results are given in Figure A4 for 0.4, 1.0, 1.6 and 10 m.y. for both the analytical solution (labeled "EQ 18)" and the numerical simulation (labeled "S"). At the scale and line thicknesses shown the results overlap and cannot be distinguished, except for slight differences in the 10 m.y. lines (Figure A4).

The stability of the heat conduction component of the numerical calculation was tested by running a stable geotherm calculated using the analytical solution of England and Thompson (1984) out to 1 Ga using a time step of 1000 years, thermal diffusivity of 0.011 cm2/s, thermal conductivity of 0.006 cal/K cm s (2.5104 W/mK), grid spacing of 1 km, a 30.5 km top layer with internal heat production of 4×10-13 cal/cm3s (1.6736×10-6 W/m3), a 39.5 km bottom layer with zero internal heat production, a constant temperature upper boundary of 0 °C, and a constant heat flux lower boundary of 6×10-7 cal/cm2s (0.025204 W/m2). After 100,000 steps (1 Ga) the maximum error obtained was 0.074 °C (0.012%) indicating a high degree of stability. In addition, the advection code was tested in isolation on 2D physical arrays using a static velocity field containing a fault, in order to assess whether path lines develop according to the velocity field and whether spurious oscillations develop. Path lines developed as defined by the velocity field and without oscillations. These tests demonstrate that the *Thermodsubduct* codes produce robust and stable numerical solutions with low discretization error.

Text A4. Comparison of *Thermodsubduct* and *PGCTherm2D* models

To facilitate comparison of the two modeling methods we evaluated how the *Thermodsubduct* model changes along its approach to a steady state by running a model with a frictional coefficient of 0.03 out to 100 m.y. and then comparing the results at 100 m.y. to 20 m.y. (Figure A5). The comparison shows that the truncated mantle cornerflow region is cooling and the upper part of the mantle convection domain is heating. Cooling of the truncated cornerflow region is expected due to refrigeration by the slab, and heating in the upper part of the mantle convection domain is expected due to the vertical component of motion associated with mantle convection in this part of the system, resulting in the advection of heat from depth to shallower levels. We note that the Alaskan subduction zone has not achieved a steady state as the subduction of the Yakutat slab has been ongoing for about 20 million years. The *Thermodsubduct* models are calculated out to 20 m.y., partly to simulate the youthfulness of Alaskan flat-slab subduction, and partly to ensure that the leading edge of the slab passes completely through the bottom boundary of the model, thus attaining a configuration similar to the *PGCTherm2D* model.

Figure A6 shows the comparison of the model calculated by both methods for the cases of both frictional heating (frictional coefficient of 0.03) and no friction. The difference between the models (*Thermodsubduct* minus *PGCTherm2D*) is shown for models that do not incorporate frictional heating (Figure A7) and for models that incorporate frictional heating (Figure A8).

Differences observed in both models with and without shear heating include the following: (1) The mantle is hotter in the *PGCTherm2D* model just below the crust-mantle boundary in the oceanic slab. (2) The *Thermodsubduct* model is colder at the bottom boundary of the subducting slab. (3) The *Thermodsubduct* model is colder along top of the thermally defined subduction channel. (4) The *Thermodsubduct* model is hotter in the mantle corner-flow region, to the right and lower right of the rigid mantle wedge. One observed difference depends on whether frictional heating is incorporated into the model. The area shallower and to the left of the rigid mantle wedge corner is hotter in the *Thermodsubduct* model when frictional heating is not incorporated (Figure A4) and colder when frictional heating is present (Figure A5). Each of these differences is addressed below.

The difference that is observed at the crust-mantle boundary within the slab is likely explained by differences in how *PGCTherm2D* and *Thermodsubduct* define the slab crust-mantle boundary. *PGCTherm2D* separates these two regions into subdomains that operate independently, whereas in *Thermodsubduct*, physical properties are assigned to each node within the subducting crust and mantle, but there is no boundary between the crust and mantle, and therefore no potential for boundary artifacts.

Both *PGCTherm2D* and *Thermodsubduct* are programmed to behave similarly in the mantle corner flow domain. Regarding *PGCTherm2D* both Wada et al. (2008) and van Keken et al. (2008) elaborate on the difficulties of simulating mantle cornerflow due to the need to finely resolve flow in the area of the mantle wedge tip. Consequently, *PGCtherm2D* incorporates elements as small as 4 x 10-8 m in the 1 km region near the wedge tip (van Keken et al., 2008; see also Figure 3 of Wada et al., 2008). Colder temperatures calculated by *Thermodsubduct* along the top of the thermally defined subduction channel were first observed when a *Thermodsubduct* model with 5 km resolution was compared to the *PGCTherm2D* model. To test whether insufficient resolution of the *Thermodsubduct* model was the cause of this difference we ran a model with 2 km resolution. In the 2 km model the top of the thermally defined subduction channel shifted to the left of ~20 km (measured at 150 km depth), decreasing the width of the area where the two models differ (Figures A7, A8). To test whether even finer resolution might yield further improvement we ran a *Thermodsubduct* model with 1 km resolution, which further shifted the top of the thermally defined subduction channel ~3 km to the left (also measured at 150 km depth). The result shows very little change from the 2 km model, with there being no perceptible change in the wedge tip area and only very slight change to the thermally defined subduction channel. Thus, we consider that running models with finer resolution than 2 km is unproductive and that insufficient resolution does not appear to be the reason for the remaining difference. It also does not appear to be related to the calculation of steady state versus non-steady state, as judged from the 100 m.y. result calculated by *Thermodsubduct*, which yields temperatures along top of the thermally defined subduction channel that are unchanged from 20 m.y. (Figure A5). Thus, we are not able to explain the remaining difference between the models. Similarly, we are not able to explain why *Thermodsubduct* calculates hotter temperatures throughout much of the mantle cornerflow area to the lower right of the wedge tip (Figures

A7, A8), other than to conclude it is not related to steady state versus non-steady state or to differences in boundary conditions.

The difference in temperature between models at the lower boundary of the slab is the result of differences in how the lower boundary conditions of the models are defined. In *PGCTherm2D* the lower boundary of the slab defined as the lower boundary of the model domain and is set to a constant temperature of 1450 °C, whereas in *Thermodsubduct* there is no boundary at this location. Instead, there is a sharp corner in the profile of the Stein and Stein (1992) geotherm that occurs inside the model domain. As one would predict, this corner undergoes thermal diffusion during the run, rounding off the corner in the Stein and Stein (1992) geotherm and lowering temperatures.

In the shear heating models (Figures A6b and d), *PGCTherm2D* produces a much hotter solution than *Thermodsubduct*. This appears to be due to the incorporation of viscous heating within the frictional heating domain in addition to frictional heating (Wada et al., 2008), whereas *Thermodsubduct* considers only frictional heating. In both models the frictional heating domain is defined as a specified width of 2 km centered on the fault surface.

Above and to the left of the wedge tip *Thermodsubduct* calculates lower temperatures for models that incorporate frictional heating (Figure A8) and higher temperatures for models without frictional heating (Figure A7). This is puzzling because this area is too distant from the fault to be affected by frictional heating, and thus, one would not expect there to be any change in this region that would be sensitive to it. The *Thermodsubduct* models (with friction and without, Figure A6a and c) do not display a difference in this area; however, the *PGCTherm2D* models (Figure A6b and d) display a large difference, with the frictional heating model being much hotter. This accounts for the observed differences between the *Thermodsubduct* and *PGCTherm2D* models in this area, but does not explain why this part of the system is sensitive to frictional heating in the *PGCTherm2D* models.

Text A5. Calculation of phase equilibria along the fault interface, and testing of other slab hydration scenarios

We present in Figure A9 a calculation of stable mineral assemblages for the MORB composition along the fault interface. Along the fault, conditions are hotter than those observed in Figure 2.5 (see a comparison of temperatures in Figure 2.5b with Figure A9 lower panel). However, the increased temperatures do not greatly alter the mineral assemblages simulated by *Perple_X*.

In order to calculate stable mineral assemblages within *Perple_X* in the subducting crust and mantle, temperature conditions were extracted from the *PGCTherm2D* results that incorporate shear heating. Pressure was calculated iteratively using densities calculated by *Perple_X* for the model region. Temperatures and pressure conditions were then extracted at every 1 km along transect at 5 km depth (basalt) and 15 km depth (gabbro) in the crust and at 5 km depth in the slab mantle in the assumed hydrated portion (Figure A9). A smoothing parameter was used on the temperature results in order to produce cleaner figures (see Figures 2.4-2.7).

In addition to the results presented in Figure 2.8 of the Chapter 2, we tested other hybrid models that test varying degrees of hydration in the slab. This is presented in Figure A9. See the figure caption and Chapter 2 for more details about these models.

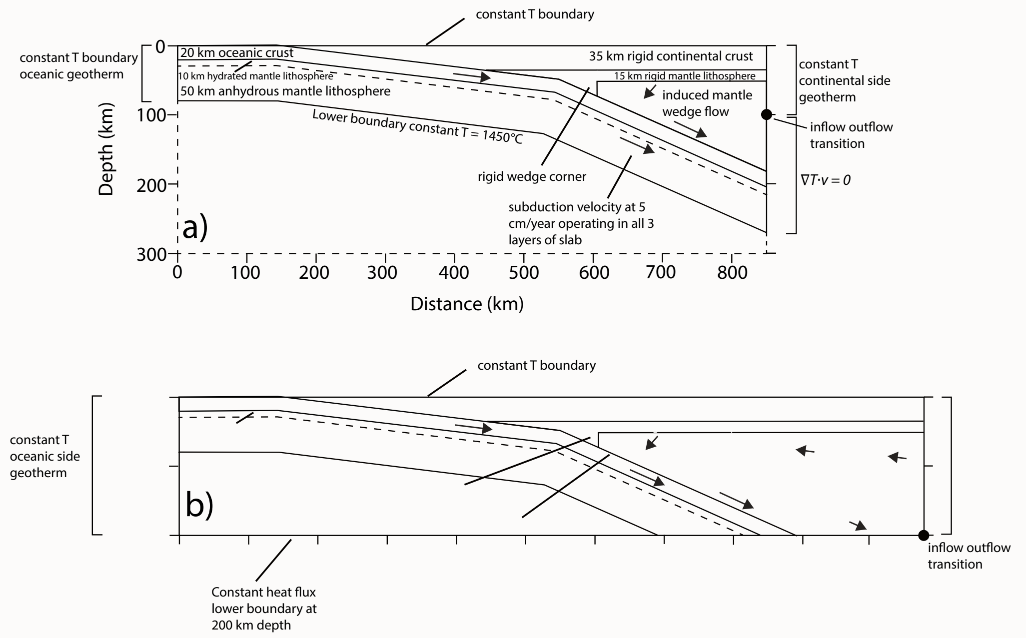

Figure A1. Model domains, boundary conditions, layer thicknesses, fault geometry, and mantle corner flow domain geometry for a) *PGCTherm2D* and b) *Thermodsubduct*. Note that in both models physical properties assigned to the mantle apply to both hydrous and anhydrous layers. The lower boundary of the model domain for *PGCTherm2D* is the bottom of the oceanic slab and is set to a constant temperature of 1450 °C, whereas the lower boundary for *Thermodsubduct* is the bottom of rectangular model domain and is set to a constant heat flux. The *PGCTherm2D* continental-side boundary is a constant temperature boundary down to the cornerflow inflow-outflow transition. Below the transition point this boundary is set to zero heat flux. For more information on how *PGCTherm2D* operates, see Currie et al. (2004).

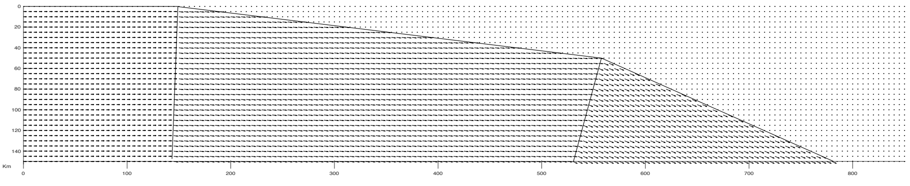

Figure A2. Assignment of nodes to vector domains within regular finite difference grid. Lower plate moves at the current convergence rate of 5 cm/yr while the upper plate remains stationary. The node spacing in this example is 5 km.

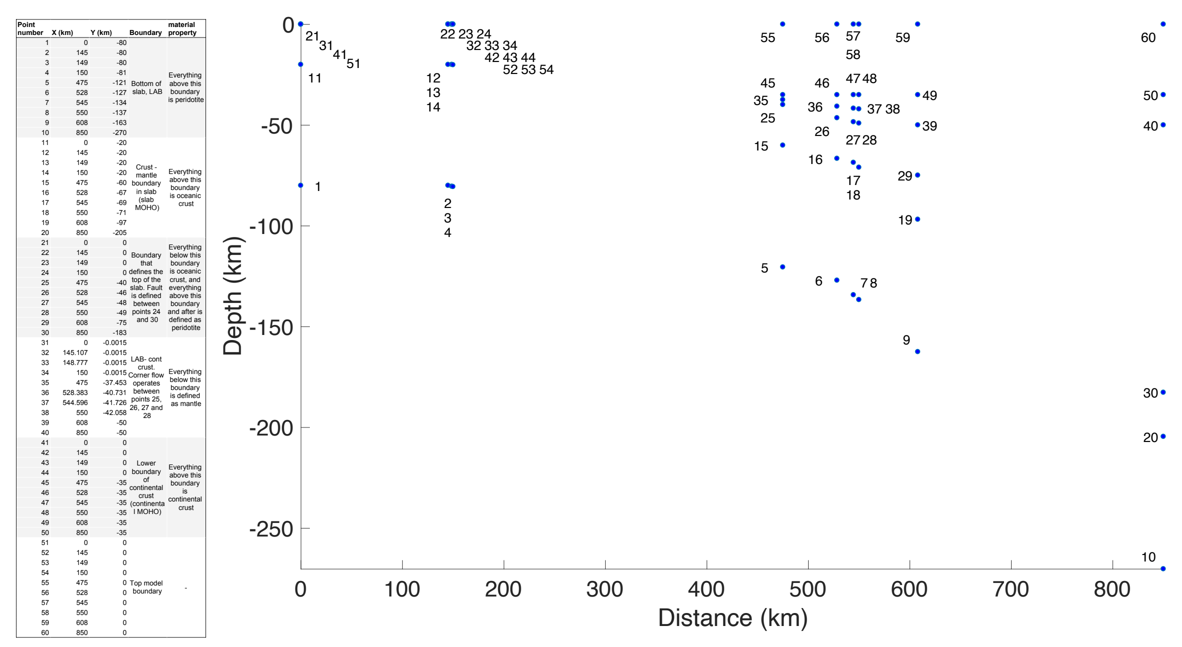

Point number	X (km)	Y (km)	Boundary	material property
1	0	-80	Bottom of slab, LAB	Everything above this boundary is peridotite
2	145	-80		
3	149	-80		
4	150	-81		
5	475	-121		
6	528	-127		
7	545	-134		
8	550	-137		
9	608	-163		
10	850	-270		
11	0	-20	Crust - mantle boundary in slab (slab MOHO)	Everything above this boundary is oceanic crust
12	145	-20		
13	149	-20		
14	150	-20		
15	475	-60		
16	528	-67		
17	545	-69		
18	550	-71		
19	608	-97		
20	850	-205		
21	0	0	Boundary that defines the top of the slab. Fault is defined between points 24 and 30	Everything below this boundary is oceanic crust, and everything above this boundary and after is defined as peridotite
22	145	0		
23	149	0		
24	150	0		
25	475	-40		
26	528	-46		
27	545	-48		
28	550	-49		
29	608	-75		
30	850	-183		
31	0	-0.0015	LAB- cont crust. Corner flow operates between points 25, 26, 27 and 28	Everything below this boundary is defined as mantle
32	145.107	-0.0015		
33	148.777	-0.0015		
34	150	-0.0015		
35	475	-37.453		
36	528.383	-40.731		
37	544.596	-41.726		
38	550	-42.058		
39	608	-50		
40	850	-50		
41	0	0	Lower boundary of continental crust (continental MOHO)	Everything above this boundary is continental crust
42	145	0		
43	149	0		
44	150	0		
45	475	-35		
46	528	-35		
47	545	-35		
48	550	-35		
49	608	-35		
50	850	-35		
51	0	0	Top model boundary	-
52	145	0		
53	149	0		
54	150	0		
55	475	0		
56	528	0		
57	545	0		
58	550	0		
59	608	0		
60	850	0		

Figure A3. Shows the geometry set-up for *PGCTherm2D*. Descriptions of boundary conditions and material properties assigned to the points are listed in the table (left).

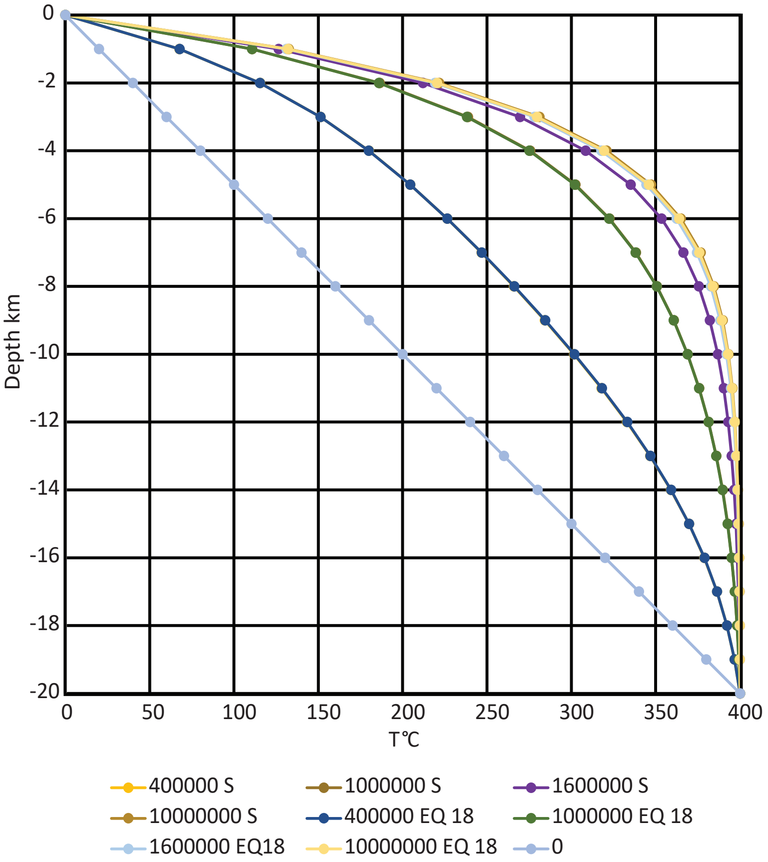

Figure A4. Comparison of solutions calculated using eq. 18 of Bickle and McKenzie (1987) with solutions calculated numerically using updated codes of Hoisch (2005). Lines are shown for specific values of time in years (lines labeled "EQ 18" were calculated using eq. 18 and lines labeled "S" are numerical simulations). Overlap causes one line for each time value to be hidden, except for the 10 m.y. (10000000) lines, which show slight differences. See Chapter 2 for further explanation.

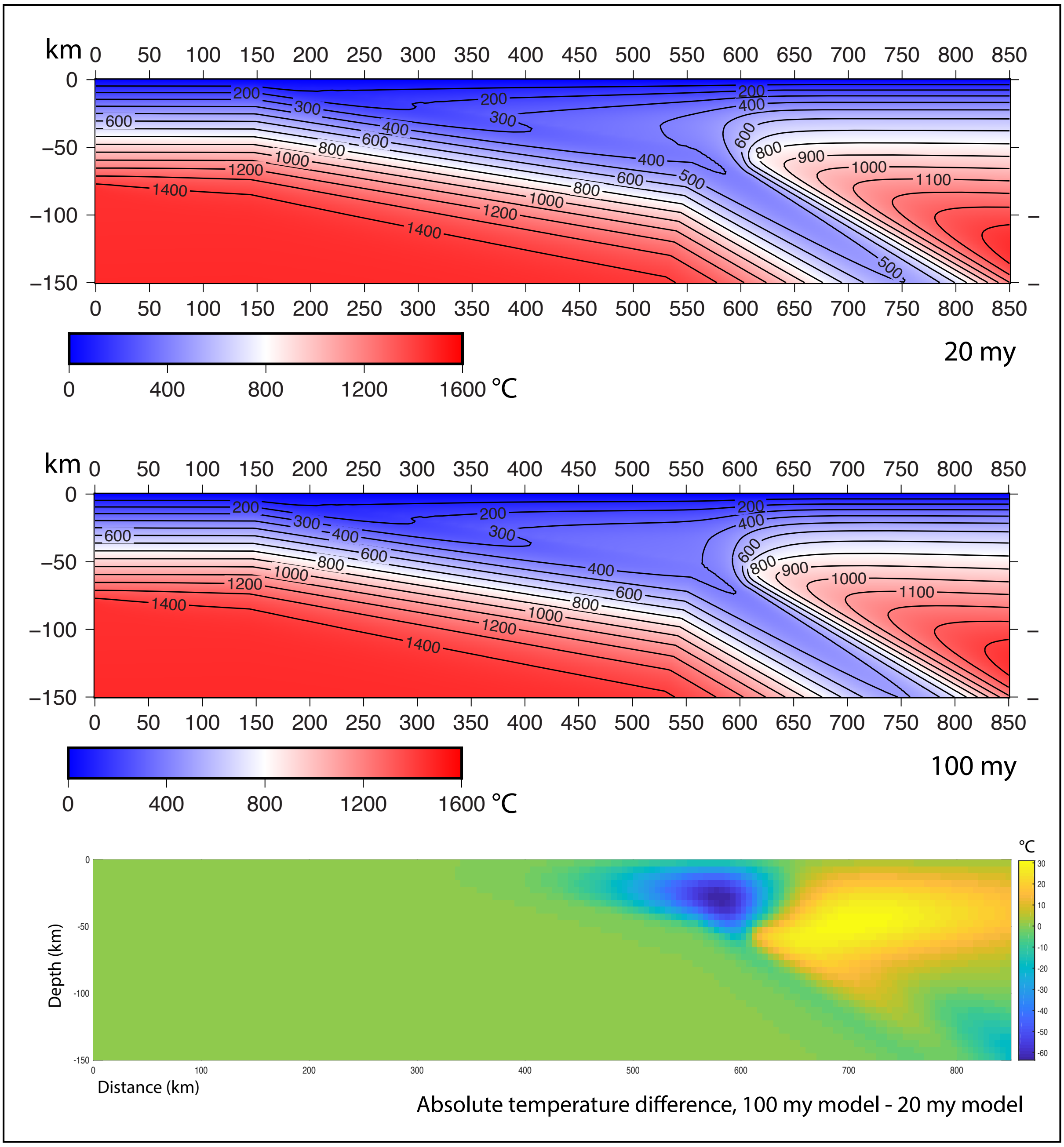

Figure A5. Comparison of *Thermodsubduct* results for 20 million years of run time (top) and 100 million years of run time (middle). The lower panel shows the absolute temperature difference in °C between the two models, showing the 20 my results subtracted from the 100 my results.

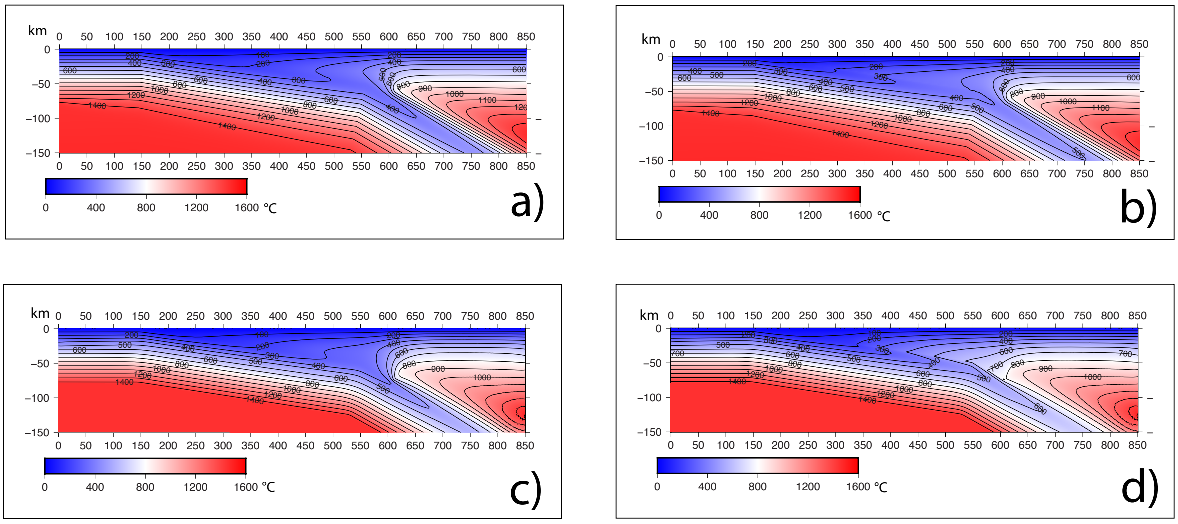

Figure A6. Figure shows comparison of *Thermodsubduct* vs. *PGCTherm2D* models. a) *Thermodsubduct* 20 m.y. model with no shear heating incorporated. b) *Thermodsubduct* 20 m.y. model with shear heating incorporated (effective frictional coefficient of 0.03. c) *PGCTherm2D* steady state model with no shear heating incorporated. d) *PGCTherm2D* steady state model with shear heating incorporated (effective frictional coefficient of 0.03). Note that the *PGCTherm2D* models (c and d) do not produce results below the bottom of the slab defined at 80 km depth on the left side of the model to be 1450 °C (paralleling the 1400 °C contour), as the bottom of the slab is the lower boundary of the model.

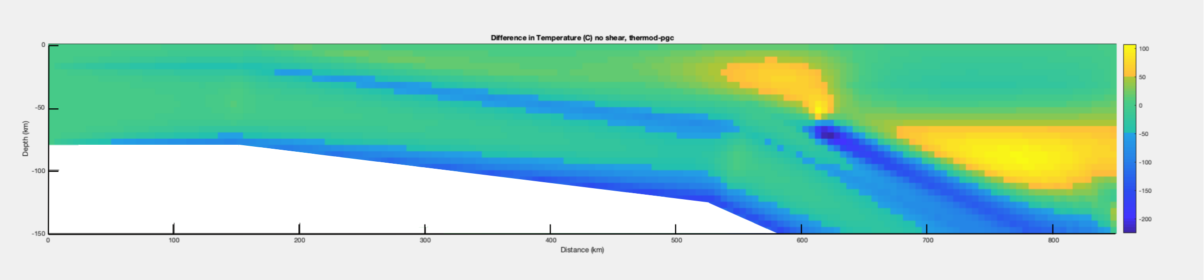

Figure A7. Figure shows comparison of *Thermodsubduct* vs. *PGCTherm2D* models. This shows the absolute temperature difference (*Thermodsubduct-PGCTherm2D*) for models that do not incorporate shear heating. Regions in green are within 50 °C.

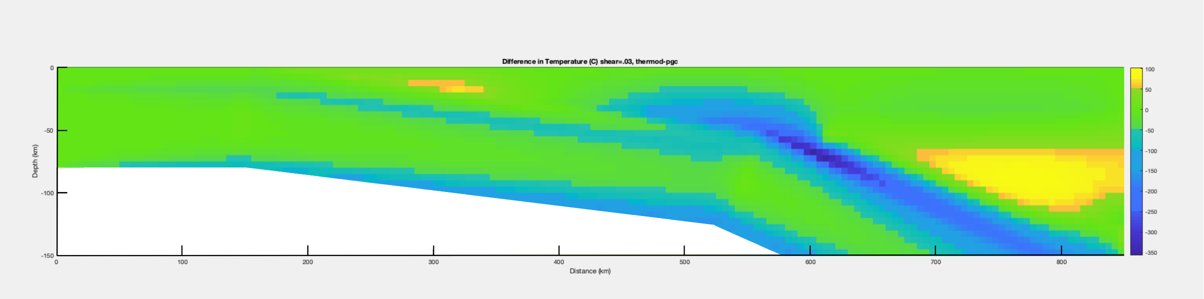

Figure A8. Figure shows comparison of *Thermodsubduct* vs. *PGCTherm2D* models. This shows the absolute temperature difference (*Thermodsubduct-PGCTherm2D*) for models that incorporate shear heating (effective frictional coefficient of 0.03). Regions in green are within 50 °C.

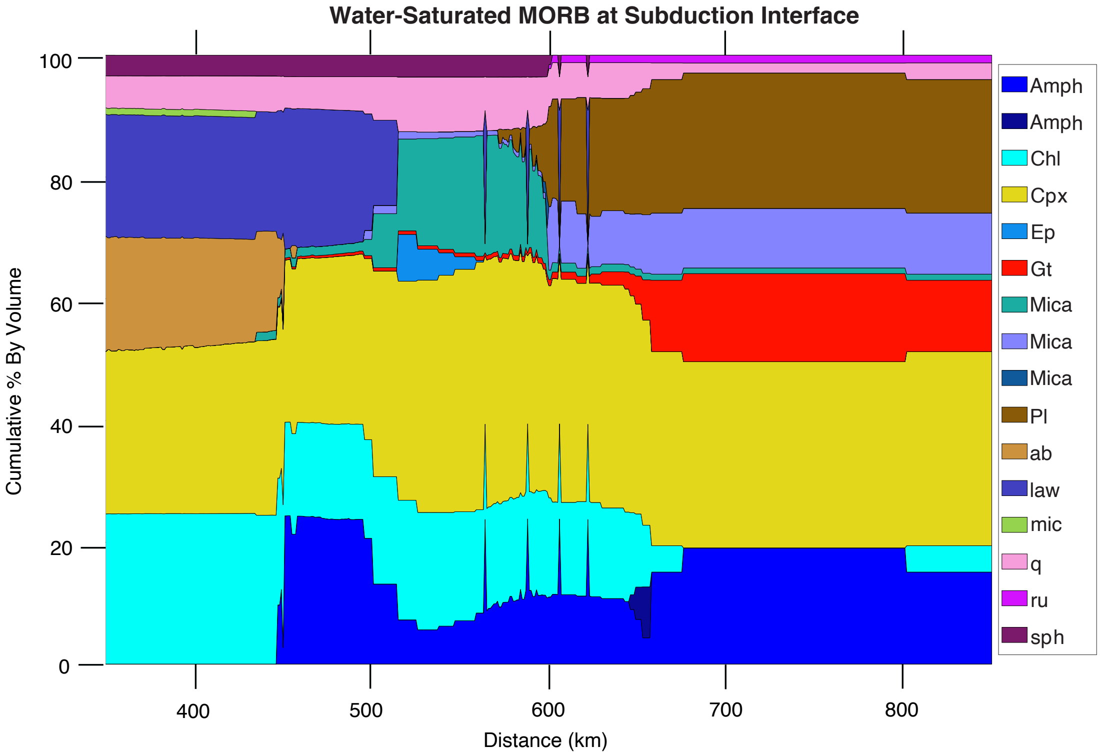

Figure A9. Stable mineral assemblages calculated using *Perple_X* for the depleted MORB composition with water-saturated conditions. The top diagram shows mineral phases plotted as cumulative % by volume vs. distance along the transect (A-A' in Figure 2.1). These results are taken along the fault interface (0 km below the fault). Abbreviations represent the following minerals: q = quartz, ru = rutile, Gt = garnet (almandine), Cpx = clinopyroxene (augite transitioning to omphacite along transect), sph = sphene, Amph = amphibole (glaucophane), Chl = chlorite, law = lawsonite, ta = talc, Mica = muscovite, ab = albite. The lower panel shows the pressure (blue line) and temperature (red line) conditions used to generate the results in the top diagram. PT conditions were taken at the subduction interface and were determined using the 20 m.y. *Thermodsubduct* model results.

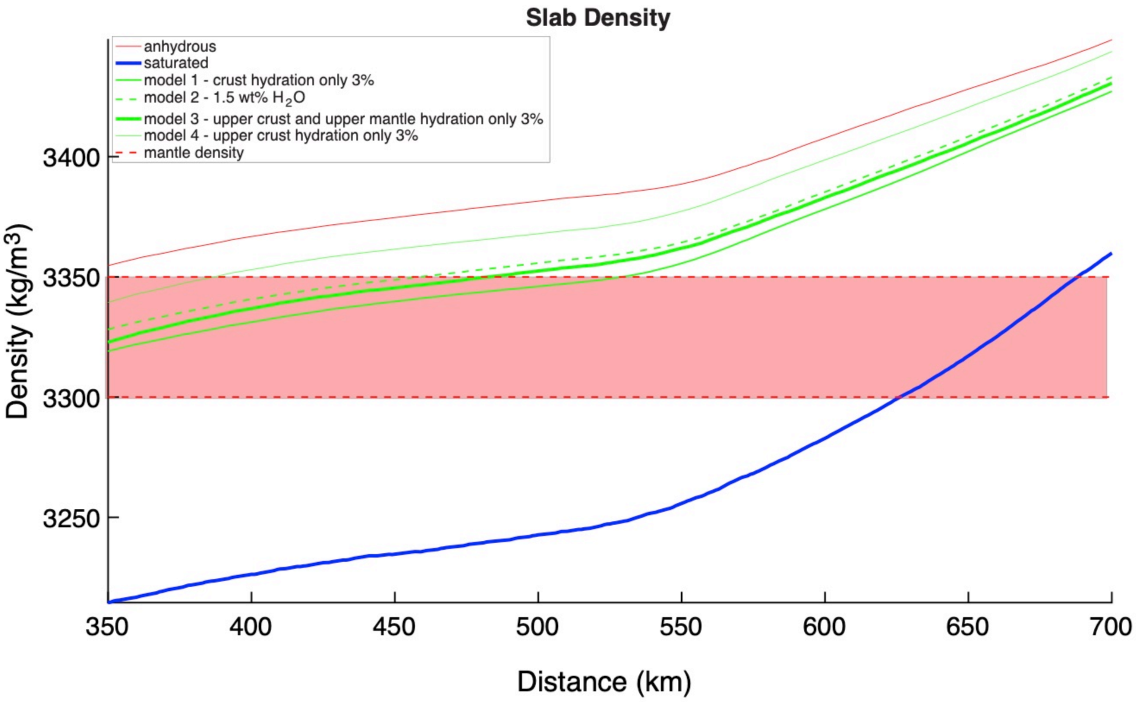

Figure A10. Calculated slab densities versus distance along A-A' (Figure 2.1) for varying degrees of hydration of crust and upper mantle. Crust is assumed to be the Yakutat basalt composition. Calculations assumed conditions determined for 20 m.y. of subduction using the finite difference (*Thermodsubduct*) model, and the Yakutat basalt composition for the upper crust. Anhydrous model is plotted in mauve, and water-saturated model is plotted in blue. Green lines correspond to hybrid models with varying levels of water saturation in different slab layers and are as follows: Model 1: 3 wt% H_2O in the upper (5 km) and lower crust (15 km), no hydration in the lithospheric mantle. Model 2: 1.5 wt% H_2O in the entire crust (20 km) and upper 10 km of the subducting mantle. This model is the same as the hybrid model shown in green in Figure 2.8. Model 3: 3 wt% H_2O in the upper 5 km of the crust, and 3 wt% H_2O in the top 5 km of the subducting mantle. No hydration in the lower 15 km of the crust. Model 4: 3 wt% H_2O in the upper 5 km of the crust only, with no hydration in the lower crust or mantle. A range for upper asthenospheric density is shaded in red.

Data Set S1. This data repository contains codes and data related to Chapter 2. It can be viewed at https://zenodo.org/record/4670347#.YG3UmxNKgQ8 (doi:10.5281/zenodo.4670347). The main folder contains a matlab code titled "Calc_Density_Hydration.m". This code uses our thermal modeling results and *Perple_X* results to calculate slab density, density across our A-A' transect (Figure 2.1), and wt% H_2O across transect and contained within the slab. A further description is contained within the Matlab code itself. The "Calc_Density_Hydration.m" code uses files in three folders in order to run properly. It uses the files in the "Data" folder, which contains the results for Alaskan flat-slab subduction thermal conditions from two different thermal modeling codes. Results using *PGCTherm2D* are in the file titled "pgc_shear03_03252020.dat". Results using *Thermodsubduct* are in the file titled "thermod_shear03_03252020.txt". The final file in the "Data" folder is "geometry3.txt", which defines the geometry of the subduction zone for the Calc_Density_Hydration.m code. The matlab functions contained within the "Functions" folder allow the matlab code to read *Perple_X* .tab files, as well as various other codes that enable the Calc_Density_Hydration.m code to work. Within the *Perple_X*_Files folder are all the .tab files required for the Calc_Density_Hydration.m code to function properly, as well as other *Perple_X* related data from our research. Within the main folder are results run in *Perple_X* using werami for each of the compositions used in our study. They include.tab files created within *Perple_X* werami for density on a 100 by 100 2D grid and H_2O (wt%) on a 100 by 100 2D grid. Within the anhydrous_assemblages_figures folder, we present the anhydrous results as .eps files for both of the basalt compositions used in our study, the gabbro used in our study, and the peridotite composition used in our study. The MORB composition anhydrous results are presented in the figure basalt_0_h2o_allmorb_modes_hp11ver_1109_2.eps, the Yakutat basalt composition anhydrous results are presented in the figure basalt_0_h2o_yak_modes_hp11ver_1109_2.eps, the gabbro composition anhydrous results are presented in the figure gabbro_0_h2o_modes_hp11ver_1111.eps, and the MOR peridotite composition anhydrous results are presented in the figure perid_DMM_0h2o_hp11ver_1028_thermod.eps. All results are plotted along the 0-850 km transect A-A' (from Figure 2.1 of Chapter 2), and are plotted using results from *Thermodsubduct*. The PT conditions used to plot these figures and the figures in Chapter 2 are in the Data folder. Figures 2.4-2.5 in the Chapter 2 were generated using the file TPYX_uppercrust_5km.txt, which contains the temperatures in Kelvin in column 1, pressure in bars in column 2, depth in kilometers in column 3, and distance along A-A' (Figure 2.1) in km in column 4. This file was generated using temperatures from *Thermodsubduct* results at 20 m.y. and was taken at 5 km below the fault (see Figure 2.3 for reference). Figure 2.6 used the file TPYX_lowercrust_15km.txt, and shows temperatures and pressures at 15 km below the fault. Data in this file and all similar files are the same as the file used for Figures 2.4 and 2.5. Figure 2.7 in Chapter 2 was generated using the file TPYX_mantle_5km.txt that contains temperatures and pressures associated with a transect 5 km below the crust-mantle boundary, or 25 km below the fault. The file TPYX_uppercrust_0km.txt shows conditions at the fault, and was used to create Figure A9. Temperatures and pressures in these files have a smoothing parameter applied to them in order to improve figure readability. Within the Perple_X_dat_files folder are the .dat *Perple_X* files used to create all our results, and include the saturated and anhydrous .dat files for each composition. We also include our perplex_option.dat file, our solution_model.dat file, and the hp11ver.dat file that was modified using ctransf (ctransf_hp11ver.dat). From the main directory, the pgctherm2d_files folder contains the input_data and inst_cb inst_ob files used to run the finite element thermal modeling in Alaska. This folder includes separate folders for both the no shear heating included model and shear heating included (frictional coefficient of 0.03). The input_data files define the geometry and parameters for the finite element thermal model, and the inst_cb and inst_ob files define the continental and oceanic side geotherms respectively. The .dat files in each folder contain the results. From the main directory, the thermod_files folder contains the .sf files used within the *Thermodsubduct* software for our finite difference Alaska thermal modeling. The file titled "ak_shear03_2km.sf" contains the run parameters for our 2-km spaced model of Alaska and includes frictional heating. It has been run out to 100 my. The file "ak_noshear_2km.sf" contains the run parameters for our 2-km spaced model of Alaska with no frictional heating included. Either of these files may be uploaded into the *Thermodsubduct* software to view run parameters.